Development of smart glazing techniques for efficient buildings

Mohammed Abdulsattar Jabbar Lami

A thesis submitted in partial fulfilment of the requirements of Sheffield Hallam University for the degree of Doctor of Philosophy

October 2023

Declaration

I hereby declare that:

1. I have not been enrolled for another award of the University, or other academic or professional organisation, whilst undertaking my research degree.
2. None of the material contained in the thesis has been used in any other submission for an academic award.
3. I am aware of and understand the University's policy on plagiarism and certify that this thesis is my own work. The use of all published or other sources of material consulted have been properly and fully acknowledged.
4. The work undertaken towards the thesis has been conducted in accordance with the SHU Principles of Integrity in Research and the SHU Research Ethics Policy.
5. The word count of the thesis is 49642.

Name	Mohammed Abdulsattar Jabbar Lami
Award	Ph.D
Date of Submission	5/10/2023
Faculty	Faculty of Science, Technology & Arts
Director(s) of Studies	Faris Al-naemi

Abstract

In recent times, the buildings sector has emerged as a major consumer of energy in urban areas. Among various contributors, windows in the external envelope of buildings are particularly responsible for a significant portion of energy consumption due to their high thermal conductivity. The integration of smart films with traditional glazing has been explored as a means to modify the opt properties of windows. However, this integration can affect the visual connection between occupants and the outside views. This thesis focuses on advancing smart windows to enhance their thermal and daylight performance, with two main developments proposed.

The first development involves the use of double-glazed ventilated windows in cold climate regions. These windows utilise waste air from the building for ventilation. However, existing research indicates that under certain conditions, the waste air may be insufficient to maintain proper ventilation. To address this, the thesis proposes validated procedures that optimise the utilisation of waste air, enabling sustained ventilation for longer periods. This optimisation contributes to improved thermal efficiency of ventilated windows and energy savings in buildings. Experimental results obtained from a small-scale test room demonstrate that implementing the proposed optimisation process can achieve energy savings of up to 83% compared to conventional double-glazed windows.

The second development focuses on integrating a double-glazed window with a polymer dispersed liquid crystal (PDLC) film for hot climate regions. Previous research overlooked the impact of reduced optical transmission on the window's visual clarity. This thesis introduces an image-processing quantification algorithm for evaluating the visual experience through PDLC windows. The algorithm identifies the comfortable visible range and determines the lowest acceptable transparency level to maintain satisfactory visual communication with the outdoor environment. Experimental results from a small-scale test room indicate that implementing the proposed quantification process enables the provision of a customized range of visual quality based on user preferences. The system also ensures that the operating visibility does not fall below a pre-defined threshold level. The trial illustrates that altering the PVR ratio from 0 to 1 has the potential to alter the mean contrast value in a clear sky setting, shifting it from 0.18 to 0.37. Additionally, in order to ensure a minimum acceptable vision quality, the proposed algorithm ensures that the optical transmittance of the window remains above a specified threshold value (C_{th}). Moreover, the experiment indicates that an increase in the PVR ratio of the PDLC window from 0 to 1 leads to a rise in the solar heat gain coefficient (SHGC) from 0.42 to 0.623. Furthermore, elevating the PVR ratio of the PDLC window from 0 to 1 allows more light to enter the interior environment of the test room, showing an increase of 73% to 85% compared to traditional double-glazed windows.

Furthermore, the thesis proposes four different methods for implementing the vision quantification process, including MATLAB, system on-chip (SoC) systems, Cortex-A9 microcontrollers, and field-programmable gate array (FPGA) chips. Each method employs unique hardware and software configurations. Overall, the implementation methods exhibit a diverse range of image-processing capabilities. The systems are evaluated based on standard parameters for automated systems, including latency, throughput, number of clock cycles, power consumption, and cost. Experimental results demonstrate that the FPGA system delivers the most effective performance, with a latency of 9.14 seconds.

The contrast estimation latency for the ARM Cortex-A9 microcontroller was 8.36 seconds, while for MATLAB realizations, it was 2.98 seconds. This indicates a comparable performance between both systems. However, there is a noticeable uptick in power dissipation and clock cycle consumption. The most efficient system, featuring a latency of only 0.228 seconds and minimal power dissipation, employs an ARM Cyclone-V FPGA chip. This FPGA system successfully achieved the proposed quantification process with a minimal repetition time of T_r = 9.14 seconds.

Acknowledgement

I would like to express my deepest gratitude to my supervisors, Dr. Faris Al-naemi and Dr. Walid Issa, for their invaluable guidance, unwavering support, and expertise throughout the entire duration of this thesis. Their mentorship, insightful feedback, and encouragement have been instrumental in shaping this research and enhancing its quality. I am truly grateful for their dedication and commitment to my academic growth.

I would also like to extend my heartfelt appreciation to my colleague Dr. Hussein A. Jabbar, whose insightful discussions and valuable input greatly contributed to the development of ideas and the overall improvement of this work. Their collaboration and shared enthusiasm have been instrumental in pushing the boundaries of this research.

To my parents, I owe an immeasurable debt of gratitude for their endless love, encouragement, and unwavering belief in my abilities. Their constant support and sacrifices have been the foundation upon which I have built my academic journey, and for that, I am forever grateful.

I am also deeply thankful to my loving wife and daughters, whose unwavering support, patience, and understanding have been my constant source of motivation. Their belief in me and their unwavering encouragement have sustained me during the challenging times of this thesis. Their love and presence have been my strength, and I am truly blessed to have them by my side.

Lastly, I would like to express my sincere appreciation to all the individuals, friends, and colleagues who have provided their assistance, advice, and encouragement throughout this research endeavour. Your contributions, whether big or small, have made a meaningful impact on this work, and I am grateful for your support.

To all those mentioned above and to anyone else who has played a part in my academic journey, thank you from the bottom of my heart. Your support and belief in me have been instrumental in the completion of this thesis.

Table of Contents

List of Tables

List of Figures

List of Equations

List of acronyms and their meanings

DNI	direct normal irradiance in (W/m^2)
DHI	diffused horizontal irradiance in (W/m^2)
E_{XT}	extra-terrestrial illuminance (lux)
E_{DN}	direct normal illuminance (lux)
E_{DH}	direct horizontal illuminance (lux)
E_{KH}	diffuse horizontal illuminance (lux)
E	total illuminance falling on the horizontal plane (lux)
GHI	global horizontal irradiance in (W/m^2)
G_{SC}	solar illuminance constant (lux)
PVR	preferred vision ratio (0 ~ 1)
CLB	configurable logic block
DSP	digital signal processing
$FPGA$	field programmable gate array
HD	high definition image
IP	intellectual property
MC	microcontroller
$PDLC$	polymer dispersed liquid crystal
PWM	pulse width modulation
SoC	system on-chip
$VHDL$	very high-scale integrated circuit hardware description language
ACC	accumulator circuit
DIV	division circuit

MUL multiplier circuit

SUB subtractor circuit

$SQRT$ square-root circuit

List of symbols and their meanings

$Q_{Tungsten}$ heat generated by the tungsten wire (W)

Q_{pot1} heat stored in the pottery (W).

Q_g heat transfer through the glazing (W).

Q_{room1} heat stored inside the test room (W).

M_{room1} mass of the air inside the room.

V_{room1} volume of the test room.

C_{air} heat capacity of the air = 1.006 kJ/kg°C.

T_{in} temperature inside the room in °C.

Q_{w1} heat transfer through inside and outside air convection and conduction through the insulation board wall (W).

U_{w1} combined U-value of the test enclosure's wall with inside and ambient air in (W/m^2K).

h_o outside convection heat transfer coefficients in (W/m^2K).

h_i inside convection heat transfer coefficients in (W/m^2K).

L thickness of the insulation board (m).

K thermal conductivity of the insulation board in $W/m\ K$.

A_w area of the insulation board in m^2.

T_o temperature of the atmosphere in °C.

U_g heat transfer coefficient (U-value) of the glazing (W/m^2K).

ρ_{air} density of the air = 1.2250 kg/m^3.

Q_{pot2} heat dissipation in the pottery inside the Heat source model (W).

M_{pot} mass of the pottery = 0.53 kg.

C_{pot} heat capacity of the pottery = 0.85 (kJ/kg°C).

T_{pot} temperature of the pottery (°C).

Q_{room2} heat stored inside the heat source model (W).

Q_{w2} heat transfer through inside and outside air convection and conduction through the insulation board wall of heat source model.

R electrical resistivity of the tungsten wire at the steady-state temperature.

R_o electrical resistivity of the tungsten wire at the initial temperature, for the executed experiments 25 °C and R_o = 168 Ω.

T_o initial temperature of the tungsten wire in Kelvin, for the executed experiments 25 °C or 298 K.

T_s steady-state temperature of the tungsten wire in Kelvin, T_s has been measured experimentally by a K-type thermometer, it was 306 °C or 579 K.

v root-mean-square value of the applied ac voltage = 225 volt.

C_{th} threshold contrast

C_{min} minimum contrast

C_{max} maximum contrast

C_{PVR} preferred contrast value

I_{ij} value of the pixel in the i^{th} column and the j^{th} row

$\bar{I}$ average brightness of the image I

m air mass (kg)

M numbers of column in an image

n the day of the year

N numbers of row in an image

T_r	repetition time of the automated vision quantification process (sec)
v_{th}	threshold voltage (volt)
v_{PVR}	voltage at preferred contrast (volt)
θ	Zenith angle (degree)
$\propto_S$	altitude angle (degree)

Chapter 1: Introduction

1.1 Background to the study

A number of research studies have highlighted the growing significance of the buildings sector worldwide, leading to a substantial increase in energy consumption. As per the United Nations Environment Programme's status report, the buildings sector accounts for 30% of global energy consumption and was responsible for 28% of carbon emissions in 2018 [1]. Furthermore, the trend of increasing energy consumption in the buildings sector continues to persist, as the global status report in 2022 revealed a 4% increase in energy demand for buildings during 2021 as compared to 2020 [2]. In the United States, the US Energy Information Administration has reported that commercial buildings consume 35% of electrical generation [3]. Recent studies have also indicated that the buildings sector contributes to 40% of carbon emissions across the world [4], [5].

Extensive research has been conducted on the energy systems of buildings to counteract the adverse effects of CO2 emissions. The Net-Zero Energy Buildings (NZEB) system is a promising approach that allows buildings to generate electricity independently without relying on external energy supplies. The European Economic Community (EEC) was the first organization to set targets for the adoption of NZEB in European Union countries, with the aim of promoting the use of various renewable energy sources in buildings. The implementation of NZEB system is expected to enhance the energy efficiency of buildings and reduce reliance on fossil fuels [6].

The thermal performance of buildings can be negatively affected by heat loss through the building envelope, which includes external walls and windows. Windows, in particular, have a higher rate of heat transfer due to their high U-value for glazing, making them the primary source of energy loss in buildings [16]. To address this issue and reduce energy consumption and carbon emissions associated with heating and cooling, recent research has focused on developing methods to improve the thermal conductivity of glazing. The primary goal of these efforts is to optimize the thermal performance of windows in order to minimize energy loss. Numerous techniques have been proposed and studied for their effectiveness in improving the thermal conductivity of glazing.

When selecting an optimal technique for improving the thermal performance of windows, it is important to consider the climate conditions of the building's location. In regions with cold

climates, the use of ventilated windows has been found to be an effective method for enhancing the thermal performance of glass. Several studies have utilised ventilated windows to increase the temperature of the glazing surface, thereby reducing the temperature difference between the indoor environment and the glazing surface. As a result, the flow of heat from inside to outside through the glass is reduced. In cold regions, the technique involves injecting warm air from the internal environment of buildings into the panes of ventilated windows. The warm air circulates within the window before being exhausted into the outside environment. This approach helps to minimize heat loss through the window, reducing the heating load of buildings and lowering energy consumption [79]–[83].

To maintain a comfortable indoor environment, it is important to periodically replace the indoor air with fresh outdoor air. This can be achieved by compensating for the exhausted indoor air with outside air and using a heating source to warm up the compensated air to maintain the desired temperature. However, this process requires additional energy to operate the heating system during window ventilation operation and cannot be expected to save energy. Despite this, buildings are typically designed to change their internal air periodically to maintain a healthy environment for occupants. Air change is achieved through forced ventilation, which utilises specialized mechanical fans to measure the number of air changes per hour. For example, if a building has a 1.2 air change per hour, the indoor air will be changed 1.2 times within one hour [96]. Each time the air is changed, the exhausted air is released outside and fresh air is introduced into the building. Another way to ventilate a room is by using warm air to ventilate windows. This method involves warming up the glazing panes with warm air before exhausting it to the outside environment. Although this process consumes energy to warm up the compensated air, it balances the need for refreshing the indoor environment, thereby enhancing the efficiency of energy consumption. In summary, maintaining a comfortable indoor environment requires periodic replacement of indoor air with fresh outside air. While using a heating system during window ventilation operation can increase energy consumption, forced ventilation is necessary to maintain a healthy indoor environment. Additionally, using warm air to ventilate windows provides a trade-off between the need for ventilation and energy consumption, thereby enhancing energy efficiency.

Recently, there have been various designs of ventilated windows introduced to optimize thermal insulation and reduce energy consumption. However, these windows may face

certain challenges. The efficiency of the window's thermal insulation is largely dependent on the quality of the available warm air. The warmer the air, the closer the temperature of the glazing will be to that of the room, resulting in better insulation. When the temperatures of the room and the glazing are the same, the window is fully insulated, and no heat is lost through it. Additionally, if the temperature of the glazing is higher than that of the room, the window will act as a source of heat. However, the temperature of the warm air depends on the source of the exhausted air from the building. For example, wasted air from kitchens tends to be hotter than other sources [90].

The thermal efficiency of glazing can be increased by increasing the airflow around it, which enhances the thermal convection between the glazing and the air, thereby lowering its thermal conductivity [90]. However, this higher airflow is dependent on the availability of wasted air in the building. Buildings that have a high rate of air change per hour have a greater amount of wasted air flow. The size of a window is an essential factor in determining its thermal efficiency since larger windows lead to greater heat transfer towards the external environment. For instance, buildings with a high window to wall (WWR) ratio have a larger area of glazing. Nonetheless, increasing the size of a window requires more warm air from the building to maintain a consistent temperature for the glazing. To determine the size of a ventilated window, the window to wall ratio, the number of panes, and the width of the gap between the panes must be considered. An additional challenge associated with the operation of ventilated windows is the impurity of wasted air. For instance, warm, fumy air from kitchens can cause a foggy appearance through the window. Therefore, ventilation systems should be fitted with specialized filters to purify the air, which makes the system more complex and expensive to operate.

In regions with warm climates, air conditioning systems are essential for cooling buildings. Various techniques are employed to improve the thermal efficiency of windows. In addition to high temperatures, buildings are also affected by the greenhouse effect, which causes the temperature inside to rise significantly. Traditional glazing has a high level of transparency, which allows a significant amount of daylight to enter the building. In facade buildings, which have a larger window to wall ratio, more heat is stored inside due to the increased amount of daylight. This requires additional energy consumption from air conditioning systems to maintain a comfortable indoor temperature.

Window shading is a highly effective technique that can help reduce the energy required to cool a building. It involves limiting the amount of daylight that enters indoor environments by decreasing the transparency of the glazing. There are many different methods that can be used to shade windows, including using curtains to partially block sunlight and reduce the greenhouse effect, as well as affixing slabs or small boards externally at the angle of sunlight to block it. These slabs can be adjusted throughout the day using special controllers that track the sun's position. While these shading methods can play a significant role in decreasing cooling loads, they do have a potential downside. The use of opaque objects to shade the window may result in a poor visual connection with external views for occupants. This is because, from the occupants' perspective, the primary function of windows is to enable them to interact with the outdoor environment [48]. Therefore, any shading technique used should not hinder this essential function. It is essential to strike a balance between effective window shading and the need for adequate natural light and unobstructed views for building occupants. This can be achieved through the use of innovative shading technologies that allow for the control of the amount of sunlight that enters the building while still providing access to views of the outside world. Such technologies include dynamic shading systems that adjust the level of shading based on the amount of sunlight entering the room, as well as electrochromic glass that can be tinted on demand to provide shading when needed. In conclusion, while window shading is an effective energy-saving technique, it is crucial to consider the needs of building occupants and ensure that any shading method used does not interfere with their ability to interact with the outdoor environment. The use of advanced shading technologies can help achieve this balance, allowing for efficient energy use while still providing adequate natural light and unobstructed views.

Another method for window shading is the permanent attachment of a thin film with a specific level of transparency to the glazing [9]. This modification results in minimal improvement to the thermal resistance of the glazing, and the heat transfer coefficient or U-value remains nearly the same. However, the primary advantage of this modification is that it improves the solar heat gain coefficient, leading to reduced solar radiation reaching the building's interior. This film's low transparency restricts visibility through the glazing to a certain extent, and therefore, the transparency level of the film should not compromise the occupants' visual comfort through the window. In addition, it is essential to maintain an

adequate level of daylight in the internal environment, or there should be a balance between daylight and artificial light. This consideration ensures that the addition of the film does not reduce the overall amount of light in the space, as this could negatively impact the occupants' comfort and productivity. Therefore, it is crucial to carefully consider the level of transparency of the added film to ensure that it provides an appropriate level of shading while maintaining adequate visibility and light levels. Overall, the permanent attachment of a thin film to the glazing is an effective window shading method that reduces solar heat gain. However, it is crucial to balance the level of shading with the need for adequate visibility and light levels in the building's interior. This can be achieved by selecting a film with an appropriate level of transparency to ensure occupant comfort and maintain productivity levels.

A recent innovation in window shading techniques is the use of Semi-Transparent Photo Voltaic (STPV) panels. These panels are made of glazing materials and serve as a substitute for traditional glazing. STPV panels are equipped with solar cells that generate electricity by absorbing solar radiation, just like conventional photovoltaic (PV) panels. However, the difference is that STPV panels are semi-transparent and only absorb a portion of the incident radiation, allowing some light to pass through. While STPV panels are effective at generating electrical energy, their efficiency is lower than that of regular PV panels due to their semi-transparent nature [7], [8]. One of the main advantages of STPV panels is their ability to allow daylight into buildings while simultaneously generating electricity. However, the reduced transparency of the glazing can negatively impact vision through the window, making it necessary to use more artificial lights to compensate. Therefore, while STPV panels are an innovative way to generate electricity and provide shading to buildings, careful consideration must be given to their impact on occupants' vision and lighting needs. Balancing the amount of electricity generated with the amount of daylight allowed in and the occupants' need for adequate lighting is essential to ensure occupant comfort and productivity.

A recent advancement in window shading techniques is the development of electrochromic thin films, such as Polymer Dispersed Liquid Crystal (PDLC) films. These films can be applied to traditional glazing and provide varying degrees of transparency, ranging from opaque to transparent states, depending on the input excitation. The ability to control the transparency of PDLC films offers significant advantages to windows. Applying PDLC films to traditional windows enables the management of the amount of daylight passing through them, allowing

for a balance between natural and artificial lighting. Additionally, the controlled visibility provided by PDLC films allows for control over the quality of the external views seen by occupants through the glazing [9], [10]. This is an important factor to consider, as occupants typically value the ability to interact with the outdoor environment through windows. Therefore, the use of electrochromic thin films, such as PDLC films, can be an effective way to shade the glazing of windows while still providing occupants with the benefits of natural light and external views. Proper management of the transparency of these films can help balance lighting needs and maintain occupant comfort and productivity.

To utilise PDLC films for shading windows, an alternating current excitation is required. When no voltage is applied, the film is opaque, and as the AC input increases, the transparency level of the PDLC film increases up to a maximum of 90%. Therefore, it is important to understand the relationship between the applied voltage and the transparency level of the PDLC film to allow an automated system to adjust the transparency level based on different conditions. The use of PDLC films on windows will result in a lower solar heat gain coefficient, as the solar radiation entering the building will be restricted. However, it is important to note that unlike other window shading techniques, the solar heat gain coefficient of PDLC films is variable and depends on the level of excitation applied to the film. Overall, the ability to control the level of transparency through an automated system makes PDLC films a promising solution for managing daylight and artificial light loads while also providing visual access to the outdoor environment.

Smart windows using the aforementioned technologies for window shading and ventilation can transform traditional windows into intelligent components in building envelopes. To operate, smart windows require an electrical connection for excitation, such as in the case of PDLC windows, or to receive generated electricity, such as STPV windows. Furthermore, smart windows require control systems to manage their operation. For instance, ventilated windows need management for airflow through the window panes and to control valves and air pumps. In PDLC glazing, a controller plays a crucial role in determining a preferred transparency level. By relying on the transparency-voltage relationship, the controller can expect the correct excitation. Overall, smart windows with these new technologies become adaptive devices with automated and artificial intelligence systems. A proper control system must be implemented based on the requirements of smart window systems. The

implementation process should involve two steps. Firstly, the function required to manage a window should be interpreted into an algorithm. Secondly, a suitable implementation method should be chosen to realize the control function.

To enable the control of smart windows, various options are available for implementing control circuits. One such option is to use PC-based software, such as MATLAB, to implement a control process. Once the target process is converted to a program, the software executes it to achieve the control function. However, the efficiency of the utilised PC impacts the performance of the control process, and establishing a physical interface between a PC and the smart window system could be a challenge. Another option for controlling smart windows is to use microcontrollers. Microcontrollers are capable of managing digital and analogue actuators and sensors efficiently, making them a viable option for controlling smart windows. The control function for a smart window is written in a programming language such as C or Python, and the microcontroller executes the program. The overall performance of the system depends on the efficiency of the microcontroller and the programming language used. Compared to PC-based software, microcontroller circuits offer an advantage in terms of easy interconnectivity with smart window systems.

A System on Chip (SoC) can be employed to achieve a control function for smart windows [132]. SoC systems have an embedded processing unit and its corresponding peripheral circuits on a single chip. It can perform a variety of functions with less size and power consumption compared to microcontroller implementations. The advantage of SoC implementation is the capability of building different digital and analogue modules on one chip that can serve the targeted function. On the other hand, the Field Programmable Gate Array (FPGA) implementation method configures the available logic blocks on a single chip to build complex digital circuits [131]. The preferred control function of a smart window system can be prototyped using the digital entities on a FPGA chip. The advantage of FPGA implementation is that it provides a low latency design and high throughput. However, FPGA implementation is limited to digital systems only. The area on the FPGA chip may not be enough to prototype the design for massive functions; in such cases, multiple FPGA chips can be used to cover the required process.

To sum up, there are different methods available for implementing smart window controllers, and their performance can be affected by various factors. To determine the most suitable

approach, it is important to consider factors such as processing speed, throughput, latency, cost, and power consumption. Processing speed refers to the ability of a processing unit to handle one bit of data per second and is typically measured in clock speed or frequency in hertz. Throughput measures the productivity of a processing unit, such as the amount of data or tasks processed over a specific time interval and is measured in data capacity per second (bit or byte). Increasing the processing speed can lead to higher throughput and efficiency for a processing unit. Latency indicates the time required by a processing unit to process an instruction in terms of the number of clock cycles. The lower the latency, the higher the processing efficiency. Power consumption is another critical factor that can increase with the frequency of the operating clock and the complexity of the running function. Therefore, it is essential to consider all of these factors to select the best approach for implementing smart window controllers.

1.2 Aims and objectives

The aim of this study is to further utilise smart windows in different climate zones for optimum thermal and daylight performance and develop an automated system to control the operation of smart windows.

The objectives are:

1- Develop a standard procedures to optimise the usage of waste air from buildings in ventilation process of double-glazed windows.
2- Determining of the maximum number of windows that can be ventilated by a given waste air velocity to achieve highest energy savings.
3- Developing a mathematical representation of the vision quality through polymer dispersed liquid crystal double-glazed windows.
4- Develop a quantification algorithm for the vision through polymer dispersed liquid crystal double-glazed windows.
5- Developing a parameter in the system of polymer dispersed liquid crystal double-glazed windows that describes user's preferred vision level.
6- Find the minimum allowed visible transparency that maintains a comfortable vision through the polymer dispersed liquid crystal double-glazed windows.
7- Implementing an automated quantification system for vision through polymer-dispersed liquid crystal double-glazed windows.

1.3 Contributions

The contributions are:

1- A standard flowchart has been developed to optimise the usage of waste air from buildings in ventilation process of double-glazed windows.
2- A quantification method has been developed to quantify the vision through PDLC double-glazed windows.
3- An automated quantification system for vision through PDLC double-glazed windows has been developed.

1.4 Publications

The journal papers arising from this thesis are the following:

1- Lami, M., Al-naemi, F., Jabbar, H.A. et al. Optimisation of wasted air utilisation in thermal loss reduction in double-glazed windows of commercial buildings in cold regions. Int J Energy Environ Eng 14, 145–165 (2023). https://doi.org/10.1007/s40095-022-00499-0

2- Lami, M.; Al-naemi, F.; Alrashidi, H.; Issa, W. Quantifying of Vision through Polymer Dispersed Liquid Crystal Double-Glazed Window. *Energies* 2022, *15*, 3196. https://doi.org/10.3390/en15093196

3- Lami, M., Al-naemi, F., Issa, W.: Automated quantification system for vision through polymer-dispersed liquid crystal double-glazed windows: Circuit implementation. IET Circuits Devices Syst. 1–15 (2022). https://doi.org/10.1049/ cds2.12135

The conference papers arising from this thesis are the following:

1- LAMI, Mohammed, AL-NAEMI, Faris, JABBAR, Hussein, ALRASHIDI, Hameed and ISSA, Walid (2021). Thermal Loss Reduction Using a Ventilated Double-Glazed Window for Commercial Buildings in Average-Climate Environments. In: *2021 International Conference on Sustainable Energy Engineering and Application (ICSEEA).* IEEE.

1.5 Outline of the thesis

The outline of the thesis is presented below, it is worth mentioning that critical analysis and summary have been included at the end of each chapter:

Chapter two: Literature Review.

In this chapter, previous related studies in relation to utilisation of smart windows and control techniques of smart windows are reviewed.

Chapter three: Optimising the use of building's waste air in double-glazed ventilated windows for commercial buildings in cold regions.

This chapter presents the first research problem, proposes a design for ventilated double-glazed windows in cold regions. The chapter demonstrates the methodology of this piece of research, shows the experimental results, discusses them, and answers the research question.

Chapter four: Quantification of visual comfort through polymer dispersed liquid crystal double-glazed windows.

This chapter presents the second research problem related to the utilisation of PDLC double-glazed windows. It proposes a system to measure the quality of vision through PDLC double-glazed windows in hot regions. The chapter demonstrates the methodology of this part of research, shows the experimental results, discusses them, and answers the research question.

Chapter five: Prototyping of automated quantification controller for vision through PDLC double-glazed windows.

This chapter presents the third research problem about the implementation of a controller for PDLC double-glazed windows. A proposed automated system shows a quantification process for the vision through a PDLC double-glazed window in terms of vision contrast. The chapter demonstrates the methodology of this part of research, shows the experimental results, discusses them, and answers the research question.

Chapter six: Conclusion and Further Work.

In this chapter, the study is summarised, and further research work is presented.

1.6 Summary

In this chapter, the main concepts of smart windows in modern buildings are introduced. Smart windows are designed to provide comfortable environments for the occupants. Different techniques are used by smart windows to optimise their performance. Climate conditions are an essential factor in determining the appropriate technique for a particular region. Ventilated windows are applied to buildings in cold environments to mitigate heat loss through windows. The wasted air is used to warm up the panes of the window to reduce the temperature difference between the glazing and the room. Consequently, energy savings can be achieved in heating loads due to the enhancement in the thermal isolation of the window. In contrast, PDLC double-glazed windows are employed in hot environments. They help reduce the greenhouse effect inside buildings. Due to their capability of adjusting the transparency of glazing, it is possible to limit the quantity of daylight accessed in internal environments. The mean value of room temperature and the annual consumption of cooling loads can be minimized. Smart windows are active elements in the envelop of buildings and achieve different functions; hence, controllers should be implemented to manage their operations. Implementation of controllers can be fulfilled by employing the available techniques of circuit implementation. The implemented systems should be automated so they can drive the smart windows autonomously based on real-time conditions. Operating conditions are the factors that may determine the status of a window, such as indoor and outdoor conditions and light intensity. As a hardware implementation method, microcontrollers are the basic option that can serve smart windows. Systems on chip are suitable for some applications of smart window controllers. Moreover, field programmable gate array technique shows an efficient performance when working as controllers. In software implementation, PC-based software, like MATLAB, is available to act as a smart window controller. Depending on the requirements of the smart window system, a proper implementation type can be chosen. The performance of a microcontroller can be evaluated by its processing speed, throughput, power consumption, and cost.

Figure 1. 1 provides an overview of the workflow outlined in the thesis. The primary focus of this research is centred around the development of two distinct types of intelligent windows. In the context of cold climates, the thesis explores the implementation of a ventilated double-

glazed window. The main objective here is to optimize the utilisation of waste air from buildings, particularly in relation to the ventilation process.

In contrast, for hot climates, the thesis examines the use of a polymer dispersed liquid crystal (PDLC) double-glazed window. In this scenario, the aim is to quantify the visual qualities of the proposed window when looking towards external views. To achieve this, the quantification process involves tasks such as image processing and mathematical computations. Consequently, an automated system will be devised and implemented to efficiently handle the aforementioned tasks in this particular scenario.

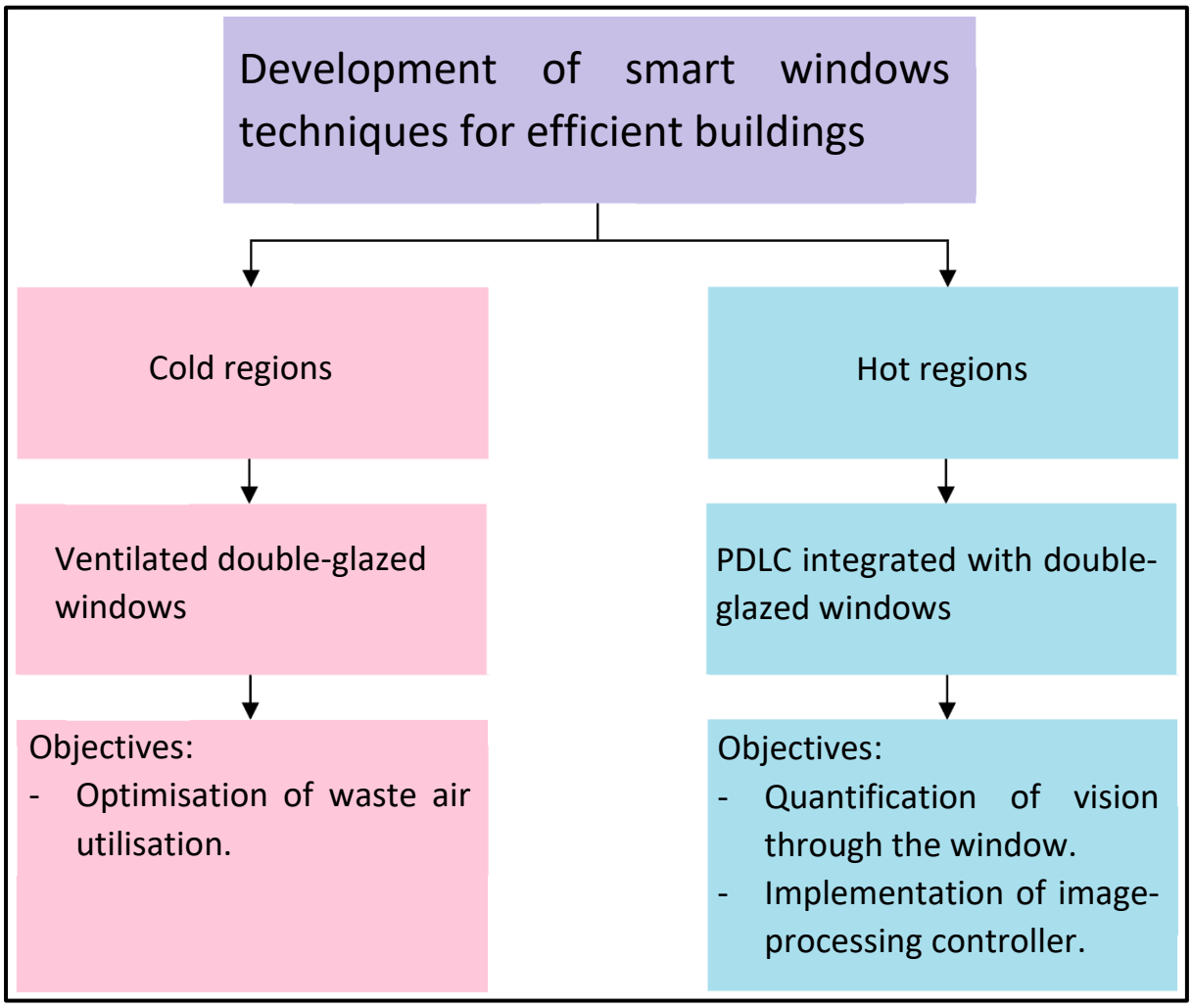

Figure 1. 1. Workflow.

Chapter 2: Literature review

2.1 Energy consumption and heat loss in the glazing in commercial buildings

Various studies have recently concentrated on energy conservation in buildings due to the rising energy consumption in this sector. In contemporary cities, the energy consumption of buildings has surpassed that of transportation and industry. In China, buildings account for 28.6% of the overall energy consumption [11]. Moreover, the International Energy Agency (IEA) has reported that residential buildings consume 20% of the total energy consumption in Japan, China, Russia, India, and the United States [12]. In 2013, a study indicated that commercial and residential buildings in Taiwan account for 40% of the country's energy consumption [13]. The energy department in the United States has also mentioned that the energy consumption of buildings in industrialized countries can be up to 40% [14], [15].

Buildings lose heat through their external structure, or thermal envelop. The most heat leakage occurs in windows, as they have the lowest thermal resistance. Previous studies have emphasized that the effective heat loss in windows is caused by the glazing. Ahmed et al. [16] mention that windows have the weakest thermal insulation in buildings. The authors investigated the energy savings of different kinds of glazing. The results showed that adding a tint to the traditional glazing can save up to 8.9 % of cooling loads. Pavlenko et al. [17] cited that the efficiency of energy in a building can be determined by the windows; however, the thermal performance of windows is defined by the U-value, or the overall heat transfer coefficient.

Respondek et al. [18] investigated the influence of climate change on the insulation of gas injected double-glazed windows. The gas between the panes decreases the thermal conductivity of the window. However, the study revealed that the increase in atmospheric pressure can decrease the insulation of the gas, leading to an increase in heat loss of up to 5%. Bahadori-Jahromi et al. [19] cited that 60% of overall energy loss in façade buildings is caused by windows. The study employs solar window films in a hotel in the UK to analyse their influence on the energy efficiency of the hotel. The findings revealed that using solar films can save up to 35% of cooling energy consumption in the building. Prapotnik Brdnik [20] modified the optical properties of the glazing used in three buildings in Slovenia. The modification was made by tuning the values of emissivity, transmittance, and reflectance of the glazing. The objective of the study is to reduce the solar heat gain coefficient of the glazing. The results showed that the optimum value of emissivity for the interior pane (of a

double-glazed window) is 0.03. The modified optical properties led to minimal solar heat gain and minimal cooling and heating loads.

Various factors influence the energy consumption of buildings, including the type of glazing used. According to a study, the choice of glazing can have a significant impact on energy consumption, with a reduction of up to 40% observed in a modelled energy system. This change also led to a 30% reduction in carbon dioxide emissions [21]. However, replacing glazing in existing buildings can be expensive. Another study highlighted the importance of considering factors such as glazing type, window orientation, and glazing dimension during the design phase to achieve optimal energy efficiency [22]. However, once construction is complete, it may be difficult or not possible to modify the direction of the building to improve energy efficiency.

Research has indicated that the window-to-wall ratio (WWR) of a building's glazing has a direct impact on energy consumption. Research has demonstrated a correlation between the window-to-wall ratio (WWR) and the amount of energy necessary to operate heating and cooling systems in a building [23], [24]. Another study conducted in Lebanon investigated the impact of different WWR ratios in four directions and found a significant impact of WWR on energy consumption per year [25]. Just like building direction, the WWR ratio should be taken into account during the initial stages of installation, as modifying it after construction can be challenging and expensive.

In summary, buildings consume an effective energy percentage around the world. Windows cause massive heat loss in buildings because of their high thermal conductivity of the glazing. Glazing type and size, window orientation, building location, WWR ratio, and other parameters influence the heat loss through windows. Numerous studies have tried to optimize the thermal performance of windows. However, more research is needed to mitigate the impact of windows on energy consumption, less CO2 emissions, and better thermal comfort for the occupants.

2.2 Comfortable environment in commercial buildings

2.2.1 Thermal comfort (temperature, ventilation, and air quality)

Due to the replacement of natural green zones with urban ones, ventilation inside cities becomes less effective. In addition, the structure of buildings has the ability to absorb much of the heat from solar radiation. The reasons mentioned have a negative impact on thermal comfort in indoor environments. Thermal discomfort causes health problems for the occupants. Further, it inflates cooling and total annual energy consumption and leads to an increase in the emission of CO2 [26]. Therefore, recent research has focused on studying the factors that directly influence the thermal comfort of buildings to mitigate their effects on occupants and energy efficiency.

Mao et al. [27] proposed a computational fluid dynamics (CFD-based) simulation method to determine the optimum room dimension to achieve thermal comfort, ventilation, air distribution, and other factors. The computations give a maximum room size of 6 m^3. Laouadi et al. [28] presented a healthy temperature standard in the internal environments of buildings. The proposed model takes into account both the simulation of buildings and human bioheat. The purpose of the study is to avoid body drought in older adults during seasonal overheating waves. The obtained criteria can be used in future research to evaluate the hazard of seasonal temperature increases on buildings' occupants. Chen et al. [29] proposed a deep learning-based algorithm to regulate the air source to a fan coil unit in an office building in China. The fan system is used as an air conditioning system in the building. The suggested algorithm controls the quantity of the supplied air to maintain a comfortable temperature and humidity level. Compared to the traditional controllers, the proposed algorithm increases satisfaction rates for the temperature and humidity inside the building by 12.66% and 9.5%, respectively. Sekartaji et al. [30] analysed the thermal comfort of a school in Japan after installing an air conditioning system to avoid the impact of the sun on the health of the students. The method was done through a questionnaire, and the result shows the preferred cooling temperature is under 28°C with a thermal comfort percentage of approximately 75% for the indoor environment. Lamsal et al. [31] reviewed a number of studies from different countries that are done on thermal comfort. The study focused on buildings that rely on natural ventilation to maintain acceptable thermal comfort. The result shows that the required range of indoor temperature is 17.6 to 31.2°C. Yaacoub et al. [32]

reviewed the recent machine learning-based methods that manage thermal comfort inside buildings. The results showed that employing machine learning enhance the thermal comfort of the building and saved up to 27% on overall energy consumption. Cheng et al. [33] discussed the influence of thermal comfort on the psychological factors of young people in varied environments. The results revealed that cold environments have more impact on people than hot environments due to the nature of human bodies. Sedighi et al. [34] reviewed the utilisation of bioactive glazing for façade buildings. This kind of glazing is adaptive to sustainable systems due to its shading features, solar radiation absorption, and thermal insulation. The properties of bioactive glazing can reduce the overall consumption of buildings, and hence, they achieve an effective energy savings of up to 30%.

To sum up, thermal comfort has a direct impact on human health and psychological parameters of people, energy consumption, and CO2 emissions. Therefore, it is essential to optimise thermal comfort in buildings to mitigate the inflation of energy consumption and to provide healthy environments.

2.2.2 Visual comfort

Windows are an integral component of a building's structure, as they contribute significantly to the overall envelope. Their primary function is to provide natural light for the indoor environment and ensure that the occupants have an adequate visual experience. Visual comfort impacts energy consumption in buildings. For instance, in a hot region, less transparent glazing provides adequate daylight for indoor environments and less need for artificial lights [35]. In contrast, more daylight causes a greenhouse effect, which inflates the consumption of cooling loads. In general, the overall consumption of a building will be higher. Studies have been done on assessing and optimising visual comfort in buildings to mitigate the consequences of energy consumption and discomfort glare [36]–[38].

In a study by Day et al. [39], 5031 people in the United States were surveyed to determine their level of satisfaction with the visual comfort of their surroundings in Three distinct edifices. The buildings utilised different techniques, such as automatically controlled blinds, electrochromic glazing, and roller shades, to limit the amount of daylight entering the buildings. Results showed that occupants in buildings 1 and 2, which had the most bright places, reported higher levels of satisfaction and contentment. Additionally, occupants'

satisfaction level was found to be directly proportional to their proximity to the windows. Nonetheless, inhabitants of the third building experienced the least amount of brightness as a result of the implementation of electrochromic glazing, provided negative feedback. Overall, the study highlights the importance of providing adequate daylight in buildings to ensure occupant satisfaction and comfort.

Lim et al. [40] investigated how an artificial light-controlled system can affect energy consumption and occupant behaviour in two distinct offices. The first workplace had access to daylight, while the second workplace did not. The study found that using the suggested lighting system in the first workplace resulted in a significant decrease of 78% in lighting energy consumption. In addition, the employees in the two offices reported high levels of satisfaction with the brightness of the environment.

Sorooshnia et al. [41] optimized the visual comfort of a building in Australia for minimal energy consumption. For the north-oriented rooms, it is found that an optimum window to wall ratio (WWR) of 10.7% to 20% provides maximum daylight in the internal environments, leading to and approximately 12% reduction in the overall energy consumption. For the west direction, setting the WWR to 51% led to a 50% energy savings in lighting loads. For south-oriented windows, 39% is the optimum WWR for the minimum possible energy consumption.

Fakhari et al. [42] investigated the ratio of daylight to overall available light in the indoor environments of six buildings in Iran. The study surveyed occupants satisfaction with the light in a number of places inside the buildings. People who stayed in places with a daylight to light ratio of 56%-80% were satisfied. However, in places with a daylight to light ratio less than 40%, people expressed their dissatisfaction.

Overall, visual comfort is essential for human well-being in buildings. It is directly related to the quality of daylight accessed in indoor environments. However, much daylight may cause an increase in overall energy consumption, it also mitigates the use of artificial lights. With non-fixed visible transparency glazing, the transparency level may determine the daylight quality and, hence, the energy consumption of a building. Therefore, it is crucial to determine to what extent it is useful to minimize transparency. Daylight quality was assessed by time consuming survey methods and gathering people's preferences in a building.

2.2.3 Vision through windows

The trend of conducting large-scale studies on windows has brought about certain challenges, including the issue of vision comfort. This pertains not just to the amount of daylight present in interior spaces, however, it also correlated to the quality of vision via the windows. Therefore, it is essential to comprehend both the quality and quantity of daylight in buildings to ensure the comfort of occupants. In terms of visual comfort, there are three critical components to consider: daylight glare (DG), correlated colour temperature (CCT), and colour rendering index (CRI) [43]. However, these components only account for visual comfort in a static scenario where the glazing maintains a constant level of transparency. The use of switchable glazing, such as the recently founded thin films that alter transparency, presents additional challenges when evaluating vision comfort.

Over the years, a plethora of research studies have been conducted to analyse the influence of daylight on buildings and improve both daylight efficiency and visual comfort, in both ongoing and upcoming building projects [44]–[46]. One such study was carried out by Wang et al. [47], who investigated the impact of exterior scenes provided by windows on the post-operative recovery of patients in Taiwan. The study revealed that enhancing visual comfort through the windows led to a substantial decrease in the usage of pain medication. This finding suggests that access to natural light and a view of the outside world can have a positive effect on the physical and emotional well-being of occupants, and reducing their reliance on pain medication can also have significant benefits. This study highlights the importance of incorporating effective daylighting strategies in building design to improve the indoor environment for occupants.

According to Fikfak et al. [48], the view from a window has a significant impact on the well-being of occupants in buildings. In a survey conducted by the authors, it was found that the type of view from a window played a crucial role in determining the preference of occupants. The survey involved people from different buildings with various types of views, and it was observed that views of green nature and high-quality outdoor scenes were highly favoured by the respondents. This study underlines the importance of incorporating windows in building design to provide occupants with access to natural elements such as greenery and picturesque landscapes. Such views can significantly contribute to enhancing the overall well-being and satisfaction of occupants in buildings. In their research, Pilechiha et al. [49] presented a novel approach for minimizing energy usage in the windows of office buildings.

The authors laid emphasis on the fact that this new method should not have any adverse impact on the quality of vision via the windows or the amount of daylight entering the building. This approach has the potential to significantly improve the energy efficiency of office buildings while simultaneously ensuring a comfortable and healthy indoor environment for the occupants. In conclusion, the study considered vision through the window as an important factor that must not be effected while modifying the window system. The study conducted by Dušan et al. [50] put forward a distinctive method for designing lighting systems in industrial buildings. The authors emphasized that, in addition to ensuring that there is sufficient natural daylight within the workspace, it is equally important to provide workers with access to the external environment to enhance their productivity and performance. This proposed approach recognizes that the physical and mental wellbeing of employees can be positively influenced by the visual and sensory connection to the outdoor environment.

Apart from the aforementioned research, several other papers have explored the functions of windows and their impact on various categories of individuals, such as students, employees, workers, and patients. These studies have consistently highlighted that the fundamental purposes of windows are to provide adequate daylight and maintain a clear vision of the exterior environment [51]–[53]. They emphasize that having access to natural light and the outside world not only enhances the physical and emotional well-being of the occupants but also boosts their cognitive and visual abilities. Therefore, it is essential to incorporate windows into the design of buildings in a way that maximizes their functionality and benefits for the occupants.

Over a duration of six months, Ma et al. [54] conducted a survey to assess the preferences of a group of students on visual comfort and discomfort glare in a study area. After conducting the survey, they used the data they collected to create a building information model (BIM). They then converted this BIM into an algorithm that could be used by a machine learning system. The resulting algorithm was used to control a proposed window shading system. This approach enabled the researchers to develop a customized window shading system that could adjust to the changing lighting conditions and user preferences over time. The use of machine learning and BIM technologies allowed for a more efficient and accurate system design, resulting in improved occupant comfort and energy efficiency in buildings. This study

highlights the potential benefits of integrating advanced technologies and user feedback in building design to optimize occupant comfort and energy consumption.

The studies mentioned previously, as well as other investigations [55]–[57], relied on the subjective observations of individuals to assess visual comfort in various settings, taking into account both the amount of natural light available and the quality of the view through the window. However, this approach typically involves administering questionnaires, which can be a time-consuming method for gathering information about human preferences over different seasons. Additionally, there is no guarantee that the collected data will be comprehensive enough to address all the potential user requirements in real-world situations. Therefore, this method may have limitations in terms of practicality and accuracy.

In a study conducted by Detsi et al. [58], the energy consumption of lighting, cooling, and heating loads in office buildings situated in Athens and Stockholm was investigated. The authors recommended the use of a triple-glazed window that featured thermochromic, electrochromic, and low-emissivity (low-e) coatings in insulated glass units (IGUs) to improve the energy performance of buildings. According to the study, the proposed window provided a high level of visual comfort for workers in terms of the daylight glare index. As a result, it was observed that the recommended window led to energy savings of 18.5% and 8.1% annually in Athens and Stockholm, respectively. The visible transparency of the window ranged from 0.46 to 0.75, but the study did not evaluate the quality of external views within this range of transparency.

Ko et al. [59] conducted a study that investigated the performance of a suspended particle device (SPD) window in an office building located in South Korea. The research method involved manipulating the visible transparency of the window by adjusting the applied voltage of the SPD film, which had a corresponding effect on the solar heat gain coefficient (SHGC) of the window. The researchers found that the controllable range of SHGC was between 0.11 and 0.45. The study reported an annual energy savings of 4.1% due to the use of the SPD window. However, the researchers also observed that lowering the visible transparency of the window to save energy had an adverse effect on the clarity of the outside view for the occupants, potentially compromising their visual comfort. The study implies that while the SPD window technology can offer significant energy savings, it may not be suitable for all applications, particularly in situations where occupants' visual comfort and outdoor views are of utmost importance.

Oh et al. [9] conducted a study to investigate the effectiveness of various types of PDLC (Polymer Dispersed Liquid Crystal) thin films applied to windows and façade walls in terms of energy consumption and daylight performance. The researchers found that integrating PDLC thin films with existing windows resulted in energy savings ranging from 3.1% to 17%, and also improved the discomfort glare ratio of the indoor environment. However, the study did not consider the possible impact of reducing the visible transmission of light through the window after adding the PDLC film on the quality of vision of the outdoor views. While the results of the study are promising, it is important to note that the use of PDLC thin films may affect the clarity of outside views, which could potentially compromise the visual comfort of building occupants.

Hemaida et al. [60] conducted a study to investigate the impact of using PDLC windows in office buildings located in Riyadh, Saudi Arabia, and London, UK, on the cooling and heating consumption. The study found that the use of PDLC windows resulted in a reduction of 12.8% in cooling capacity in Riyadh and a decrease of 4.9% in heating capacity in London, indicating that the suggested window is more effective. The study also concluded that the PDLC window provided an adequate amount of daylight for internal spaces. The findings indicated that the window provided 75.8% of the annually required daylight glare in Riyadh and approximately 63% in London. However, the study did not analyse the impact of reducing the glazing's visible transmittance on the vision via the window, even though the visible transmission of the window varied from 44% in the OFF state to 79% in the ON state.

Previous research has primarily focused on assessing vision comfort in internal environments by measuring available luminance, particularly through the use of dynamic windows. The evaluation of visual access to the outside environment through windows has been limited to human surveys and preference analyses. However, with the emergence of switchable films and glazing with dynamic optical and thermal properties, it is crucial to investigate and assess various factors to determine the true impact on visual comfort. Proper evaluation is necessary to accurately understand the effects of these new technologies on vision comfort. This poses a challenge to surveying and traditional evaluation methods. Therefore, if artificial intelligence is employed to control window settings, the accurate measurement and quantification of visual comfort are essential, and it is important to develop algorithms that can precisely parameterize it.

Previous studies have indicated that human visual perception is highly reliant on the contrast of images, which allows the human eye to distinguish between adjacent objects in an image. Consequently, when assessing the quality of vision through glazing, it is possible to use an artificial vision system to calculate the contrast value in real-time. This value serves as an accurate representation of the quality of human vision and is critical in evaluating the effectiveness of dynamic windows and switchable films. Such systems enable accurate measurement of the contrast value, which is a crucial aspect of human vision perception, and thus provides a more effective approach to evaluating the quality of vision through glazing than traditional survey methods.

Previous studies have utilised image processing methods to assess various aspects of daylight in indoor environments, such as the daylight glare index and discomfort glare index. These methods involve using digital images of the environment to determine the luminosity histogram, which reflects the brightness level and luminance of different points in a given area. Several studies have been conducted to evaluate the daylight performance of different environments. For instance, Fan et al. [61] simulated an image-based gymnasium to determine the daylight level, while Hegazy et al. [62] utilised luminosity histogram analysis in a virtual environment to quantify the daylight. Futagami et al. [63] used an image-based motion sensor to determine the luminance level in a workplace. Additionally, Day et al. [39] captured high dynamic range (HDR) images of three office buildings and analysed them using the Evaglare algorithm [64] to evaluate the daylight illuminance and glare probability. However, all of these studies didn't examine the visual quality of the external views through PDLC glazing. Nonetheless, previous research has highlighted that windows serve as a crucial means of providing occupants with visual linking to the exterior environment.

Unfortunately, most previous research has failed to evaluate the visual aspect of windows, with some studies resorting to conducting surveys to assess individuals' preferences regarding the vision through windows. Nevertheless, surveys are often time-consuming to involve weather conditions throughout all seasons, and the resulting information may not accurately reflect the diverse preferences of real-world users. Moreover, with the introduction of thin-film technologies into the window industry, As windows with variable optical transmittance features are becoming more common, relying solely on surveys to evaluate vision through windows is no longer a practical approach.

At this point, one might ask how to mathematically describe the level of visual quality through a window. Unfortunately, the literature suggests that the quality of vision from the perspective of occupants towards exterior views is not yet a measurable parameter. Another question that arises is what is the minimum level of visible transparency required to maintain an acceptable level of visual quality through the window when a thin film, such as a PDLC film, is added to conventional glazing? Previous studies have focused on reducing the transparency of smart films to save energy in hot regions without exploring the impact on visual comfort through windows. However, in chapter four of the thesis, a new methodology will be introduced to quantify the quality of vision through PDLC windows and determine the minimum level of transparency required for the glazing to maintain acceptable visual quality.

2.3 Smart windows

2.3.1 Smart windows versus traditional windows

In recent years, the window industry has experienced a surge in new technologies that utilise innovative materials to improve or replace traditional glazing. These materials include semi-transparent photovoltaic panels (STPVs), suspended particle device (SPD) films, electrochromic films, and polymer dispersed liquid crystal (PDLC) films, all with unique optical and thermal characteristics that set them apart from conventional glass. When incorporated into glazing, these panels and films bring new dimensions to be considered, as some of them possess controllable optical and thermal properties that can be adjusted to suit specific building requirements [8], [65]–[69]. These innovative materials have the potential to significantly enhance the energy efficiency and comfort of buildings, making them a key area of interest for the window industry.

Traditional windows in commercial buildings are no longer static components of the building envelope. In recent years, a variety of studies have suggested new designs and modifications to turn windows into "smart" elements that can perform a range of functions [70]. These new types of windows play an important role in improving the overall living environment for building occupants. They also have the potential to enhance renewable energy systems, since they provide improved thermal and daylight efficiency [71]–[73]. Furthermore, some windows are being used to generate electricity in the form of building-integrated photovoltaic windows [65].

In a research conducted by Ghosh et al. [43], the authors investigated the daylight efficiency of building-integrated photovoltaic (BIPV) windows in an office building located in Saudi Arabia. The study findings suggested that a transparency range of 50% to 70% was sufficient to maintain a comfortable glare level during the winter, whereas for summer, a transparency level of 70% was required. However, rising the transparency level to 90% leaded to a high level of daylight inside the building, but it also led to high discomfort due to glare. The research indicates that achieving the right balance between transparency and glare is important for the optimal daylight performance of BIPV windows in commercial buildings.

In their study, Guo and Zhang [74] used a window with multiple layers of glazing as a means of recovering heat. They achieved this by directing exhaust air from the interior environment to ventilate the window, which improved its ability to regulate temperature. Overall, their

approach resulted in a significant energy savings of 38.2%. The study shows the advantages of smart windows that used a developed ventilation technology to enhance its thermal performance and saving an effective percentage of energy compared to traditional windows.

Kim et al. [75] conducted a study aimed at optimising the physical properties of an electrochromic smart window, in order to achieve maximum energy savings. They discovered that when the electrochromic glazing was installed in a window facing south, it was able to reduce the amount of solar radiation that passed through the window. This resulted in a maximum annual energy savings of up to 45%. Meanwhile, in another study, Olivieri et al. [76] focused on investigating the thermal, daylighting, and electrical performance of semi-transparent photovoltaic (STPV) windows. These windows were made with different levels of visible transparency, ranging from 10% to 40%, and different solar heat gain coefficients (SHGC) ranging from 0.655 to 0.734. The study found that the efficiency of electrical generation increased as the transparency decreased. However, this also resulted in a reduction in the illuminance of the interior environment.

In conclusion, various methods are employed to upgrade conventional windows with new and improved features. These new windows possess different characteristics that are crucial in enhancing the overall performance of their predecessors. They exhibit lower thermal conductivity, can generate electricity, have shading properties that mitigate discomfort glare, and can reduce greenhouse gas emissions. Smart windows offer the added benefit of reducing energy consumption, making them suitable for sustainable buildings and minimizing CO2 emissions. Additionally, smart windows are highly adaptable to automated systems and artificial intelligence, which enables them to be easily controlled and monitored. This allows for the creation of comfortable environments for occupants through smart controllability and observability of the windows.

2.3.2 Ventilated windows

As indoor activities of occupants in buildings have increased, there has been a growing interest in managing ventilation systems to maintain air quality [77], [78]. This has resulted in the recent widespread adoption of mechanical forced ventilation systems over natural ventilation [79]–[83] as a means of achieving this goal.

Alternatively, a number of studies have explored the possibility of using the entry and exhaust air of ventilation systems to provide it to the gap of multi-pane glazed windows. The main benefit of this approach is to heat up or cool the window cavity, which in turn can help to reduce thermal loss through the windows. For example, one study investigated a type of window known as a phase change material (PCM) ventilated window, which utilises a material that can absorb or release energy when its physical state is changed (usually from liquid to solid or vice versa), allowing it to offer heating or cooling effects. The study utilised a PCM heat-exchanger to pre-heat or pre-cool a double-glazed window and found that when the window operated in heating mode, the temperature of the inlet air was increased by 2°C over a 12-hour period during the day, while in cooling mode, the inlet air temperature was lowered by 1.4°C over a 7 hour period during the day [84].

Other researchers have found alternative methods to improve the thermal performance of windows. One such method involves utilising fresh air or warmed exhausted air and injecting it into the space between the panes of double-glazed windows, which helps to reduce the window's heat transfer coefficient. In the studies carried out by Lago et al. [85] and Zeyninejad et al. [86], a solar reflective film was applied to a double-glazed window to evaluate the thermal performance of the proposed system. Lago et al. concluded that a spacing of 25mm between the glazing layers is the most suitable for achieving the minimal heat loss throughout summer.

Michaux et al. [87] conducted a study to examine the thermal efficiency of a triple-glazed ventilated window and compared it to traditional double-glazed and triple-glazed windows. The study found that the use of the triple-glazed ventilated window resulted in a reduction in heating loads by 5% at night and 90% during the day. In another research conducted by Liu et al. [88], fifteen different types of windows were placed in an area to assess their energy efficiency and thermal comfort in the space. The study showed that using ventilated windows can improve thermal comfort and reduce the consumption of heating and cooling loads.

Furthermore, in a research article by Lollini et al. [89], a dynamic glazing system was put forward that is capable of reacting to external environmental stresses, such as U-value, g-value, spacing airflow thickness, and airflow rate. The primary objective of this system is to ensure optimal efficiency and effectiveness of the glazing in diverse weather conditions.

In a study conducted by Behrouz Nourozi et al. [90], a unique approach was presented to decrease the thermal conductivity of a window, which was subsequently validated using simulations. This approach includes a double-glazed window that is filled with Argon gas and is enclosed between two coated glazing panes. In addition, a heat exchanger is used to provide warmed air to the window while simultaneously directing the waste warm air from the building towards the heat exchanger to enhance its efficiency. The simulation results revealed that if the temperature of the air supplied by the heat exchanger is greater than the ambient temperature of the room, the U-value of the window could be lowered to less than 0.65 $W/m^2.K$. However, this innovative design incorporates extra components that increase the complexity of the structure and consequently, the cost of installation. Additionally, in instances where a building's facade possesses a high WWR (window-to-wall ratio) and employs multiple-glazed windows, the available waste air may not be sufficient to warm up the large space between the window panes.

Zhang et al. [91] conducted a study to compare the efficiency of a regular triple-glazed window with a triple-glazed ventilated window, which operates in heating and cooling modes by utilising the waste air from the room to be directed into the window. The study aimed to investigate the potential energy savings achieved by the exhaust window compared to the conventional one. The results indicated that the ventilated window had the potential to decrease the heating and cooling loads by 50.1% and 25.3%, respectively, when compared to the regular window. However, the study also mentioned that the amount of air required to maintain the same level of energy savings would increase with the window's size. The study presumed that the waste air source would be available continually, which may not be the case in practice.

Previous studies on ventilated windows employed the heat transfer coefficient or U-value to assess the thermal efficiency of the windows. The U-value was typically obtained through experimental measurements conducted under steady-state conditions, involving the assessment of temperature variations between the window's two sides. Moreover, it was

essential to conduct the experiment without considering the influence of solar radiation-induced heating [92]–[95].

The studies mentioned earlier in this context had varying methods to supply air to the space between the panes of the window. Some of them heated up fresh air from outside before release it into the room whereas others expelled room air to the outdoors through the gap in the window to heat the panes in winter or cool them in summer. From these studies, it is evident that wasted air can be utilised as an important resource to achieve maximum energy efficiency in buildings. Previous research works assumed that there is an unlimited supply of waste air that can continuously be used to power the ventilation systems and minimize heat loss through windows.

However, in some situations, the amount of waste air in a building may be less than the expectation. According to ASHRAE, a recommended amount of 5 and 4.2 cubic feet of air per minute per person is necessary to be replaced with fresh air in large-scale and small-scale buildings, respectively. Additionally, a minimum air change per hour of 0.35 is also recommended [96]. Thus, the amount of available waste air is limited by the number of occupants in a building. As a result, buildings with fewer occupants may not be able to provide sufficient air flow for ventilated windows. Furthermore, the needed amount of waste air in a building is dependent on the space capacity between the panes of the ventilated multi-glazed windows, which is a function of the window dimension and number of panes. For ventilated windows with a high Window to Wall Ratio (WWR), particularly in façade buildings where the WWR can be as high as 70% [97]–[99], or even more, the need for waste air will be significant. Considering a (1 m^2) ventilated window proposed by Nourozi et al. [90] for a very cold climate, the required flow rate for the waste air is up to 11 L/S. If this window is utilised in a (4 x 3 x 2.5 m^3) room in a façade building with a wall area of (4 x 2.5 = 10 m^2). In façade buildings, the window to wall ratio WWR can be up to 100% [101]. Hence, 10 ventilated windows will be needed with 10 inlets; each inlet requires (3.96 m^3/h) of wasted air, or totally (39.6 m^3/h). According to the ASHRAE standard, the lowest air change per hour is 0.35 [102]. Therefore, the attainable resource of waste air per hour from the room is (4 x 3 x 2.5 x 0.35 = 10.5 m^3/h). Obviously, there is a shortage of wasted air supplied by the room, and the performance of ventilated windows will be effectively degraded.

In conclusion, previous studies have shown that waste warm air in buildings in cold regions can be utilised through ventilated windows to achieve significant energy savings. However, these studies did not address the issue of optimizing the usage of waste air in ventilating windows for buildings with a high WWR ratio, such as façade buildings in cold regions. To address this issue, Chapter Three proposes an experimental methodology to optimize the usage of waste air in ventilating windows.

2.3.3 Polymer dispersed liquid crystal windows

Polymer dispersed liquid crystal (PDLC) thin films are smart films that can change their optical state electrically. PDLC films have randomly oriented “nanoparticles” in their normal state. When an external energy source is applied to a PDLC thin film, the nanoparticles are oriented in one direction. The uniformity of the nanoparticles changes the optical transmission state of the PDLC film from opaque to transparent [103], [104]. A study [105] analysed the evolution of optical transmission of a PDLC film against an AC excitation. The curve showed that the examined PDLC film has less solar transmission than luminous transmission. This feature makes the PDLC film an effective addition to conventional glazing. If a PDLC film is added to normal glass, an effective portion of solar radiation can be eliminated while maintaining an acceptable visible transmission. The shading effect of PDLC films reduces the impact of greenhouse. On the other hand, higher luminous transmission ensures comfortable vision through the glazing. The investigations on PDLC films showed that the optical transmission varied while increasing the excitation. The visibility of PDLC films is very low with low excitation and starts growing before reaching a saturated value [106]. The variation of visible transmittance against the input voltage can be exploited in practical applications. Practically, a curtain transparency level could bring a balance between the visual comfort in a building and the energy consumption [107]. A study revealed that the operating temperature of PDLC films can be up to 90°C before their electrical-optical characteristics start deforming [67]. Another study concluded that PDLC films can work normally within a temperature range of -20 to 80°C [108]. This is another merit that makes PDLC films are suitable for hot climate zones.

Therefore, PDLC windows are feasible to employ in buildings for higher thermal isolation compared to traditional glazing. PDLC films can be attached directly to the old glazing of a building; in contrast, other kinds of smart glazing require a full replacement, such as electrochromic glazing [109] and semi-transparent photovoltaic panels [110]. Numerous studies have shown the impact of utilising the PDLC windows on eliminating the discomfort glare and mitigating annual energy consumption. Oh et al. [9] remodelled an old building after attaching PDLC films to the existing glazing. The simulation result emphasised that the PDLC films can reduce the annual consumption and discomfort caused by daylight in the building. Gosh [111] investigated the thermal performance of a developed glazing where a PDLC film is sandwiched between an acrylic sheet and a glass pane. An experiment was carried out on the three panes to measure the heat transfer coefficient (U-value) and solar heat gain coefficient (SHGC). The experiment showed that the U-value for the PDLC film in transparent and opaque states is approximately 1.1 $\frac{W}{m^2K}$. In addition, the SHGC coefficient of the PDLC film is 0.45 in the transparent state and 0.23 in the opaque state. Shaik et al. [112] achieved an experiment on four coloured samples of PDLC films to measure the visible and solar characteristics. The PDLC films were applied to a simulated library building in a hot climate zone. Simulation results showed a maximum saving in the case of white PDLC film of more than $8K in cooling loads when it works in the transparent state. The reduction in energy consumption can mitigate CO2 emissions by approximately 100 tCO2 annually. The results also showed adequate daylight for the internal environment of the library. Another study [113] concluded that employing PDLC windows for a building in Saudi Arabia can save at least 21% of the cooling and lighting loads annually. Consequently, a reduction in CO2 emissions of up to 89 $\frac{kgCO2}{m^2}$ can be achieved. The experimentally calculated overall heat transfer coefficient of the utilised PDLC film is approximately 5 $\frac{W}{m^2K}$ in ON and OFF states. Further, the experimental results showed that the SHGC of the PDLC film is 0.39 in the off state and 0.53 in the on state. The luminance inside the simulated building was calculated for different window to wall ratios and orientations. The calculations revealed adequate daylight in the building (up to 300 lux annually) while the PDLC is in ON (maximum designated visibility). In contrast, the simulation showed a discomfort glare spaces when the PDLC film is in the off state and the SHGC is low. Iluyemi et al. [114] investigate the energy savings that can be achieved using electrochromic and PDLC windows if they are applied to a residential building

in Oman. The findings revealed that using electrochromic windows can save 23% of the overall annual energy consumption. On the other hand, in the case of a double-glazed window that has a silver inner pane with a PDLC film, an energy savings of 22% can be realised.

In summary, utilising PDLC films is a feasible option to enhance the overall performance of buildings' windows located in hot regions. In hot climates, solar heat gain coefficient (SHGC) has a better indication of the overall performance of windows than heat transfer coefficient (U-value) [112]. Adding PDLC films to the existing glazing minimises solar heat access to the internal environments and simultaneously maintaining sufficient daylight. As a result, an effective reduction in the cooling and overall consumption of buildings can be realised. Further, less SHGC compared to conventional glazing mitigates the discomfort glare. Overall, PDLC films fit the target of sustainable buildings and ensure high quality environments for the occupants.

2.4 Smart windows controllers

2.4.1 Implementation of embedded controllers for smart windows and industrial applications

The advanced features of smart windows require specific algorithms to perform their intended functions. These algorithms can be executed through dedicated software and hardware components. Previous studies have utilised diverse implementation strategies to implement the control functions of smart windows. Ismail et al. [115] used FORTRAN programming language to create a numerical code on a PC in order to evaluate the thermal efficiency of three different window designs. However, more efficient programming languages, such as open-source C-language, which is commonly used in modern embedded systems, have been suggested [116]. Other studies utilised the MATLAB software tool [117] to implement their developed algorithms, which were used to estimate the visible transmittance level of polymer dispersed liquid crystal (PDLC) windows [118] or to regulate the functioning of multi-layer ventilated windows [119], [120]. Despite this, the use of standalone embedded systems [121] is necessary for industrial applications in order to eliminate the need for PC-based software. As an example, Dobrojevic and Bacanin [122] implemented a smart home control system using a Raspberry Pi-based embedded system [123] and the Python programming language [124], which leveraged the Internet of Things (IoT) technology. In another instance, Elkholy et al. [125] developed an energy management system for a hybrid microgrid, based on a field programmable gate array (FPGA). The FPGA system demonstrated high responsiveness in adapting to changes in the load. Meanwhile, Kumar et al. [126] created a grid-interfaced solar photovoltaic (GIPV) system, incorporating an ARM Cortex-M4 core. The ARM core manages various peripheral devices, including the voltage source converter and the DC-DC boost converter, to enable the connection between the solar grid and the computer. Wang et al. [127] introduced a field programmable gate array (FPGA)-based adaptive power controller for DC-excitation polymer dispersed liquid crystal (PDLC) films. The system relies on a photovoltaic panel to supply the PDLC film. A DC-DC converter is fed by the solar DC excitation to provide a variable DC voltage to the PDLC film. The output of the DC-DC converter is determined by the pulse width modulated PWM signal. Real-time conditions like the illuminance and other parameters are read by sensors and fed

to the FPGA design. The online data is set as input to an algorithm that is executed by the FPGA design. The FPGA finally determines the level of the PWM signal that is matched with the given conditions. Hence, the generated level of the PWM signal determines the preferred transparency of the PDLC film. The result shows that the proposed algorithm requires 2.5 seconds to adjust the transmittance level of the PDLC film. Grygierek et al. [128] used the Python programming language with other simulation tools to analyse the influence of natural and mechanical ventilation in a house on thermal comfort and heating loads. The result shows accurate calculations by the Python language when compared with a similar system. Chekired et al. [129] used an Arduino microcontroller (MC) to build a cheap power management system for a family house in developing countries. The MC controls the charging of a battery from solar panels via a MOSFET via a PWM signal. The system helps minimise the lighting load and provides a remote control for home appliances for the occupants. Mobaraki et al. [130] proposed an Arduino MC-based, low cost monitoring system to measure and record the temperature in indoor environments. Implementation results show that the cost of the monitoring system can be reduced by up to 88% with an accuracy of 0.29°C to 0.42°C.

In certain scenarios, when the size of the processed data is relatively large, such as with images or videos, the use of embedded systems with high processing speeds is crucial. To address this issue, Liu and Feng [131] introduced a developed object edge detection algorithm that utilises a special SoC FPGA-based hardware platform known as Zynq. This algorithm takes advantage of the hardware acceleration blocks present in FPGA chips to enhance the speed of processing. Jaskolka and colleagues [132] highlighted the impressive potential of the Raspberry Pi 3 SoC system to execute various tasks related to image and video processing. They suggested that this system could replace the MATLAB-based implementation approach. Moreover, the Raspberry Pi 3 is a cost-effective option that supports the use of Python, a freely available and open-source programming language. Pereira [133] presented four possible methods to execute an image processing algorithm for detecting cracks in buildings in civil applications. The scenarios included implementing the algorithm using MATLAB's image processing toolbox and without it, implementing it using PC-based C/C++ coding, and implementing it using Raspberry Pi-3. The processing time was calculated for each scenario to evaluate their effectiveness. The results showed that the shortest running time was obtained when the MATLAB image processing toolbox was utilised. In the field of English

vocabulary translation, Wang [100] suggested a neural network approach that utilises a FPGA Xilinx type chip, leading to a vocabulary detection accuracy of 98%. This accuracy is higher than the 92.35% accuracy obtained through the use of the FUZZY method.

Ahmad et al. [123] conducted a study that presented a novel approach for determining the cost associated with implementing a given function on an FPGA. This method was subsequently utilised to assess the FPGA implementation of various circuits, based on their respective latency and throughput. The findings of the study indicated that the latency and throughput of four mathematical operations were 2382 clock cycles and 0.178 Mega inversions per second, respectively. Paunski et al. [102] conducted a study that aimed to compare the performance of several single board SoC (System on a Chip) systems for automated applications. The study evaluated the operational performance of the Raspberry Pi-3, Rock64, and LattePanda systems under similar conditions. The results indicated that the LattePanda system consumed the least amount of power, at 3.6 watts, as compared to Raspberry Pi-3, which consumed 7.5 watts. Additionally, the Rock64 system was found to execute a face detection algorithm in 311 seconds, while it took the Raspberry Pi-3 system 757 seconds to perform the same task. These findings suggest that different SoC systems may possess varying levels of power consumption and processing speed, which must be taken into account when selecting a suitable system for a specific application.

In conclusion, previous research studies have utilised diverse approaches to realize controllers for various industrial applications, including smart windows. Each implementation method employs specific hardware and software based on the requirements of the application. Some suitable hardware options include System on-chip (SoC), PC-based systems, microcontrollers, and field programmable gate array (FPGA). Furthermore, programming languages such as C, Python, and Fortran have shown efficient performance compared to other programming languages. Key performance indicators for a controller include various parameters such as latency, throughput, power consumption, and cost. The latency and the throughput reflect the processing speed, while less power consumption and less cost are crucial factors that determine the controller's efficiency.

2.4.2 Image processing-based daylight evaluation (Image brightness and contrast)

The brightness is known as the total luminance in an image [134]. Mathematically, it represents the mean value of the pixels intensity in a digital image. However, the intensity of a pixel in an RGB image is the average of the red, green, and blue colour values [135]–[139]. The contrast indicates the disparity in luminance that makes things recognisable to human eyes [134]. Mathematically, it can be determined by finding the room mean square of the difference between local pixel brightness and global brightness of an image [136].

The traditional method to evaluate the daylight inside buildings is by using light sensors. However, in previous research, brightness was a property of digital images that was exploited to detect the visible light intensity in an environment. On the other hand, the contrast of a digital image is used to assess the visual comfort of indoor environments. Determining the real-time values of brightness and contrast for an environment scenes can reveal the quantity of the available light as well as the quality of vision [140]. The brightness of individual pixels in digital images reflects the quantity of daylight in a particular spot in a given environment. In contrast, relying on light sensors in the traditional method doesn't provide light intensity at every point. Further, light sensors can't reflect vision quality like contrast-based methods.

If an automated system with a digital camera is employed to detect the spatial daylight intensity inside a building spontaneously, an intelligent system can act as an external observer on the windows. Artificial intelligence evaluates the overall performance of windows instantaneously. Consequently, the adjustable factors that impact window operation can be tuned to maintain optimum performance and a comfortable visual environment.

Wang et al. [137] cited that relying on the detection of visibility from the image mimics the vision in human eyes. Zhou et al. [138] emphasised that if an image is taken in low-level light conditions, it may not be suitable for image-based luminance detection applications. Kim et al. [141] developed a method to detect the discomfort glare in an office building instantaneously. The method used a digital camera to capture high dynamic range images of outdoor scenes through the window. Based on image-processing, it is possible to measure the quantity of luminance, and the location of any external glare. The proposed method utilised a roller to shade the glare source in response to the glare detection action. The result shows that the shading process can mitigate the impact of discomfort glare and maintain

comfortable vision for the occupants. Jakubiec [57] proposed an image processing-based method to determine the value of discomfort daylight in an office environment. The method relies on taking online high dynamic range images of the environment under assessment. Image processing calculations estimate the brightness and contrast of the captured scenes. Then the discomfort glare probability DGP can be extracted, which reflects the spatial discomfort daylight in the office. In contrast, Bian et al. [142] emphasised that daylight glare probability does not accurately reflect the visual comfort of occupants. Therefore, the study proposed a contrast-based method to evaluate the visual perception of students while they are looking at a blackboard in the classroom in a luminous environment. The result shows that a contrast ratio over 1.3 measured for the blackboard reflects an undesirable reflected glare.

In summary, the previously mentioned studies relate the brightness and contrast of environmental scenes with the available daylight. In a similar manner, it is possible to determine the quality of external views through windows. For normal, fully transparent glazing, the quality of vision is guaranteed. However, this action could be useful for smart glazing, such as the polymer dispersed liquid crystal films, as the transparency is lower and challenges, the linking of occupants with the outdoor environments. On the other hand, since the quantification method for the vision through PDLC windows (in chapter four) is based on brightness and contrast analysis, it will be essentially necessary to implement an efficient controller to handle image processing calculations to realise the quantification process. This subject will be thoroughly discussed in chapter five.

2.5 Summary

In this chapter, the concepts of smart windows and their role in mitigating energy loss in buildings were discussed. Mainly, two types of smart windows were demonstrated. Firstly, ventilated windows that use the wasted air in buildings to warm the glazing and reduce the heat loss through it. This kind of smart windows faces a lack of wasted air challenge when it is employed for façade buildings in very cold environments, which reduces its thermal efficiency. In such conditions, special strategies for optimising the use of wasted air should be developed to overcome this problem and ensure the performance of the window. Secondly, polymer dispersed liquid crystal (PDLC) windows are used in hot regions to minimise the greenhouse effect on buildings. Although PDLC films have the merit of constraining the level of glazing transmittance, they have a negative impact on the quality of vision through the glazing. Another challenge with such kinds of windows is that vision quality through glazing has not been quantified by previous research. Therefore, two cardinal tasks are necessary for PDLC windows: quantifying the vision through PDLC films and defining the minimum level of transparency of PDLC films that ensures a minimum level of vision quality through the window. To realise these tasks, implementing a controller is essential to managing the operation of PDLC windows. Since vision through PDLC films is related to the instantaneous transparency of the film and the brightness and contrast of scenes, the controller should handle image processing calculations. Implementation techniques for embedded systems, in addition to efficient hardware and programming languages, were demonstrated. The challenge of implementing the controller for PDLC windows is achieving the given tasks in a short time to ensure an appropriate operation for the window in practical applications.

Chapter 3: Optimising the use of building's waste air in double-glazed ventilated windows for commercial buildings in cold regions

3.1 Introduction

As mentioned in chapter two, ventilated windows use the wasted air from buildings to warm up the panes of the glazing to lessen the heat loss through the window. Further, in some cases, the available resource of wasted air is not adequate to feed the window, and this degrades the thermal performance of the window. In this chapter, strategies for optimising the use of wasted air for ventilated windows are introduced. A multiple scenario experiment was carried out in a small scaled room to investigate the thermal performance of a double-glazed ventilated window. The proposed system, research method, experiment scenarios, and results were demonstrated. The proposed system was modelled using special software, and the simulation results were compared with the experimental results to show the validity of the system. The thermal efficiency of the proposed window was evaluated based on the heat transfer coefficient in different scenarios; therefore, the scenario that led to the optimum utilisation of wasted air was pointed out.

3.2 Research method and experimental setup

3.2.1 The proposed system

Figure 3. 1 illustrates the suggested ventilated window that will be utilised to carry out the experiment. A test room was fitted with a ventilated double-glazed window. A different small and thermally insulated room was utilised to produce warm air, which served as the waste air production room while executing the experiment. The room also contained an integrated microcontroller heating system to regulated the temperature of the air. An amount of fresh air from the external environment will be injected into the room instead of the warm air taken during the execution of the experiment. In the test room, an air pump is used to introduce the warm air from the waste air room into the bottom entry hole of the ventilated window. Therefore, the air flows upwards towards the upper exhaust hole of the window and is released to the exterior environment. The waste air room and the ventilated window input and output holes are equipped with check valves to guarantee a unidirectional flow of air. As a result of the check valves, the air can only flow in one direction, preventing any backflow of air or unwanted mixing of air from the room and the outdoor environment.

Three operating styles can be recognised for the suggested ventilated window: (1) if the air between the glazing layers is maintained with no flow, the window behaves like a typical double-glazed window; (2) if the air between the glazing layers is replaced by warm room air at various intervals; or (3) continually, in which case the window will be switched to the forced ventilation operation. The three operating ways of the proposed ventilated window are covered in detail throughout the carried out experiments in the following sections, along with how various cases impact the window's thermal efficiency.

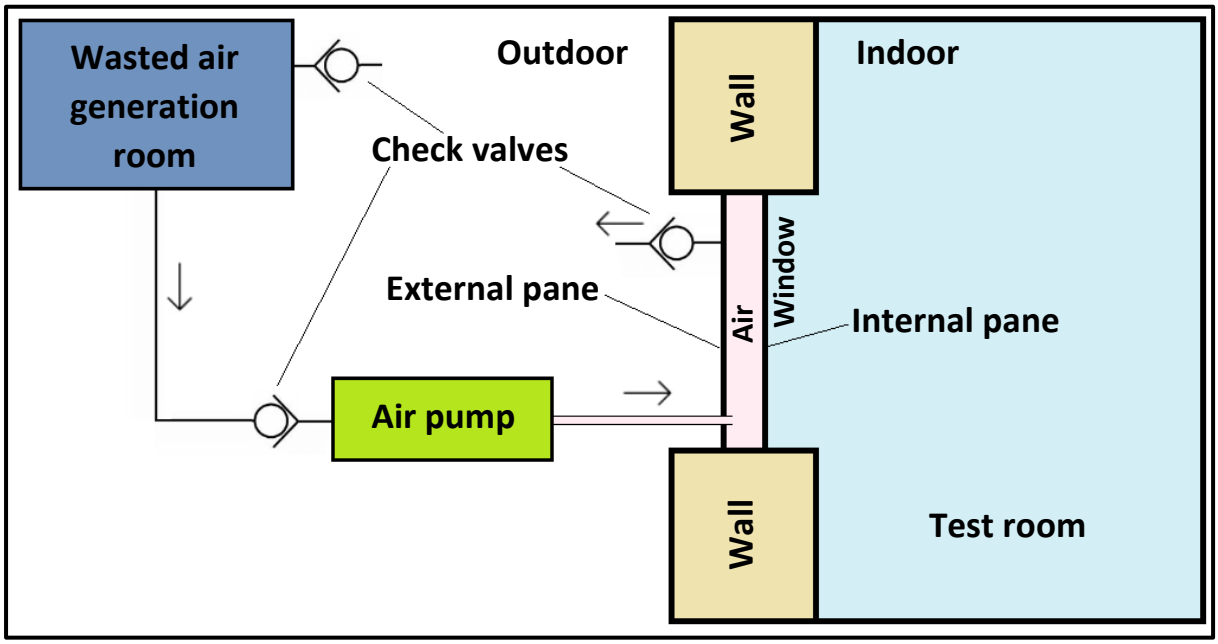

Figure 3. 1. *The proposed double-glazed window with the ventilation system.*

3.2.2 Methodology setup

The research methodology setup is depicted in *Figure 3. 2* and is employed to run the procedures, verify the validity of the experimental models, and assess the experimental results. It is important to note that the current system has been built using two main models. The test room model is the first one; it is a miniature version of the actual room that will be utilised to run the experiment. A heat source will be placed inside the test room to be used during the experiment. The output generated heat from the heat source will be demonstrated using the second model, which is a heat source model. Alternatively put, the test room model will receive the heat produced by the heat source model. A proof of concept experiment was performed prior to carrying out the experimental examinations for the case in question. By

employing the standard double-glazed window, the Design Builder software was used to create a model of the experimental test room. When the proposed system is deployed, showing the validity of the created model and the setup of the experiment will give a suitable evidence setup for testing the suggested system and verify the validity of energy results of the implemented experiments. It is important to note that the software lacks the features necessary to model the suggested system. But the below information demonstrates the research method that was set up in *Figure 3. 2* and used in this chapter to accomplish the goals: Well-calibrated sensors collect the initial conditions and other input factors from the internal environments of the test models as well as from the external environment. The collected information is shown in *Figure 3. 2* as both indoor and outdoor measurements. For interior conditions, the temperature of the test room is necessary for heat transfer numerical analysis. In addition, the operational status of the heat source and air pump should be recorded in order to calculate energy usage. A data logger can observe the ON intervals for both devices. In order to carry out the modelling of the test room and heat source models by Design Builder software, the weather data outside the test room should be prepared. Temperature, humidity, wind speed, wind direction, and pressure are all aspects of the outside weather. In the sections that follow, a unique tungsten filament calculation procedure has been used to determine the mathematical model of the heat source. The test room model was built using common heat transfer equations. The total thermal efficiency of the suggested ventilated window was evaluated using heat transfer numerical analysis. The mathematical test room model's input data are the heat source's mathematical model and the measurements taken indoors and outdoors. To verify the validity of the system and assess the window's overall thermal performance, the thermal efficiency of the test room model obtained by the numerical analysis and that obtained by the Design Builder software simulation have been contrasted. At last, energy calculations based on the experiment outcomes have been used to confirm the study's goals.

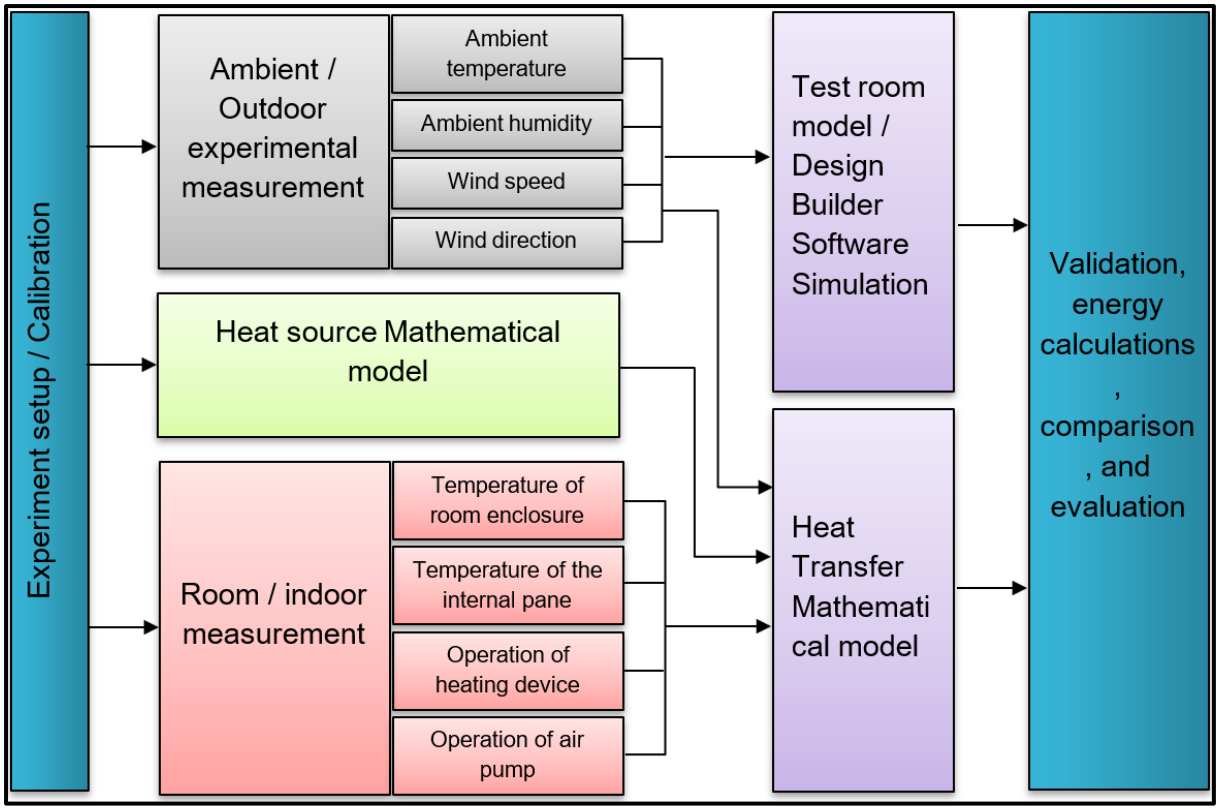

Figure 3. 2. *Workflow and methodology setup.*

3.2.3 Test room

A drawing of the experimental test room and the surrounding environment (atmosphere) is shown in Figure 3. 3 (A). Inside a larger box is the test room; the area between the test room and the outer box symbolizes the atmosphere. As a result, the experiments can be carried out in a controlled setting. A standalone mechanical cooling device will regulate the temperature of the atmosphere space. A cross sectional area for the experimental setup is shown in Figure 3. 3 (B). The air was pumped into the outer box using the mechanical air conditioning system, spread throughout the atmosphere space, and then drained through tiny holes into the exterior environment, maintaining a predetermined temperature. The test room benefits from the outer box's gloomy environment, which makes it easier to study the heat leakage via the window without being affected by solar radiation [143].

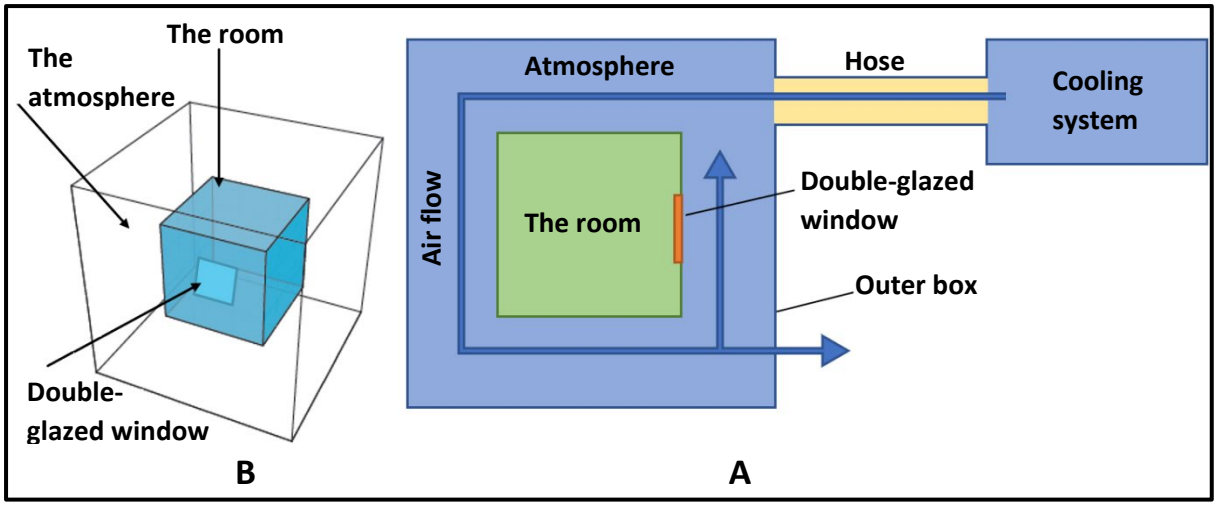

Figure 3. 3. *(A) The test room inside the outer box; (B) Cross-section diagram showing the test room and the outer box with the cooling system.*

The test room and the outer box in **Figure 3. 4** where the experimental setup is depicted, have been constructed from an insulation board. The board is made of double light slices of steel with a thickness of ($0.05\ cm$ each) sandwiching a layer of polystyrene with a thickness of $4.9\ cm$ and a thermal conductivity of $0.046\ W/m.K$. From the outer box to the mechanical cooling system, a metallic hose with a diameter of $7\ inches$ is laid to transmit the cooled air.

In **Figure 3. 4** (A), the front side of the outer box has small holes; these holes allow the cooled air to exhaust after it circulates in the ambient air. **Figure 3. 4** (B) shows the outer box without the front side; the test room with the ventilated double-glazed window is placed inside it. Further, a weather station is hanging on the internal side of the right wall of the outer box; this position will expose it to the proposed atmospheric conditions during the experiment.

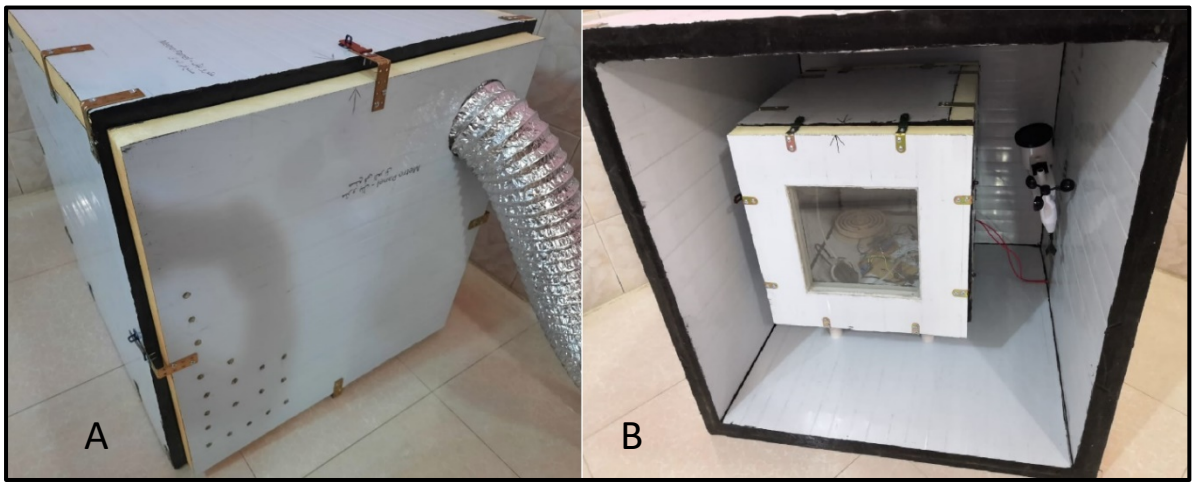

Figure 3. 4. *Setup of the experiment: (A) The outer box; (B) The test room inside the outer box.*

Table 3. 1. *Specifications of the test room and the outer box.*

Component	Parts	values
Board	Thickness of the polystyrene layer	$4.9\ cm$
	Thickness of the steel layer	$0.05\ cm$
Dimensions of the test room's wall		$55\ x\ 55\ cm^2$
Dimensions of the outer box's wall		$100\ x\ 100\ cm^2$
Double glazed window	Length x width of the glazing	$30\ x\ 30\ cm^2$
	Window to wall ratio (WWR)	$44\ \%$
	Glazing type	Clear
	Thickness of a glazing layer	$0.4\ cm$
	Thermal conductance for the glass	$0.9\ W/m.K$
	Distance between glazing panes	$2\ cm$
	Outside reveal depth	$0\ cm$
Dimensions of the test room		$45\ x\ 45\ x\ 45\ cm^3$
Dimensions of the Outer box		$90\ x\ 90\ x\ 90\ cm^3$
Heat source	Input AC voltage	$225\ V$
	Electrical resistance of tungsten filament at 25 °C	$168\ \Omega$
	Mass of the base (the pottery)	$0.53\ kg$
	Heat capacity of the pottery	$0.85\ KJ/kg°C$

The experiments use a typical tungsten-based heater as their heat source. It makes use of a tungsten filament with an electric resistance of $168\ \Omega$ (at standard temperature of $25°C$) that is firmly installed on a mass made of $0.53\ kg$ of pottery with a $0.85\ KJ/$kg°C heat capacity. More information about the design of the test room, the double-glazed window, the outer box, and the heat source is provided in **Table 3. 1**.

3.2.4 Data acquisition system

The outer box and the test room were equipped with a data acquisition system, as shown in **Figure 3. 5**. An Arduino microcontroller (MC) was utilised to manage the operation of data acquisition in the test room. A temperature sensor is connected to the MC to monitor the

temperature inside the room. The heating device and the air-pump were connected to digital output ports on the MC via driver circuits. The function of driver circuits is to sense the digital status of the output digital ports (HIGH or LOW) and drive the heating device and the air pump accordingly.

An SDRAM memory is interfaced with the MC to save the observed data. The MC was programmed to record the ON duration of the heating device and the air-pump in addition to the instantaneous values of indoor temperature with a time step of 10 seconds; then all data should be listed in a text file to be stored in the SDRAM. On the other hand, a weather station was used to measure the weather conditions in the atmosphere space between the outer box and the test room. The weather station has a built-in data logging system to save the observed data. The weather station is designed to measure outdoor temperature, humidity, wind speed, wind direction, and pressure. **Table 3. 2** shows the technical specifications for the utilised microcontroller, temperature sensor, and the weather station.

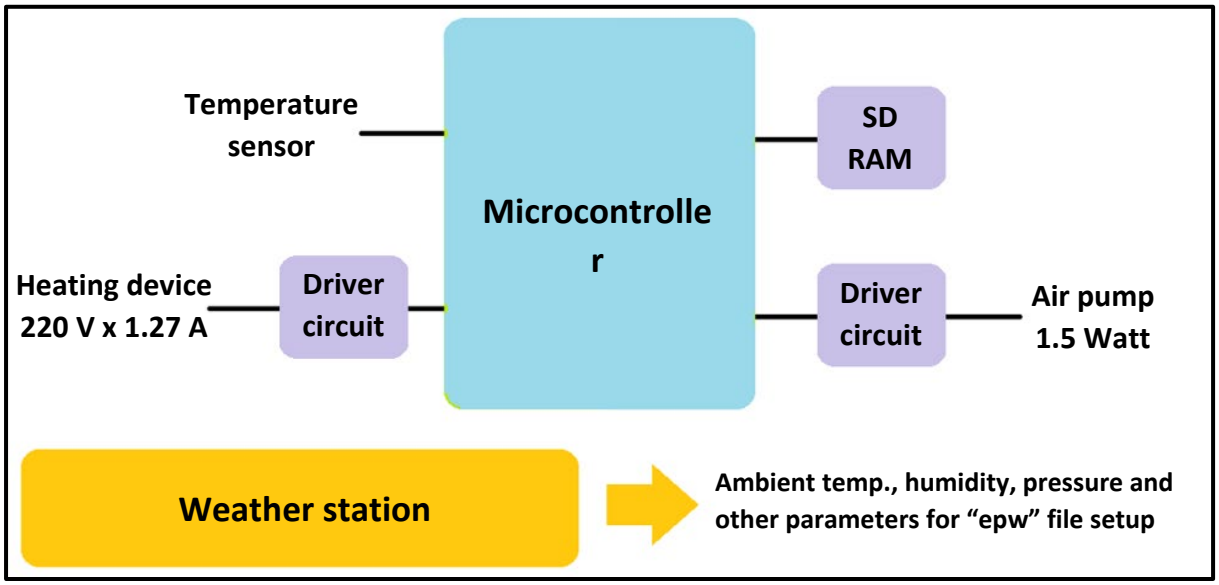

Figure 3. 5. *Data acquisition system for the experimental model.*

Table 3. 2. *Technical specifications.*

Microcontroller		Arduino UNO
DHT22 temperature sensor	Power supply	3.3 - 6 V DC
	Sensing element	Polymer capacitor
	Operation range	humidity 0 - 100 % RH; temperature -40 ~ 80 Celsius
	Precision	humidity +-2 % RH (Max +-5 % RH); temperature < +-0.5 Celsius
	Resolution or sensitivity	humidity 0.1 % RH; temperature 0.1 Celsius
	Sensing period Average	2 sec
WS-8681 MKII weather station	Communication range in open field	100 m (300 feet)
	Frequency	868 MHz (Europe)
	Temperature range	-40 ˚C – 60 ˚C (-40 °F to +140 °F)
	Accuracy	+ / - 1 ˚C
	Resolution	0.1 ˚C
	Measuring range (humidity)	1 % ～ 99 %
	Accuracy	+/- 4 % in range 20 – 80 % RH
	Wind speed	0 - 50 m/s (0 ~ 100 mph)
	Accuracy	+/- 1 m/s (wind speed < 5 m/s) +/- 10 % (wind speed > 5 m/s)
	Measuring interval thermo-hygro sensor	48 sec

3.2.5 Test room model

A heat source is used to provide space heating in the experimental test room. Different components inside the room, which serve as thermal loads, should receive the heat produced. For example, a portion of the heat produced heats the interior environment and the pottery, whereas the remainder is absorbed by the walls and window glazing. The equations presented in this section, however, are those that Ghosh et al. suggested [144]. However, the equations have been amended to take into account the heat that the pottery absorbs in accordance with the specified heat system. The subscript "1" is adopted here for particular acronyms to prevent repetition in the following sections.

$$Q_{Tungsten} = Q_{pot1} + Q_g + Q_{room1} + Q_{w1} \quad (3.\ 1)$$

Where:

- $Q_{Tungsten}$: heat produced by the tungsten filament (W).

- Q_{pot1}: heat absorbed by the pottery (W).
- Q_g: heat leakage via the glass (W).
- Q_{room1}: heat absorbed by the environment of the room (W), it is calculated as following:

$$Q_{room1} = M_{room1} C_{air} \frac{dT_{in}}{dt} \quad (3.\ 2)$$

- M_{room1}: the amount of air inside the room (kg) $= \rho_{air} V_{room1}$.
- ρ_{air}: density of the air = 1.2250 kg/m3.
- V_{room1}: the size of the test room.
- C_{air}: heat capacity of the air = 1.006 kJ/kg°C.
- T_{in}: temperature of the interior environment of the room in °C.
- Q_{w1}: heat transfer due to interior and exterior air convection and conduction via the insulation board wall:

$$Q_{w1} = U_{w1} A_{w1} (T_{in} - T_o) \quad (3.\ 3)$$

- U_{w1}: combined heat transfer coefficient of the test enclosure's wall with interior and exterior air in (W/m^2K).

$$U_{w1} = [\frac{1}{h_o} + \frac{L}{K} + \frac{1}{h_i}]^{-1} \quad (3.\ 4)$$

Where:

- h_o: exterior convection heat transfer coefficients in (W/m^2K):
- $h_o = 5.7 + 8.8V_{wind}$, V_{wind}: the wind speed in m/s.
- h_i: inside convection heat transfer coefficients in (W/m^2K):
- $h_i = 7\ (W/m^2K)$.
- L: thickness of the insulation board in meter.
- K: thermal conductance of the insulation board in $W/m.K$.
- A_w: area of the insulation board in m^2.
- T_o: temperature of the atmosphere in °C.

Equation (3. 5) gives the glazing's heat transfer coefficient, or the U-value (U_g), after equation (3. 1) has been solved to determine the value of (Q_g):

$$U_g = \frac{Q_g}{A(T_{in} - T_0)} \quad (3.\ 5)$$

The tungsten wire stops producing heat during the cooling interval. Since the pottery began to release heat into the room as soon as it had absorbed the majority of the heat during the heating phase, equation (3. 1) can be modified as follows to account for cooling conditions:

$$Q_{pot1} = Q_g + Q_{room1} + Q_{w1} \quad (3.\ 6)$$

It is now essential to identify the mathematical model of the heat source, including the tungsten filament and the pottery, in order to calculate the actual heat input to the test room in the heating and cooling phases. In order to satisfy this demand, a new test room will be built in the following section.

3.2.6 Heat source model

Finding the mathematical representation of the heat source, including the tungsten filament and the pottery, is essential to calculating the actual heat input power to the test room in the heating and cooling phases. An additional experimentation model was developed. The tungsten-based heat source is housed inside a tiny box with the dimensions (0.245 * 0.175 * 0.375 m^3). The box's walls are made of the same insulation board that was used to build the test room. To make calculations simple, the box was built without windows to prevent heat loss in the glazing. Moreover, the main purpose of the new model is to calculate the heat source generation.

After disregarding the heat loss in the glazing, the formulas of the heat transfer model can be used to describe the heat source model, so:

$$Q_{Tungsten} = Q_{pot2} + Q_{room2} + Q_{w2} \quad (3.\ 7)$$

Where:

- $Q_{Tungsten}$: heat produced by the tungsten filament (W).
- Q_{pot2}: heat dissipation in the pottery (W):

$$Q_{pot2} = M_{pot} C_{pot} \frac{dT_{pot}}{dt} \quad (3.8)$$

Where:

- M_{pot}: mass of the pottery = 0.53 kg.
- C_{pot}: heat capacity of the pottery = 0.85 kJ/kg°C.
- T_{pot}: temperature of the pottery.
- Q_{room2}: heat stored inside the heat source model (W); it can be determined using equation (3. 2) based on the given data of the internal environment of the test box.
- Q_{w2}: heat transfer due to interior and exterior air convection and conduction via the insulated board wall, it can be estimated using equation (3. 3) according to the given data of the test box.

Equation (3. 7) can be changed to fit the cool conditions as follows: throughout the cool phase, the tungsten filament receives no electrical power, and the heat preserved in the pottery begins to transfer to the room as it absorbs a large percent of the heat source generation throughout the warming phase.

$$Q_{pot2} = Q_{room2} + Q_{w2} \quad (3.9)$$

The pattern of heat generation from the heat source will be determined and verified before carrying out the experiment on the test box. In order to operate the heat source inside the test box and monitor the temperature of the pottery-base, the probe of a K-type thermocouple was directly attached to the pottery's body. In addition, two temperature sensors were positioned inside and outside the test box to measure the temperature inside and outside the room, respectively. An Arduino microcontroller manages the operation of the calibrated sensors, as shown in Figure 3. 6. The SDRAM memory was necessary to store the measured data during the experiment.

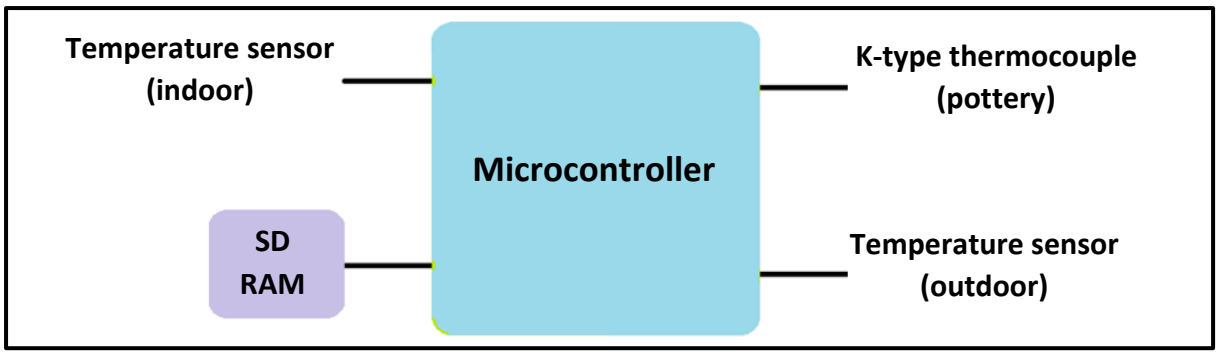

Figure 3. 6. *data acquisition system for heat source modelling experiment.*

Figure 3. 7 shows the source's heat production after resolving equation (3. 7). Once the electrical source is powered up, the amount of heat supplied increases and requires about $200\ seconds$ to reach the steady state. In addition, the mean value of the supplied heat in the steady state is approximately $117.32\ watts$ over the course of $200\ to\ 600\ seconds$.

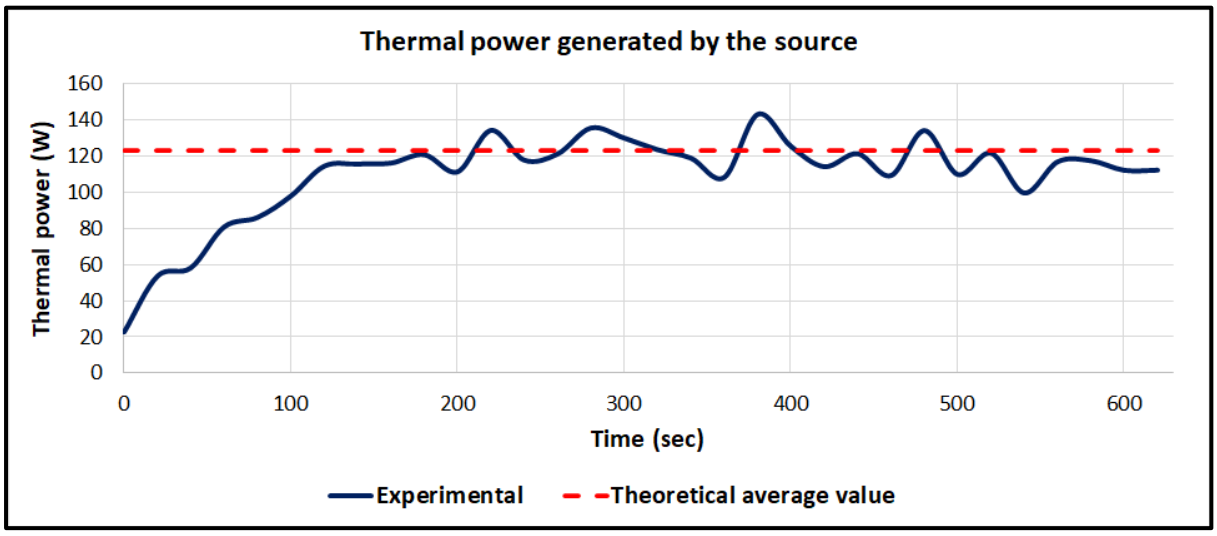

Figure 3. 7. *Heat production of the tungsten filament heat source.*

According to equations (3. 10) and (3. 11), Agrawal [145] calculated the generated steady state heat P by the tungsten filament:

$$R = R_o \left({}^{T_s}/_{T_o}\right)^x \tag{3.10}$$

$$P = \frac{v^2}{R_o \left({}^{T_s}/_{T_o}\right)^x} \tag{3.11}$$

Where:

- R: electrical resistance of the tungsten filament at the steady-state temperature.
- R_o: electrical resistance of the tungsten filament at the initial temperature, for the implemented experiments, $25\ °C$ and $R_o = 168\ \Omega$.

- T_o: initial temperature of the tungsten filament in Kelvin, for the implemented experiments, 25 °C or 298 K.
- T_s: steady-state temperature of the tungsten filament in Kelvin, T_s has been determined experimentally by a K-type thermometer; it was 306 °C or 579 K.
- v: root-mean-square value of the input ac voltage $= 225\ volts$.
- The parameter (x) is estimated to maintain the ratio ($^{R}/_{R_o}$) equals to the ratio ($^{T_s}/_{T_o})^{x}$ according to the equation (3. 10). The ratio of $^{R}/_{R_o}$ is determined from the table of electrical resistance of tungsten filament on [146], in the range of ($298\ to\ 579\ K$). However, based on the case under consideration, the most appropriate match for the parameter x is 1.31.

By resolving equations (3. 10) and (3. 11), it can be seen in Figure 3. 7 that the source generates $123.46\ watts$ of steady state heat. The difference between the mathematical and experimental steady state values of the supplied heat, $123.46\ vs.\ 117.32\ watts$, respectively, is acceptable. Further, it could be the result of omitting the heat absorption by some components in the box, such as electrical wires and thermocouple wires. For purposes of further consideration, it is therefore feasible to assume that the experimental model of the heat source is accurate.

3.2.7 Simulation and validation of the experimental model

To confirm the validity of the experimental test room, a different experiment has been carried out. The test room was subjected to the atmospheric temperature values represented by the curve depicted in Figure 3. 8; the heat source was turned off. The weather station collected the weather data on the outdoor environment, including temperature, humidity, pressure, and wind speed and direction, while the heat sensor captured the temperature of the room's enclosure.

As opposed to that, the test room model has been created using the Design Builder software according to the specifications listed in Table 3. 1. Additionally, the weather data file, which is necessary for the simulation, has been organized to reflect the experimental circumstances, including the information gathered from the weather station. As the experiment was

conducted in a gloomy environment (according to the experimental setup, the test room inside the outer box), solar irradiation and illumination data were ignored.

As shown in Figure 3. 8, the temperature of the test room's enclosure was determined throughout the experiment and through the simulation. The outcome demonstrates how the simulated and experimental temperature of the test room's enclosure react to changes in atmospheric conditions. Additionally, there is a $0.2°C$ difference on average between the simulated and experimental room temperatures. As a result, it is reasonable to presume that the experimental test room model will be taken further into account when the suggested ventilation system is implemented.

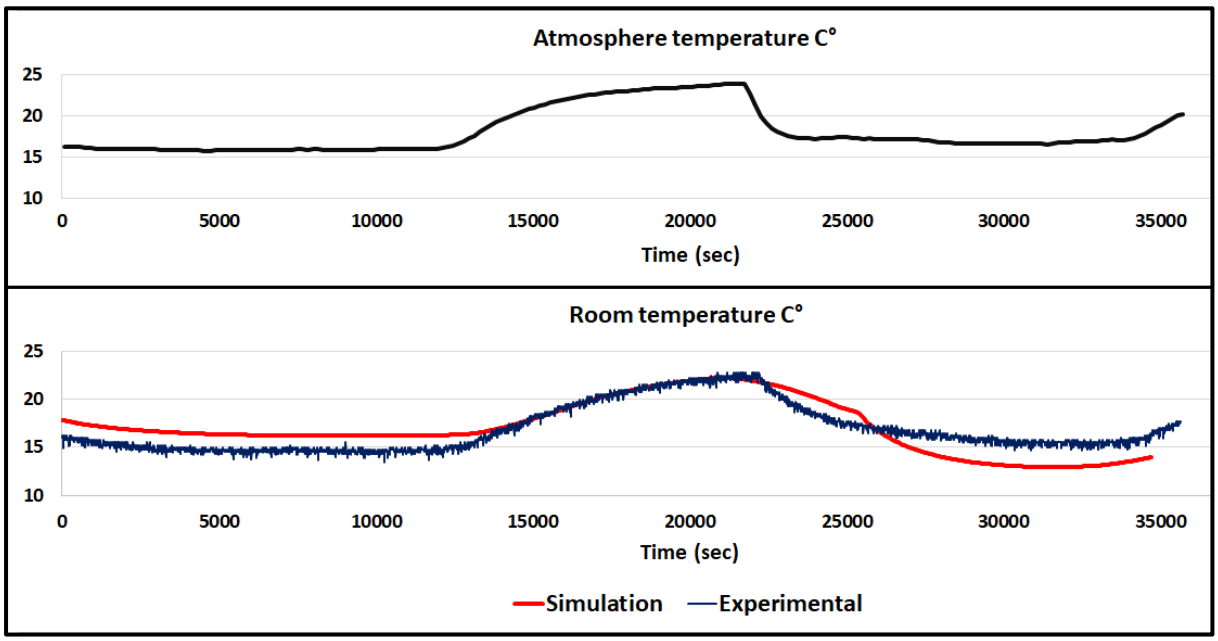

Figure 3. 8. *The experimental and simulated temperature of the test room.*

3.2.8 Experiment scenarios

The scenarios demonstrated in **Table 3. 3** have been carried out in the experimental test room, and a data logger and an embedded control system were developed. In all cases, it is proposed that the velocity of waste air be $2000\ cc/min$, based on the technical specifications of the utilised air pump. The suggested ventilated double-glazed window will be supplied with the waste air. The main challenge in each scenario is to use the least amount of the obtainable waste air; the remainder can then be used for other windows. As a result, more heat loss that

is caused by windows can be minimized, and total energy savings will be maximized accordingly. The use of waste air per single ventilated window will be carried out according to the following proposed techniques:

i. As the air pump was turned off in the first scenario, the window operated according to the standard double-glazed approach. Other scenarios will be referred to this case.

ii. In scenario $2, 3, and\ 4$, the air pump operates in a duty-cycle of 50% as follow:
    a. Based on the provided dimensions of the suggested double-glazed ventilated window and the highest obtainable velocity of the waste air ($2000\ cc/min$), the air pump should operate for $54\ seconds$ in order to drain out the air in the gap between the panes of the window and substitute it with the waste air. Thus, through one operating cycle, the air pump ran for $54\ seconds$, then powered off for $54\ seconds$ periodically. In other words, the frequency of on-off air pump operation was ($1/108\ Hz$) in scenario 2.
    b. The frequency of on-off air pump operation was raised to ($1/20\ Hz$) and ($1/10\ Hz$) in scenarios 3 and 4, respectively.

iii. The air pump operates continually, i.e., with duty-cycle of 100%, with various air velocities. For the fifth through eighth scenarios, the waste air flow rate was changed to $2000\ cc/min, 1000\ cc/min, 666\ cc/min, and\ 500\ cc/min$, respectively.

Throughout every scenario, the test room will transition between two thermal transfer conditions: heating and cooling. The heating phase begins at a room temperature of $22°C$. The final temperature during the heating phase is to heat up the room to $27°C$ before turning off the heat source. The test room will be subjected to the atmospheric circumstances during the cooling phase. The cooling duration is the amount of time needed for the room's temperature to drop to $22°C$.

The outcomes of the experimental scenarios will be illustrated in the following subsections, along with an analysis of the effects of (1) the air pump's duty-cycle and on-off operation frequency and (2) the velocity of the waste air on the window's thermal efficiency.

Table 3. 3. *Scenarios of the experiment on the test room.*

No.	Air velocity (cc/min)	Pump duty cycle	Pump on/off frequency (Hz)	Initial room temperature (°C)	Target room temperature (°C)	Final room temperature (°C)
1	0	0 %	0	22	27	22
2	2000	50 %	1 / 108			
3	2000	50 %	1 / 20			
4	2000	50 %	1 / 10			
5	2000	100 %	0			
6	1000	100 %	0			
7	666	100 %	0			
8	500	100 %	0			

3.3 Results and discussion

The test room inside the outer box has been used to conduct the experimental scenarios shown in Table 3. 3. To keep track of the weather, the weather station was installed in the atmospheric area between the two boxes, as described earlier. The temperature sensor has also recorded the test room's temperature every $10\ seconds$. In all cases, the temperature of the waste air was $24.5°C$.

The temperature of the test room's enclosure is shown in Figure 3. 9 with the air pump turned off. In this case, the window performs the same function as a typical double-glazed window. While conducting the energy calculations, the outcomes from other scenarios will be referred to this case. As shown in the figure, it took $100\ seconds$ of continuous running of the heat source throughout the heating time to raise the room temperature from $22°C\ to\ 27°C$. Following $3390\ seconds$ of the cooling phase, the room's temperature dropped to $22°C$ once more.

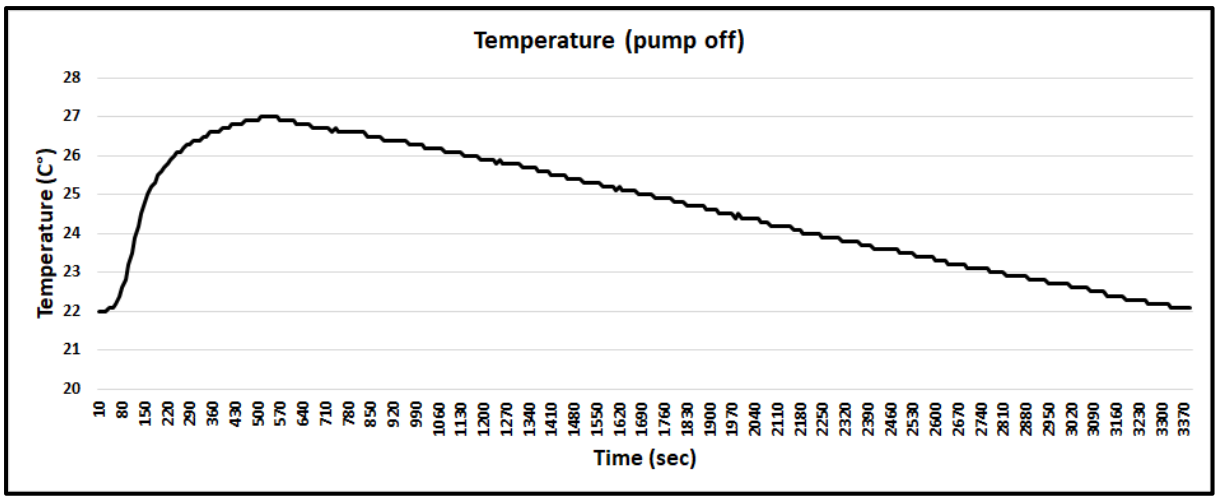

Figure 3. 9. *Temperature of the test room in scenario 1.*

For scenario $2, 3, and\ 4$, test temperature is shown in Figure 3. 10. The window operates under forced ventilation conditions and functions as a double-glazed ventilated window. Throughout the heating time of the mentioned scenarios, the heat source needed $100\ seconds$ to run in order to increase the room's temperature from $22°C\ to\ 27°C$. However, after $4690, 4830, and\ 4870\ seconds$, the room's temperature dropped to $22°C$ once more throughout the cooling period in the scenarios $2, 3, and\ 4$, respectively.

The temperature of the room's enclosure for scenarios $5, 6, 7, and\ 8$ is shown in Figure 3. 11. The window operates under forced ventilation conditions and functions as a double-glazed ventilated window. Following $100\ seconds$ of operating the heat source throughout the heating duration, the room's temperature rose from $22°C\ to\ 27°C$. On the other hand, the room temperature declined to $22°C$ once more throughout the cooling period after $7230, 6420, 5120, and\ 4050\ seconds$ in the mentioned scenarios, respectively.

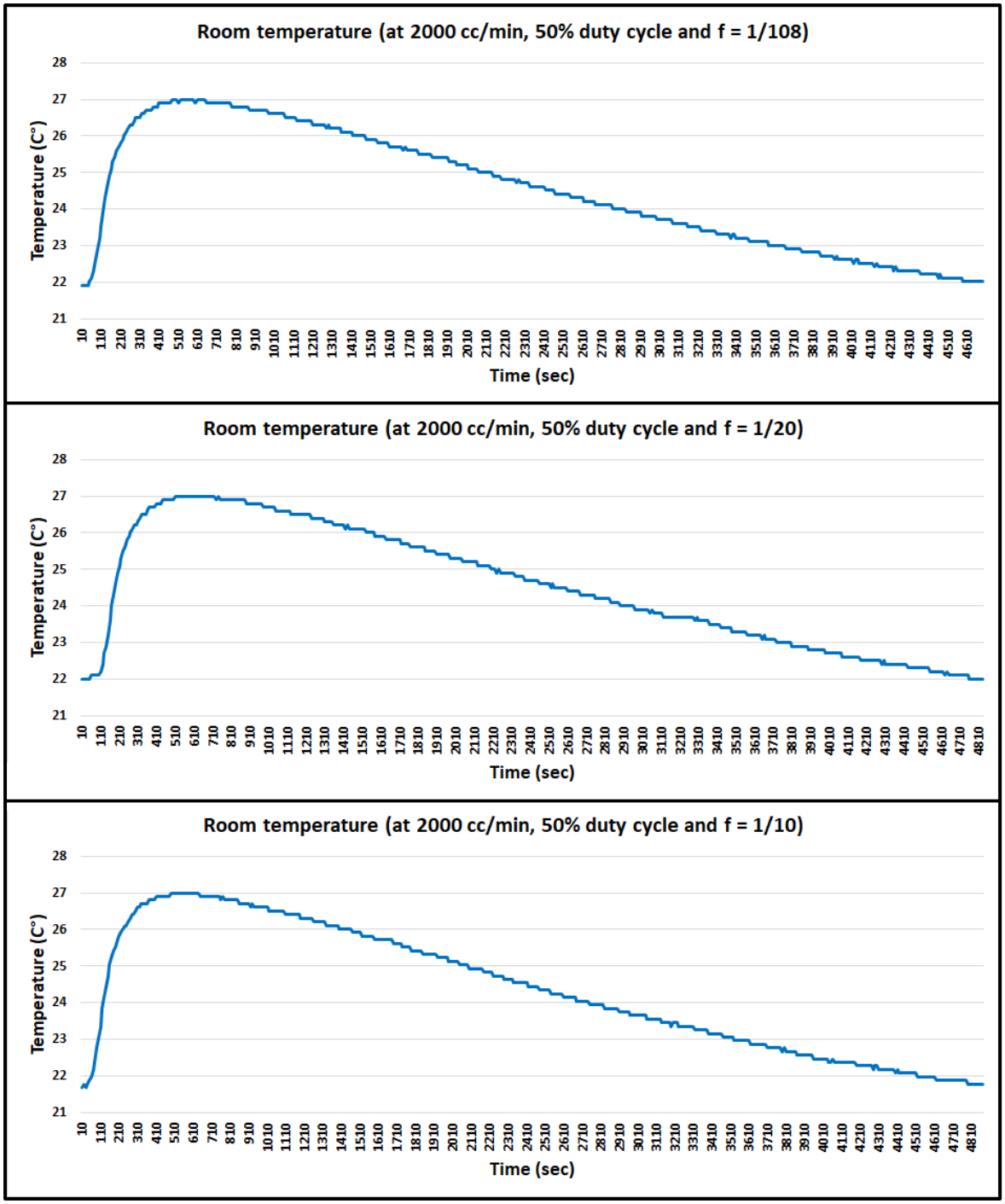

Figure 3. 10. *The temperature of the test room in scenarios* $2, 3,$ *and* $4.$

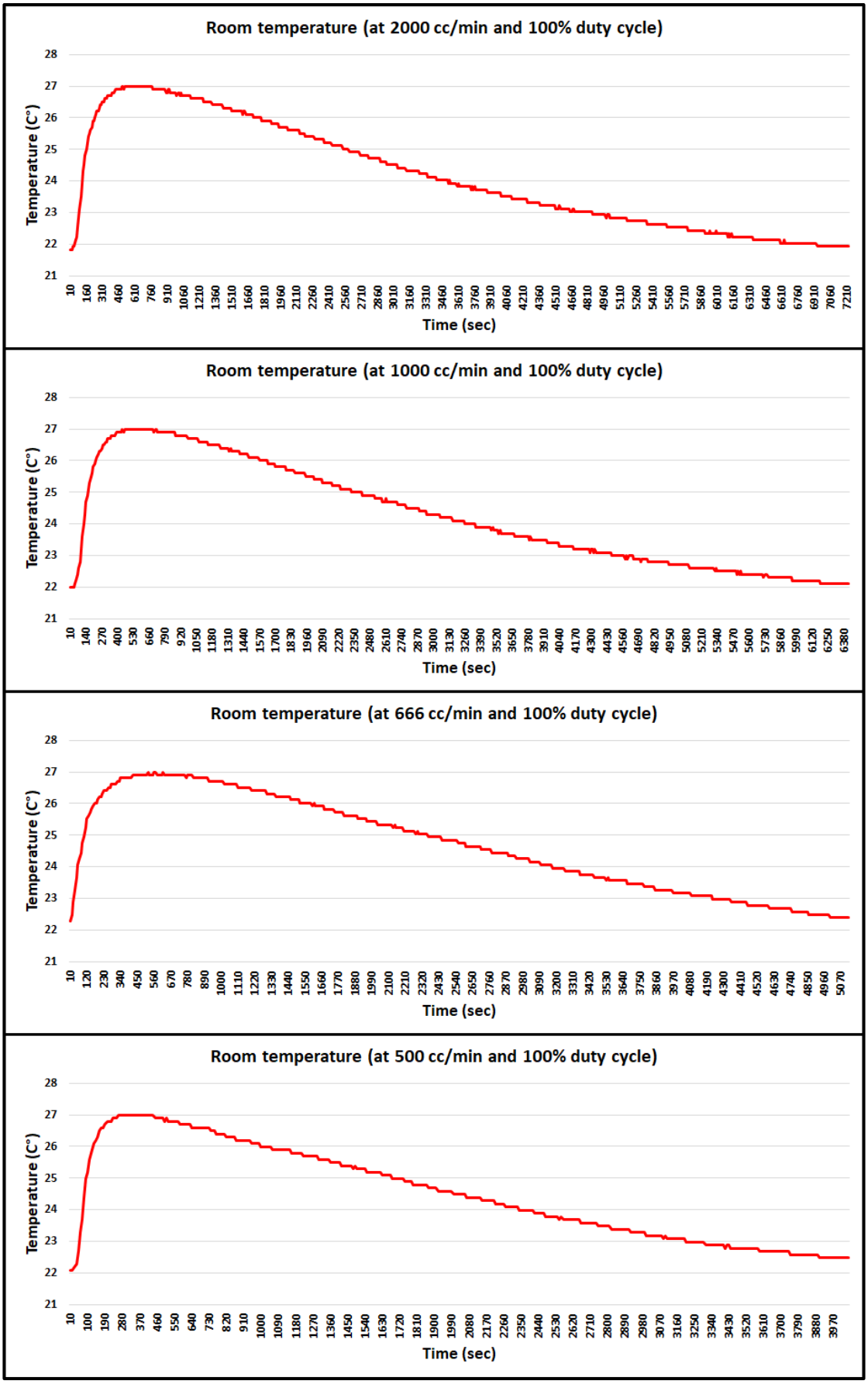

Figure 3. 11. *The temperature of the test room in scenarios* 5, 6, 7, *and* 8.

Starting with a temperature of $22°C$, a highest targeted temperature of $27°C$, and ending with a temperature of $22°C$, the test room's temperature always falls within the same range in all scenarios. However, because each scenario's circumstances for heat transfer were unique, the cooling duration varied between scenarios.

Due to the fact that different scenarios' heating and cooling times were not identical, each experiment's input heat power was different because the source needed $200\ seconds$ to approach its steady-state response. Alternatively, during the heating phase, further operation of the heat source causes higher heat generation. In contrast, during the cooling phase, further cooling time leads to lower supplied power. The average heat transmitted from the source to the test room will be calculated for every scenario throughout the heating and cooling periods in the steps that follow. The total heat transmitted from the heat source to the room is essential to estimating the heat loss in the glazing.

The test room's heating and cooling times revealed by the experiments are listed in Table 3. 4. Heating times in all scenarios are almost equal because the start and end room temperatures are the same during the heating phase of the experiment. In order to avert producing duplicate outcomes, the mean value of the heating periods ($594\ seconds$) will be taken into account in the calculations that follow.

Table 3. 4. *Times of heating and cooling phases.*

Scenario	1	2	3	4	5	6	7	8
Heating interval (seconds)	560	600	605	610	610	600	610	560
Cooling interval (seconds)	2830	4090	4225	4260	6620	5820	4510	3490

Throughout the heating phase, turning to equations (3. 1) and (3. 7), the dissipated power in the pottery in the test room and in the heat source box is equivalent ($Q_{pot1} = Q_{pot2}$), as the amount of heat absorbed by the pottery is equal in each case; therefore, the heat generated by the source can be defined as follows:

$$Heat\ supplied\ to\ the\ test\ room\ during\ heating\ period = Q_{Tungsten} - Q_{pot2} = Q_{room2} + Q_{w2} \quad (3.\ 12)$$

Furthermore, turning to equations (3. 6) and (3. 9) that define the cooling phase, the dissipated power by the pottery in the test room and in the heat source box is not equated ($Q_{pot1} \neq Q_{pot2}$), as the temperature variance between the pottery and the room is not equivalent in the two experiments.

To conquer this obstruction, the variance in the dissipated power in the pottery ΔQ_{pot} may be determined in terms of the mean temperature differences ($T_{pot1av} - T_{room1av} = 44 - 24.5 = 19.5°C$) and ($T_{pot2av} - T_{room2av} = 44 - 28.6 = 15.4°C$), therefore, $\Delta T_{1,2} = 19.5 - 15.4 = 4.1°C$ is the temperature variance that creates the difference between Q_{pot1} and Q_{pot2}, in which T_{pot1av} and $T_{room1av}$ are the mean temperatures of the pottery and the room in the test room, while T_{pot2av} and $T_{room2av}$ are the mean temperatures of the pottery and the room in the heat source box. Therefore:

$$\Delta Q_{pot} = Q_{pot1} - Q_{pot2} = M_{pot} C_{pot} \frac{d(\Delta T_{1,2})}{dt} \quad (3.\ 13)$$

Thus, the heat provided to the test room throughout the cooling phase is:

$$Heat\ supplied\ to\ the\ test\ room\ during\ cooling\ period = Q_{pot1} = Q_{room2} + Q_{w2} + \Delta Q_{pot} \quad (3.\ 14)$$

The heat source was activated for $100\ seconds$ in each experiment to jump to the desired temperature ($27°C$). Further, scenario 5 needed the highest delay ($7230\ sec$) to bring the test room temperature down to ($22°C$). In order to estimate the mean heat provided to the room throughout heating and cooling phases in various scenarios, a different experiment has been carried out. The temperature of the room, the pottery, and the exterior environment were recorded over a period of $7230\ seconds$ following the activation of the heat source inside the box for $100\ seconds$. Using the collected information, the equations (3. 12) and $(3.\ 14)$ have been solved. As a result, Table 3. 5 shows an estimate of the heat provided to the test room throughout the heating and cooling phases.

Table 3. 5. *Input heat throughout heating and cooling phases.*

Scenario	Mean time heating phase	Average heat power	Cooling intervals (seconds)	Mean heat power (Watts)
1	594 *seconds*	6 *watts*	2830	5.1
2			4040	4.68
3			4090	4.43
4			4230	4.32
5			6460	4.36
6			5700	4.25
7			4500	4.51
8			3610	4.86

Back to equations (3. 5), it has been calculated how much heat is lost through the window (Q_g) and how much heat is transferred (U_g) during the experiments. Figure 3. 12, Figure 3. 13, and Figure 3. 14 explain the heat transfer coefficient and heat loss in the window in the scenarios that were put into practice. It is noted that glazing U-value and heat loss change in the same manner as room temperature because the atmospheric temperature is set to $17°C$ permanently and only room temperature is changed throughout the experiments. Alternately, they react in accordance with the temperature variance between the room and the atmosphere based on equation (3. 5). The mean values will be taken into account when examining the glazing's thermal performance under various conditions.

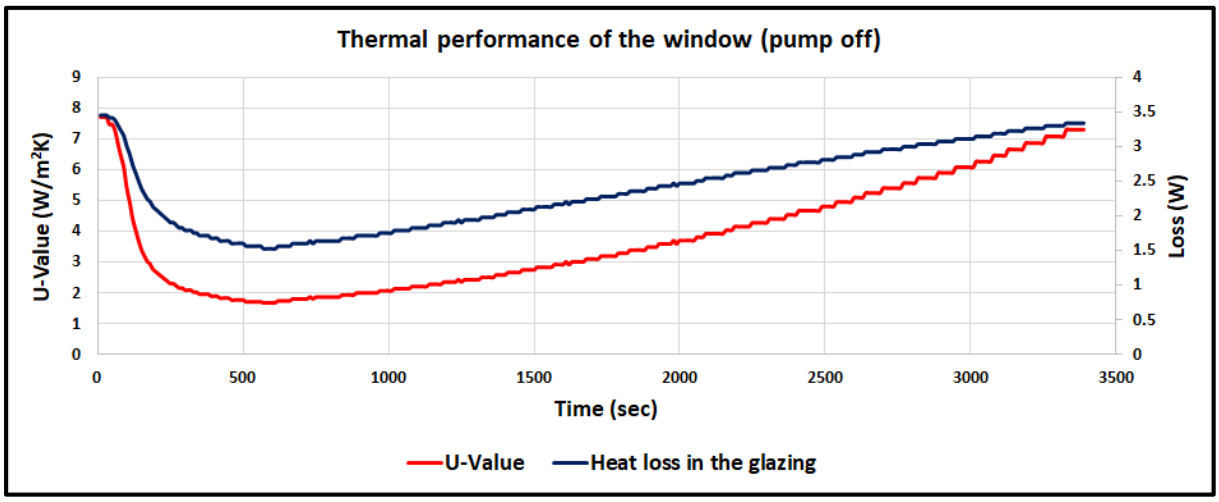

Figure 3. 12. *Glazing heat transfer coefficient and heat loss in scenario 1.*

Figure 3. 12 illustrates the typical double-glazed window's thermal efficiency. As the temperature variance between the room and the atmosphere increased, heat loss and the heat transfer coefficient of the glazing dropped, displaying an improvement in thermal performance throughout the heating phase. On the other hand, as the room temperature dropped throughout the cooling phase, thermal performance declined. However, the U-value's lowest and highest noted values are $1.7\ W/m^2K\ and\ 7.69\ W/m^2K$, respectively, while the glazing loss's lowest and highest noted values are $1.52\ W\ and\ 3.46\ W$, respectively.

The thermal efficiency reacts to the temperature variance in a similar way for scenarios 2 through 8, as shown in Figure 3. 13 and Figure 3. 14. The U-value of the glazing ranged from $3.24\ to\ 2.86\ to\ 2.89\ to\ 3.06\ to\ 2.46\ to\ 2.36\ to\ 3\ W/m^2K$ on average, respectively. These values, however, show divergent efficiency in the experiments. After the estimations for energy consumption are accomplished, the relationship between thermal efficiency and the system's inputs in various experiments will be examined in the sections that follow.

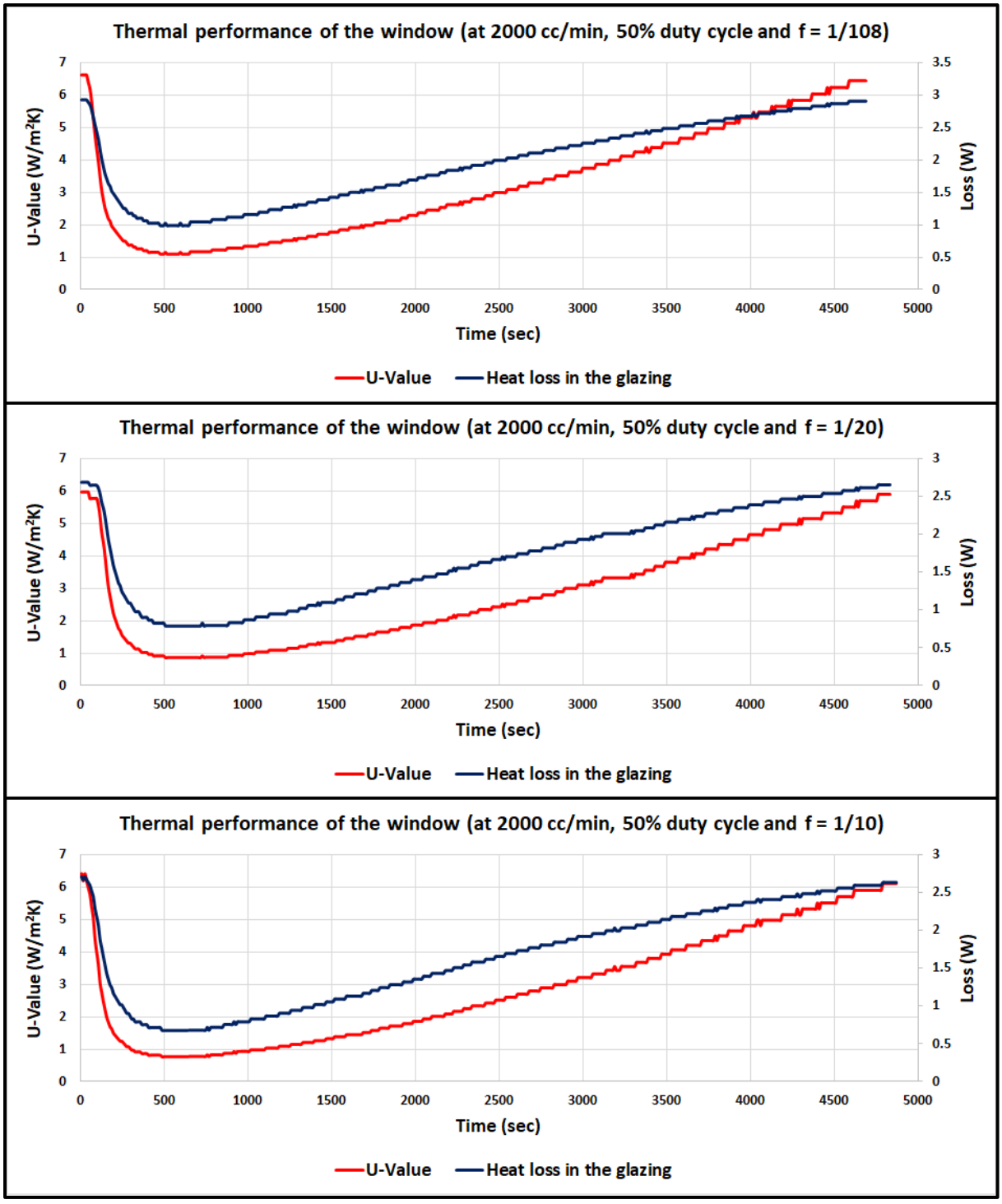

Figure 3. 13. *Glazing heat transfer coefficient and heat loss in scenarios* $2, 3,$ *and* $4.$

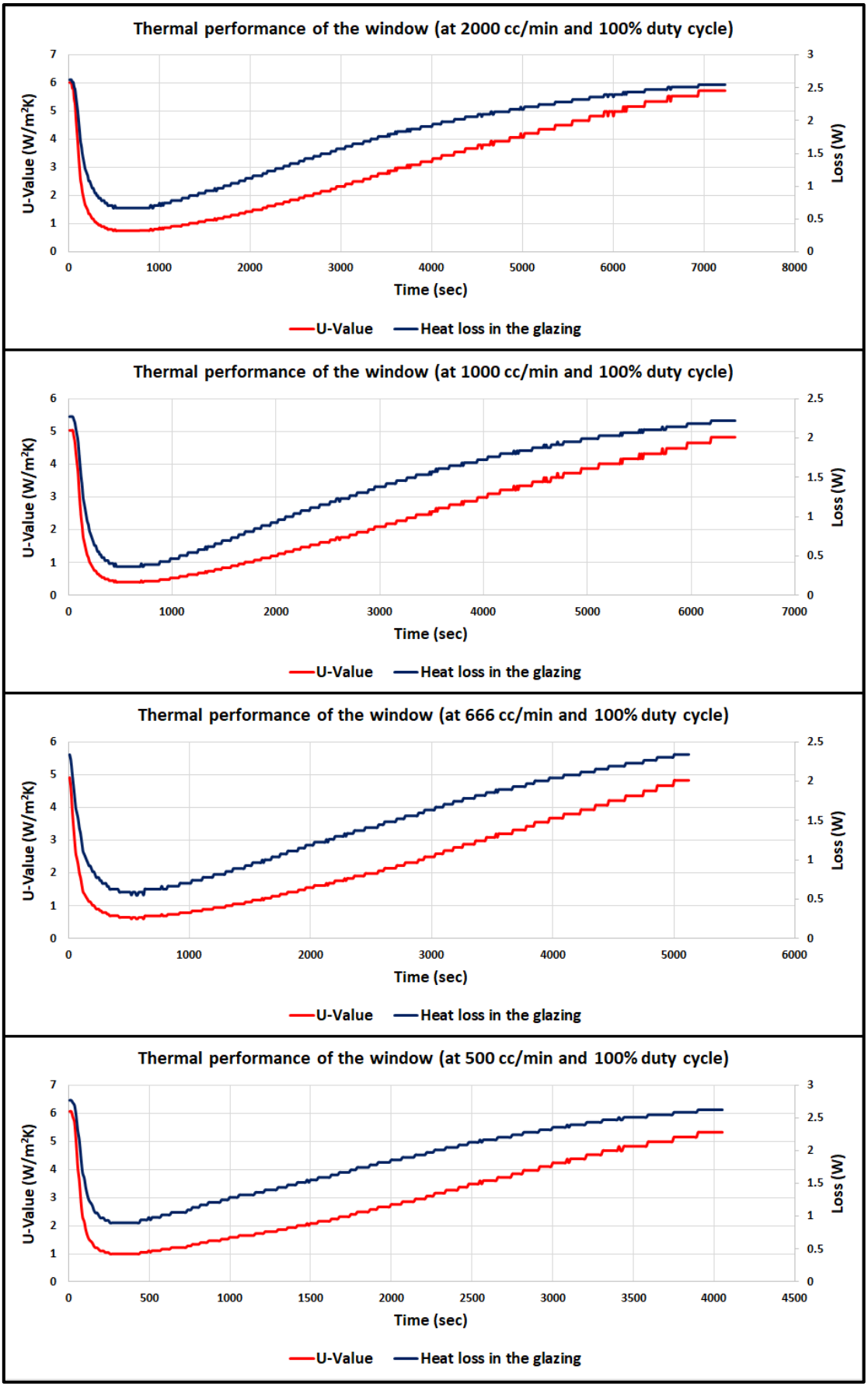

Figure 3. 14. *Glazing heat transfer coefficient and heat loss in scenarios* 5, 6, 7, *and* 8.

The experiment's energy computations are shown in Table 3. 6. Input energy consumption of the heat source was the same across all scenarios because the heat source's operating time was constant ($100\ seconds$). With the exception of scenario 1, where the air pump consumed no energy as it was off, the pump's energy use is calculated as the product of its input ($1.5\ W$) and the related experiment time. The energy used for the heat source and the pump determines the overall energy usage.

Table 3. 6. *Energy calculations.*

Scenario	Air-pump operation			Experiment duration (sec)	Heating consumption (W.sec)	Pump consumption (W.sec)	Total consumption (W.sec)
	Flow (cc/min)	Duty cycle %	Frequency (Hz)				
1	0	0	0	3390	27940	0	27940
2	2000	50	1 / 108	4690		3517.5	31457.5
3	2000	50	1 / 20	4830		3622.5	31562.5
4	2000	50	1 / 10	4870		3652.5	31592.5
5	2000	100	0	7230		10845	38785
6	1000	100	0	6420		4815	32755
7	666	100	0	5120		2560	30500
8	500	100	0	4050		2025	29965

Table 3. 7 also illustrates the experiment's computations for energy conservation. As was already mentioned, various scenarios have different experimental periods. Consequently, energy usage in various cases should be compared to the first scenario (typical double-glazed window) in accordance with the time in order to determine energy conservation in different cases. The experiment time, for example, is $1.38\ times$ greater in scenario 2 than it is in the first case. In comparison to the reference scenario, the second scenario's energy usage is ($31457.5 / 1.38 = 22737.9\ W.sec$). Alternately, whenever the test room runs under the circumstances of the second scenario for $3390\ seconds$ (the experiment time of the first case), energy usage will be $22737.9\ W.sec$. In the same manner, energy conservation was calculated for the remaining scenarios, as illustrated in the table.

Table 3. 7. *Computations of energy conservations.*

Scenario	Energy usage w.r.t. 1st scenario (W.sec)	Energy conservation (W.sec)	Energy conservation per one window (%)	Number of windows shared the attainable velocity	Total energy conservation w.r.t. 1st scenario (%)
1	27940	- - - - - - -	- - - - - - -	- - - - - - -	- - - - - - -
2	22737.9	5202.1	18.62	2	37.24
3	22152.6	5787.4	20.7	2	41.4
4	21991.5	5948.5	21.3	2	42.6
5	18185.5	9754.5	34.9	1	34.9
6	17295.9	10644.1	38.1	2	76.2
7	20194.3	7745.7	27.7	3	83.1
8	25081.8	2858.2	10.2	4	40.8

Additionally, the carried out scenarios have been compared to scenario 1 to estimate the energy conservation in a single window. In scenario 6, the greatest energy conservation of 38.1% was attained when air velocity was $1000\ cc/min$. However, in some cases, as depicted in the table, the window used some of the attainable waste air. In this situation, it can be presumed that additional windows in the building can receive the leftover air at the same time to further reduce energy use. As a result, the following scenarios can demonstrate total energy conservation:

1. The air pump operates at 50% duty cycle in scenarios $2, 3, and\ 4$, so the velocity of waste air is sufficient to supply two windows, doubling the total energy conservation.
2. In the fifth experiment, a single window was ventilated by the available waste air, so the total energy conservation remained at 34.9%.
3. Two windows can be fed by the attainable waste air resource in the sixth experiment since the velocity of the utilised waste air was only $1000\ cc/min$. As a result, total energy conservation will increase by twofold.

4. By using an air velocity of $666\ cc/min$ for the window in the seventh scenario, $2000\ cc/min$ is sufficient to supply three windows. Total energy conservation will triple accordingly.
5. In the eighth scenario, the air velocity was $500\ cc/min$, which was sufficient to provide enough supply for four windows. As a result, the energy savings across all four windows will be four times higher.

The experiment aimed to optimize energy conservation by controlling the waste air through two different methods. The first method involved setting the pump duty cycle to $50\ \%$ in scenarios $2, 3, and\ 4$. The pump was turned on and off at various intervals within its duty cycle. The thermal efficiency of the ventilated window under this on/off interval control is illustrated in Figure 3. 15, and further information are provided in the below three situations:

1. When the air pump operated for $54\ seconds$ within one duty cycle, the heat transfer coefficient of the glazing decreased from $3.82\ to\ 3.24\ W/m^2K$, leading to an energy conservation of 37.24% in comparison with a standard double-glazed window. However, it was observed during the experiment that switching off the pump for $54\ seconds$ within one duty cycle could result in significant heat leakage via the window. Therefore, it was decided to lower the on/off intervals for the air pump within each duty cycle in subsequent steps.
2. By adjusting the on/off durations of the air pump to $10\ seconds$ per duty cycle, the system demonstrated a significant enhancement in its heat transfer coefficient, which decreased to $2.86\ W/m^2K$. This modification also led to an energy conservation of $41.4\ \%$.
3. By adjusting the on/off durations of the air pump to $5\ seconds$ per duty cycle, the thermal efficiency of the system reached a point of saturation, achieving an energy conservation of 42.6% and a heat transfer coefficient of $2.8\ W/m^2K$. This was the best efficiency achieved by on/off duration control. Further reduction of the on/off intervals was not possible as it was not feasible to turn the pump on and off within less than $5\ seconds$.

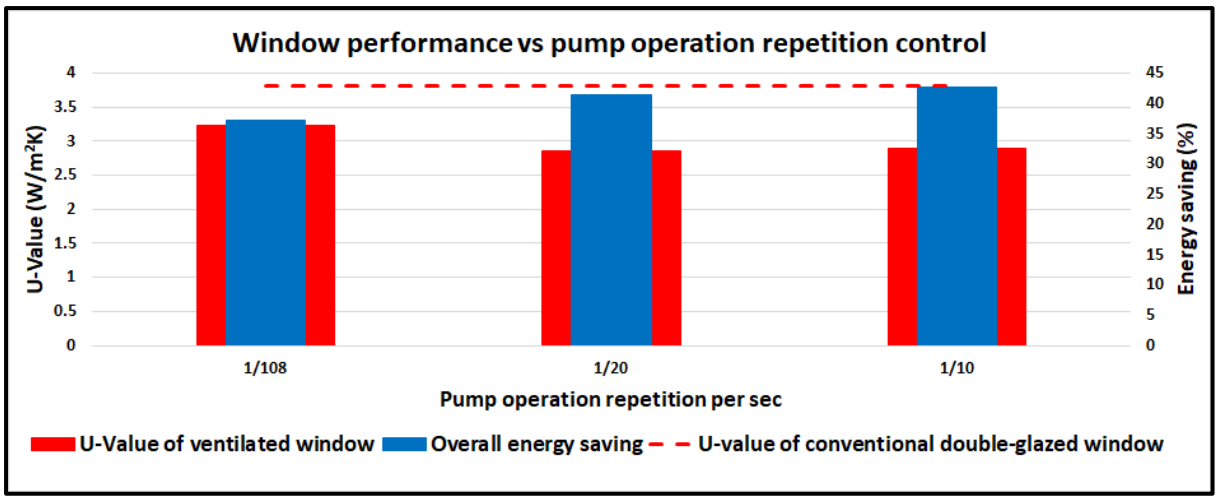

Figure 3. 15. *Thermal efficiency of the ventilated window using on/off duration control.*

The second method used in the experiment involved setting the air pump duty cycle to 100% in scenarios $5, 6, 7, and\ 8$, while adjusting the air velocity supplied to the window. The thermal efficiency of the glazing under this flow rate control is illustrated in Figure 3. 16, and further details are provided in the below four situations:

1. When the air velocity was adjusted to $2000\ cc/min$, the heat transfer coefficient of the window decreased from $3.82\ to\ 3.07\ W/m^2K$, resulting in an energy conservation of 34.9% in comparison with a standard double-glazed window.
2. At an air velocity of $1000\ cc/min$, the heat transfer coefficient of the window decreased to $2.46\ W/m^2K$, and an energy conservation of 38.1% was achieved. Since the attainable waste air can supply two windows, it is possible to achieve a total energy conservation of 76.2%.
3. At an air velocity of $666\ cc/min$, the system demonstrated a slight improvement in the heat transfer coefficient of the glazing as well as a remarkable energy conservation of 83.1%. It's important to note that the attainable air velocity was sufficient to feed three windows at the same time.
4. When the air velocity was set to $500\ cc/min$, the U-value of the glazing decreased, resulting in a total energy conservation of 40.8%.

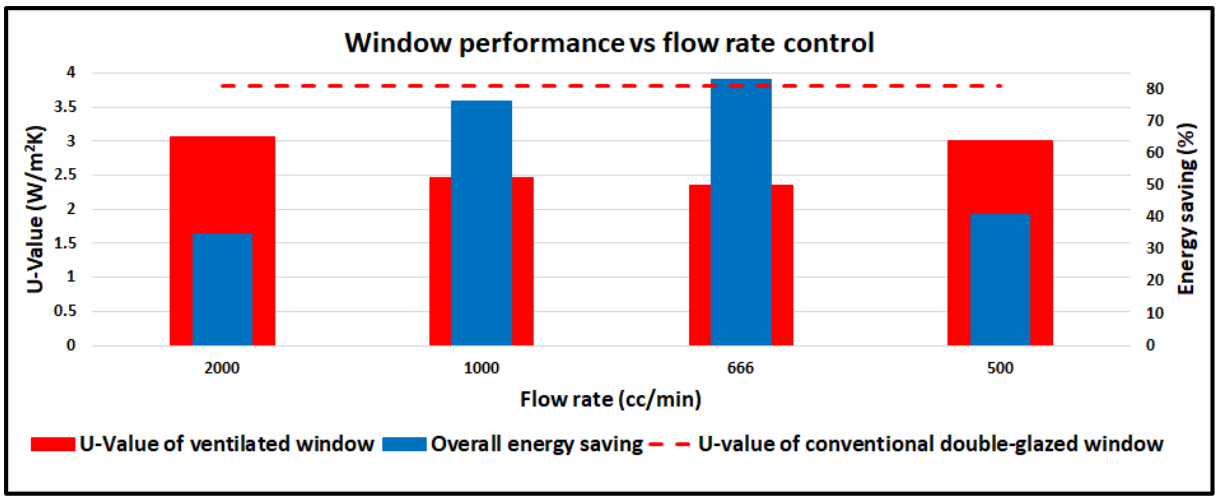

Figure 3. 16. *Thermal efficiency of the ventilated window using air velocity control.*

To summarize the strategy used in the scenarios performed, when distributing the waste air via selecting the optimal on/off duration for the pump (in scenarios $2\ to\ 4$), the first duration should be chosen to totally fill the gap between glazing panes every time the pump is run. Subsequent tries should be made using progressively shorter intervals until the shortest achievable duration for the air pump is reached. There is more heat loss via the window when the pump is off due to longer on/off cycles. However, the interval that results in the greatest amount of energy conservation is the optimal interval. When sharing the waste air by splitting the flow (in scenarios $5\ to\ 8$), several tries should be carried out on only one window, dual windows, triple windows, etc., until the optimal number of windows is determined that yields the greatest energy conservation.

In general, the proposed procedures for optimal usage of waste air are illustrated in the flowchart in Figure 3. 17. The flowchart begins by evaluating the expected energy savings S_{ref} when the typical double-glazed window is employed. The right column of the flowchart demonstrates the first method, which relies on setting the duty cycle of the air pump to 50% and then calculating the overall energy conservation with different on/off times set for the air pump, which are $S_i, S_{i+1}, S_{i+2}, \ldots etc$. On the other side, the column on the left of the flowchart represents the second method of waste air management, which relies on sharing the air with one or multiple windows, as explained formerly. Similarly, the overall energy savings are calculated in different cases, which are $S_j, S_{j+1}, S_{j+2}, \ldots etc$. In each method, the process stops in an iteration if the calculated overall energy savings is less than that in the reference case (S_{ref}). Finally, the calculated energy savings in both methods

$S_i, S_{i+1}, S_{i+2}, \ldots etc.$ and $S_j, S_{j+1}, S_{j+2}, \ldots etc.$ will be compared to that in the reference case (S_{ref}); the highest energy savings will be pointed out to the optimal case. The flowchart can be used for already constructed buildings or in the initial design stages of buildings to determine the optimal tactic that should be employed to optimally use the waste air in window ventilation. It is worthy to mention here that the procedures in the flowchart can be done manually or by employing the available special software.

The primary difference between scenarios $2\ to\ 8$ and the initial scenario is that forced ventilation increased the flow rate and temperature of the air in the glazing gap of the window, resulting in improved thermal performance. This alteration impacts the rate of convective heat transfer through the glazing panes, as noted in [90]. Additionally, the findings indicate that the cooling period of the test room is influenced by the pump's on/off duration, the velocity of the waste air, and how many windows can be supplied with the waste air. An example of the system's optimal efficiency was observed when three windows were sharing the attainable flow rate of $2000\ cc/min$. This configuration led to a decrease in the thermal conductivity of the window, allowing the room to preserve the target range of its temperature for a more time.

The suggested system demonstrated that the U-value of the glazing can be controlled by effectively managing the utilisation of the attainable waste air, provided that other factors affecting thermal performance remain constant. However, it should be noted that this study only examined the impact of heat transfer because of conduction and convection. For example, solar irradiation can also have a significant effect on the thermal efficiency of the glazing. A growing in the exterior temperature can lead to a decrease in the temperature variance between the interior and exterior environments, which in turn can result in a reduction of the overall heat loss through the window, leading to a reduction in the total heat loss of the glazing. Applying the suggested approach in hot areas could also be a viable option for reducing building cooling demands. In such cases, the chilled air would be used to ventilate the double-glazed window. However, the effectiveness of window ventilation can be reduced due to greenhouse effect resulting from solar radiation, which increases cooling demands, as indicated in previous studies [147]–[149].

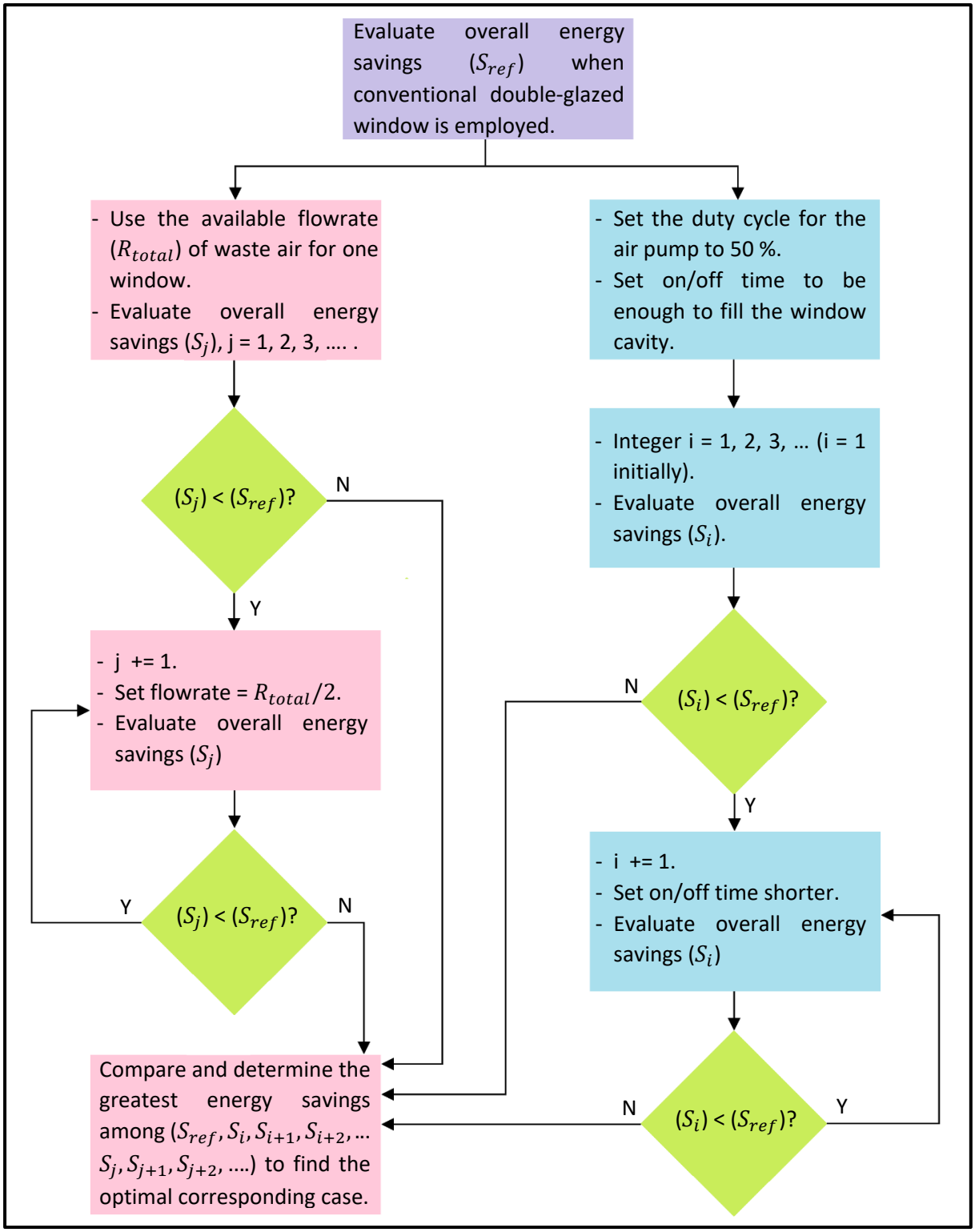

Figure 3. 17. Flowchart of waste air usage optimisation process.

The proposed methods of managing waste air can be influenced by different variables. For example, the number of residents in the building can affect the amount of air that needs to be changed per hour, and thus, affect the amount of attainable waste air. Increasing the velocity of the waste air can reduce heat conduction and convection via the glazing, leading to greater energy conservation. Moreover, when the difference between the desired interior temperature and the exterior temperature is large, the heat leakage via the glazing increases, necessitating a higher velocity of waste air to maintain the same amount of heat transfer.

In contemporary building design, it has become essential to select windows with a big window-to-wall ratio (WWR) to sustain a satisfactory level of visual comfort, allowing for exterior scenes and providing a naturally lit indoor environment for people inside. However, the larger window sizes present a challenge for achieving a higher velocity for the ventilation process. Hence, such scenarios highlight the significance of effective management of the utilisation of waste air in structures.

Other research has utilised the circulation of warm air within the gap between the glazing's panes as a means to enhance the effectiveness of double-glazed windows. One example is the study conducted by Nourozi et al. [90], which found that increasing the speed at which the air circulates can result in a decrease in the window's heat transfer coefficient. This conclusion was explicitly outlined by the authors. The researchers created a sophisticated design and incorporated Argon gas to lower the thermal conductance of the window. They also utilised a distinct heat exchanger to preheat the air prior to injecting it into the window. This approach led to a significant reduction in the heat transfer coefficient, achieving an impressive level of efficiency with a value of $0.2\ W/m^2K$. This outcome is reasonable considering the additional resources invested in the project. Nevertheless, the intricacy of their system may be more suitable for implementation in absolutely cold countries. The main point that the present research aimed to convey, however, was that in regions with typical climates where highly efficient windows may not be necessary, the experiment outcomes, in combination with the mathematical model of the heat transfer system, demonstrated that the suggested system for managing wasted air could lead to energy savings of up to 83.1% in heating loads. In the case of an already-constructed building, the suggested methodology may offer a more accessible and cost-effective alternative to replacing the existing windows with triple-glazed or other modernistic types of windows.

As previously noted, raising the flow rate and temperature of waste air can enhance the overall thermal efficiency of ventilated windows [90]. However, increasing the air velocity necessitates a higher flow rate, which in turn necessitates a greater quantity of waste air. The amount of waste air volume that is accessible within a building is identified by the assigned air change per hour of the forced ventilation system as well as the number of occupants [96].

In the current study, the test room runs under no-lighting conditions to eliminate the impact of solar irradiation on the thermal efficiency of the window. However, in real-world conditions where ventilated windows are subjected to solar influence, heat storage within the building will be inflated because of solar irradiance. As a result, the total thermal performance of the suggested system is likely to be even greater.

Organizing tactics for using the waste air suggested in the current study rely on distributing the accessible waste air to supply the greatest possible number of windows to accomplish the greatest energy conservation. Thus, the primary challenge that the suggested system may encounter is the accessibility of waste air, irrespective of the approach used to distribute the air among the windows.

Based on the results of scenario 7, the proposed system achieved optimal efficiency, resulting in an energy conservation of $56.5\ kWh$ in the heating load of the three miniature test rooms in a single year. Similarly, if a real-sized room with dimensions of $6\ x\ 5\ m^2$ and a height of $3\ m$ is provided with the suggested ventilated window, it could result in an energy savings of $40.6\ MWh$ annually. Moreover, for a building comprising 30 rooms, the energy savings could reach up to $1.22\ GWh$ per year.

3.4 Summary

This study focuses on optimizing the utilisation of waste air in the ventilation of the double-glazed windows to accomplish maximum energy savings in heating demand. Two techniques were used for the optimization procedure, both of which depend on distributing the waste air among multiple windows. One technique involves dividing the operation of the air pump based on time, where the air pump supplies more than one ventilated window, one at a time, repeatedly. The other technique involves simultaneously distributing the accessible waste air to various windows. The thermal efficiency of the window was assessed through experiment outcomes and the heat transfer numerical model. The primary conclusions of the research are:

1. To optimize the reduction of energy consumption for heating demand in buildings, it is possible to distribute the waste air to various ventilated double-glazed windows.
2. The study evaluated two ventilation methods, and the first method proved to be the most effective at saving energy, achieving a 50% reduction in energy consumption when the waste air was distributed to two windows in a cycle of $10\ seconds$ on and off. Compared to standard double-glazed windows, this method resulted in a 42.6% energy savings and reduced the U-value from $3.82\ W/m^2K\ to\ 2.8\ W/m^2K$.
3. The study also evaluated a second ventilation method and found that it provided the best thermal efficiency when the waste air was distributed simultaneously to three double-glazed windows using the accessible air velocity. This method resulted in a significant 83.1% energy savings in comparison with standard double-glazed windows and reduced the U-value from $3.82\ W/m^2K\ to\ 2.36\ W/m^2K$.
4. The study introduced the flowchart in Figure 3. 17 which involves the general procedures that can be employed in practical applications. The process can be used for in-use buildings or buildings under construction to determine the optimal method for waste air management.

Chapter 4: Quantification of visual comfort through polymer dispersed liquid crystal double-glazed windows

4. 1 Introduction

It is mentioned in chapter two that the polymer dispersed liquid crystal (PDLC) films are an efficient solution to mitigate energy consumption in hot regions. When a PDLC film is affixed to the traditional glazing of a window, it restricts solar radiation from accessing the internal environment. Hence, the greenhouse effect will be less, and this will lead to a lower need for cooling loads. However, lowering the optical transmittance challenges the visual quality through the glazing. In this chapter, two main points will be addressed. Firstly, developing a new method to quantify the visual quality via the PDLC windows and, secondly, determining the threshold value of visible transparency that maintains a minimum acceptable visual quality via the window.

This chapter suggests an approach using image processing to measure vision quality via PDLC windows. Experimentally, the suggested method was used on a double-glazed window with polymer dispersed liquid crystal (PDLC). The system instantly evaluates the contrast range that is available for views seen via the window. In order to retain the preferred level of vision within the identified vision range, the system modifies the PDLC film's biasing voltage. To ensure the comfort of the occupants, a preferred vision ratio (PVR) is suggested to be chosen by the occupants. Experimental research has been done to determine how the PVR ratio affects solar heat gain, daylight performance, and vision quality.

4. 2 Research Method

Figure 4. 1 shows the functional diagram of the suggested instant vision quantification system. It has two models: a model for image processing and a model for mathematics.

a. In order to create the image processing model, an artificial eye, for instance, an HD camera module, takes a series of pictures from interior environment of a room toward the exterior scenes via a PDLC double-glazed window. Every 30 minutes, sixteen images will be taken in a set. Each image is captured using a different setting for PDLC optical transmission, ranging from opaque to transparent. Following that, a proposed algorithm will be used to extract the

contrast value of the images one by one and finds the pair values of optical transmittance and contrast.

b. In order to create the mathematical model, an instant contrast slope will be derived between contrast values and the functioning transparency at each time the experiment is executed during the day. The minimum and maximum permitted values of image contrast at a particular time will be used to identify the vision comfort band. This will have an impact on the optical transmission of the PDLC film set and result in new transparency span constraints.

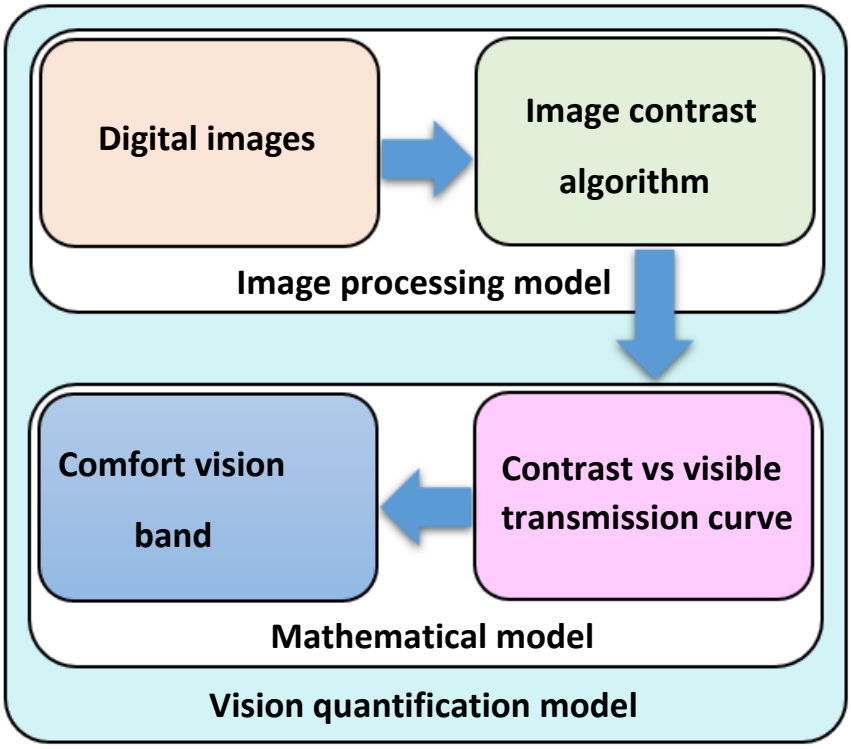

Figure 4. 1. *Functional diagram of the proposed visual comfort quantification system.*

4.2.1 Research method setup

As shown in Figure 4. 2, the experiment setup comes with a test room in addition to a data acquisition system consisting of sensors and data loggers needed for both internal and external measurements. A spectrometer tool was used in the lab to measure the glazing's optical characteristics. In order to employ the experimental exterior weather conditions for the simulation, a weather data file is also required; however, three types of data are needed to setup the file of weather data. First off, humidity, temperature, atmospheric pressure, wind

speed, and direction are all included in exterior weather data. Second, information on sunlight irradiation includes global vertical and horizontal irradiance as well as diffused horizontal irradiance. Furthermore, the direct normal irradiance (DNI) is additionally required for the preparation of the weather data file; equation (4. 1) [150] has been adopted to predict the DNI.

$$DNI = \frac{GHI - DHI}{\cos(\theta)} \quad (4.\ 1)$$

Where:

- DNI is the direct normal irradiance in $^{W}/_{m^2}$.
- GHI is the global horizontal irradiance in $^{W}/_{m^2}$.
- DHI is the diffused horizontal irradiance in $^{W}/_{m^2}$.
- θ is the Zenith angle in degrees.

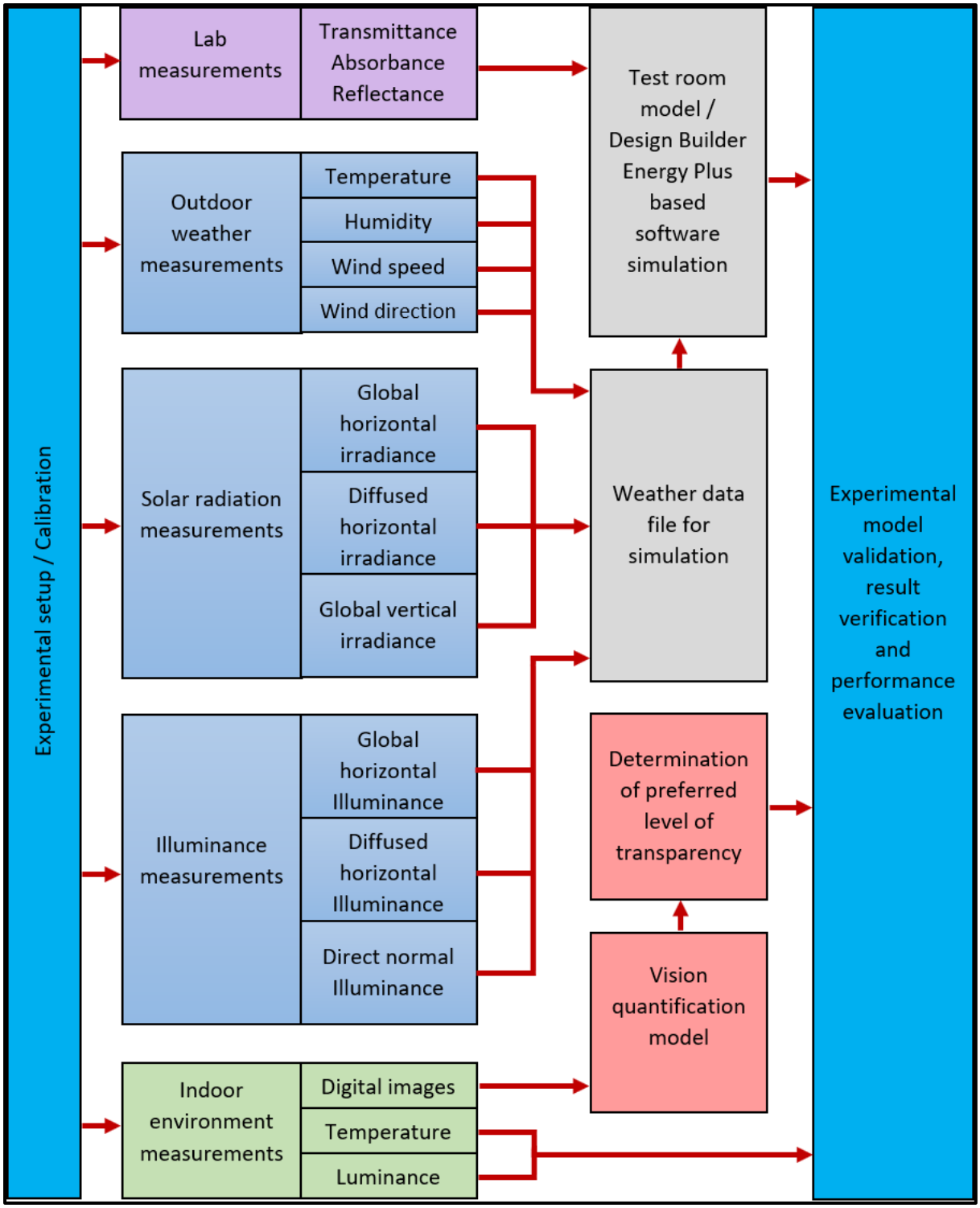

Figure 4. 2. *Setup of the proposed visual comfort quantification method.*

Third, the data on illumination includes direct normal illuminance, diffused horizontal illuminance, and global horizontal illuminance. The IESNA method by the engineering society of north America, as recommended by Kandilli and Ulgen [151], provides a proper estimation for the obtainable illumination in solar radiation for any given day of the year. The formulas

(4. 2) through (4. 7) below explain the illuminance determination processes according to the IESNA approach.

$$E_{XT} = G_{SC}\{1 + 0.034\cos[\frac{2\pi}{365}(n - 2)]\} \quad (4.\ 2)$$

Where:

- E_{XT} is the extra-terrestrial illuminance.
- G_{SC} is the solar illuminance constant.
- n represents the numerical value of a specific calendar day within the year.

Consequently, the direct normal illuminance E_{DN} can be predicted in equation $(4.\ 3)$.

$$E_{DN} = E_{XT}\exp(-cm) \quad (4.\ 3)$$

Where:

- m is the air mass, it can be determined by the following formula:

$$m = \frac{1}{\sin(\propto_S)} \quad (4.\ 4)$$

- $\propto_S$ is the angle of altitude in degree.
- The small "c" in equation $(4.\ 3)$ is a constant, it can be obtained from Table 4. 1 based on the state or appearance of the sky. Then, direct horizontal illuminance E_{DH} is predicted using equation $(4.\ 5)$.

$$E_{DH} = E_{DN}\sin(\propto_S) \quad (4.\ 5)$$

According to the clarity of the sky, the diffuse (or sky) horizontal illuminance E_{KH} can be determined by equation $(4.\ 6)$.

$$E_{KH} = A + B\,sin^C(\propto_S) \quad (4.\ 6)$$

$A, B\ and\ C$ are constants, their values depend on the clarity of the sky which is classified into cloudy, partly cloudy, and clear. Table 4. 1 demonstrates the values of sky constants in

different conditions. It is noticed that for a cloudy sky, the direct sun radiation has no value, thus, $E_{DN} = 0$.

Table 4. 1. *Constants of sky clarity.*

Clarity	c	$A\ (Klux)$	$B\ (Klux)$	$C\ (Klux)$
Clear sky	21	0.8	15.5	0.5
Partly cloudy sky	0.8	0.3	45	1
Cloudy sky	Direct radiation = 0	0.3	21	1

Lastly, the total illuminance E fall on the horizontal surface is described by equation $(4.\ 7)$.

$$E\ =\ E_{KH}\ +\ E_{DH} \tag{4. 7}$$

The test room's temperature and lighting level are measured experimentally indoors in order to assess the system's performance and validate it. In addition, digital images will be taken via the test room window and sent outside, where they will be processed using the suggested vision quantification model to instantly estimate the visual comfort band. The commercial Design Builder software's weather data file has been prepared using measurements of the exterior environment. The energy model was created using the software Design Builder. To accomplish the simulation, the model was fed with experimental weather conditions data and optical properties. The experimental model has been validated, the experimental result has been verified, and the system's performance has been assessed using both simulated and experimental data as well as the results of the quantification procedure.

4.2.2 Image processing calculations

For contrast estimation, the $RMS\ contrast$ approach in equation $(4.\ 8)$ is employed [152].

$$RMS\ Contrast\ =\ \sqrt{\frac{1}{M*N}\sum_{i=0}^{M-1}\sum_{j=0}^{N-1}\ (I_{ij}\ -\ \bar{I})^2} \tag{4. 8}$$

Where:

$M\ and\ N$ are the count of vertical and horizontal lines of the image I respectively which reflect the position of pixels in the image.

I_{ij} is the mean of pixel's value in the column number i^{th} and the row number j^{th}, or the brightness of the pixel I_{ij}.

$\bar{I}$ is the mean brightness of the image I and it is expressed in equation (4. 9) within the interval or range of zero to one.

$$\bar{I} = \frac{1}{M * N} \sum_{i=0}^{(M*N)-1} I_i \qquad (4.\ 9)$$

Each image in Figure 4. 3 was captured following the adjustment of the AC excitation of the PDLC within its input rating ($0\ to\ 200\ V$), as displayed in the figure. The images were taken in an outdoor environment throughout the day on a sunny day via a double-glazed PDLC window with different optical transmission levels.

Figure 4. 3. *The captured digital images during the experiment with various PDLC excitations.*

The contrast values for the taken images in Figure 4. 3 were computed; each contrast value corresponds to a particular PDLC excitation. Figure 4. 4 shows the relation between the contrast and the input excitation. The curve can be broken down into three distinct regions. In the first part, from the least contrast value (C_{min}) to point (C_y), the contrast is undoubtedly minimal because the PDLC film excitation is low and it is in an opaque state. In the second part, which is between the (C_y) point and the threshold contrast point (C_{th}). However, contrast values are significantly rise as the input excitation increases. The contrast begins a saturation response against the input voltage in the third region, which is extended from the threshold contrast point (C_{th}) to the highest contrast point (C_{max}).

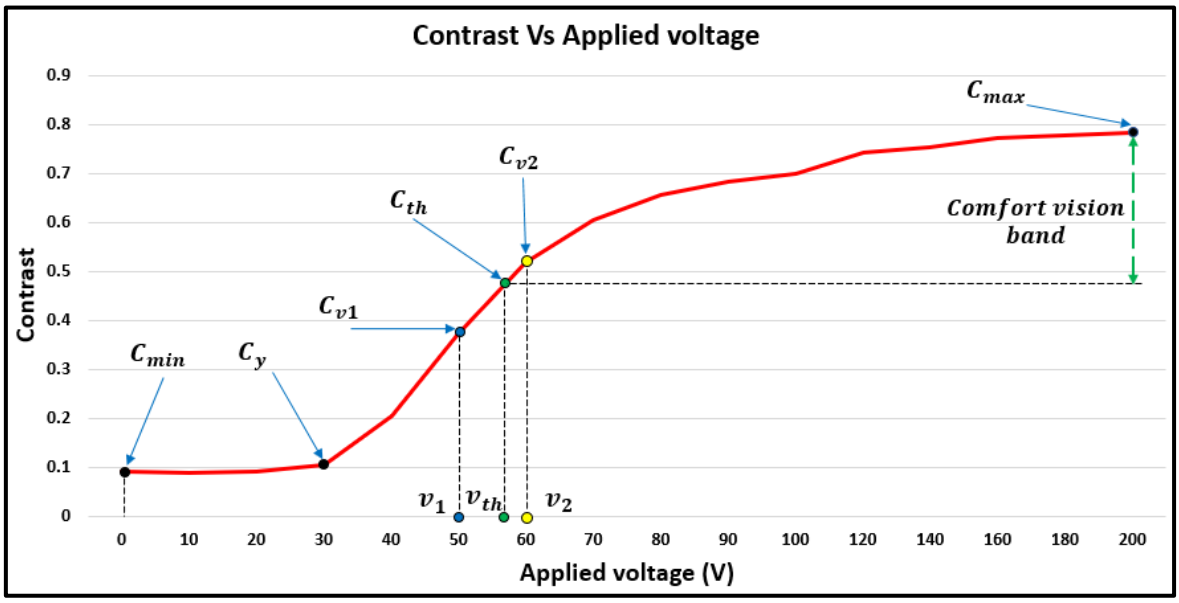

Figure 4. 4. *Relationship between the contrast versus PDLC excitation (contrast curve).*

The threshold value of contrast (C_{th}), which was schematically estimated from the contrast vs. voltage slope, is 0.48, above which the vision is accounted to be comfortable. This point does not, however, always relate to the same values of transparency and voltage. The suggested lowest comfort band that restricts the optical transmission of the glazing to be above is represented by the threshold contrast point (v_{th}, C_{th}). The threshold contrast value in Figure 4. 4 can be mathematically defined in the formula of equation Threshold Contrast ($4.\ 10$) as it is located between the two given points (C_{v1}, v_1) and (C_{v2}, v_2).

$$\text{Threshold Contrast } (C_{th}) = 0.707\ (C_{max}\ -\ C_{min}) \qquad (4.\ 10)$$

A reasonable approximation can be made to facilitate the calculations; the portion of the curve that lies between (C_{v1} and C_{v2}) will be considered a straight line in order to determine the threshold voltage (v_{th}). This presumption results in:

$\frac{C_{v2} - C_{th}}{C_{v2} - C_{v1}} = \frac{v_2 - v_{th}}{v_2 - v_1}$, or:

$$v_{th}\ =\ v_2\ -\ \left[(v_2\ -\ v_1)\ \left(\frac{C_{v2} - C_{th}}{C_{v2} - C_{v1}}\right)\right] \qquad (4.\ 11)$$

Therefore, according to the consumer's desire, the system selects one operational point on the comfort vision band. The user's desire will be taken into consideration and will be referred to (v_{th}). The user's selection range is from $0\ \%\ to\ 100\ \%$, which matches v_{th} to v_{max}. A preferred vision ratio (PVR) is suggested in this system as a way to identify the user's preference. As a result, if the $PVR = 0\%$, the working point is at the threshold value (C_{th}), while if the $PVR = 100\%$, the system operates at (C_{max}). Accordingly, the following formula can be used to determine the preferred contrast value (C_{PVR}):

$$\text{The preferred contrast value } (C_{PVR})\ =\ PVR\ (C_{max}\ -\ C_{th})\ +\ C_{th} \qquad (4.\ 12)$$

Equation $(4.\ 12)$ can be used in place of equation $(4.\ 11)$ to define the corresponding PDLC excitation voltage at the desired contrast, as demonstrated in the following:

$$v_{PVR}\ =\ v_b\ -\ \left[(v_b\ -\ v_a)\left(\frac{C_b - (PVR\ (C_{max} - C_{th}) + C_{th})}{C_b - C_a}\right)\right] \ldots\ldots\ldots\ 0\ \leq\ PVR\ <\ 1 \quad (4.\ 13)$$

4. 3 Experiment of quantification of vision through PDLC window

4.3.1 Experiment setup

Three layers of insulation board have been used to build two identically sized small test rooms. The main layer of the board is made from a solid layer of polystyrene with a thermal conductivity of $(0.046\ W/m.k)$. Two light layers of steel are sandwiched between the polystyrene. A traditional double-glazed window with the details listed in Table 4. 2 is present

in the first room. In the experiments, this space will serve as the reference model. The window in the other room is identical, but the inner pane of the double-glazed window has a PDLC thin film affixed to it. The suggested vision quantification method will be assessed in the second room. Both rooms are equipped with a flux sensor, fixed in the centre at a height of $15\ cm$, as well as a temperature sensor in each room to monitor the temperature of the internal spaces. More information about the design of the test rooms, the double-glazed windows, and the PDLC film can be found in Table 4. 2.

A weather station is used to monitor and save the temperature, humidity, pressure, wind speed, and wind direction for exterior weather conditions. Furthermore, three pyranometers are used to monitor the diffused horizontal irradiance (DHI), the global vertical irradiance (GVI), and the global horizontal irradiance (GHI). To gather the data, a datalogger is connected to every pyranometer; the next section has more details regarding the data acquisition system used in the experiment.

A $300\ V, 500\ VA$ manually controlled VARIAC transformer is employed in the second test room to set the preferred voltage because the experiments demand a an adjustable AC excitation for the PDLC film. Additionally, a high definition camera module is mounted in the space, $5\ cm$ from the window's interior glazing. To take an image of the scenes outside the window, the camera is horizontally positioned toward the window. The images are transmitted immediately after being captured from the digital camera to the computer through an IP network connection. Windows-based software is utilised to control the image capture process.

Moreover, a MATLAB program was created to calculate the contrast value of the images that were taken throughout the experimentation. This procedure happens every 30 minutes. The experiment setup is shown in Figure 4. 5, which also includes the reference test room, the PDLC test room, three pyranometers, and the weather station.

Table 4. 2. *Information on the experiment components.*

Items	Parts	Info
Insulated board	Thickness of the polystyrene layer	$4.9\ cm$
	Thickness of the steel layer	$0.05\ cm$
Length x width of the room's walls		$55\ x\ 55\ cm^2$
Length x width x height of the room's internal space		$45\ x\ 45\ x\ 45\ cm^3$
Double glazed window	Length x width of the glazing	$30\ x\ 30\ cm^2$
	Window to wall ratio (WWR)	$44\ \%$
	Type of the glazing	Clear
	Thickness of the glazing	$0.4\ cm$
	Thermal conductivity of the glazing	$0.9\ W/m.K$
	Optical transmittance of the glazing	0.83
	Reflectance of the glazing	0.12
	Absorbance of the glazing	0.039
	The distance of glazing gap	$2\ cm$
	Outside reveal depth	$0\ cm$
PDLC film	Rating of excitation	$220\ AC\ volt$
	Thickness of the film	$0.36\ mm$
	Optical transmittance (OFF / ON)	$0.05\ /\ 0.83$

Figure 4. 5. *Components of the experiment setup.*

A: Reference test room with double-glazed window (nearest), test room with the PDLC window (the furthest) and the pyranometer for measuring the vertical global irradiance (GVI) (red encircled).

B: Pyranometer for measuring the global horizontal irradiance (GHI).

C: The weather station.

D: Pyranometer for measuring the diffuse horizontal irradiance (DHI).

4.3.2 Data acquisition system

The data acquisition system shown in **Figure 4. 6** was employed to observe and record the data in the field during the experiment as following:

1- An Arduino microcontroller (MC-A) was responsible for gathering indoor temperature and indoor flux density inside the reference room (conventional double-glazed window room). In addition, the pyranometer that measures the vertical global irradiance was also connected to MC-A. MC-A reads the data from the sensors and stores it in the SD RAM.
2- An Arduino microcontroller (MC-B) was utilised to collect indoor temperature and indoor flux density inside the PDLC room (PDLC double-glazed window room). MC-B reads the data from the sensors and stores it in the SD RAM.
3- Three software were installed on a windows-based personal computer (PC): MATLAB, camera, and datalogger software. MATLAB software undertook contrast calculations for the images taken by the camera. On the other hand, two pyranometers were connected to a datalogger to monitor global horizontal irradiance and diffused horizontal irradiance. The datalogger was interfaced with the PC so the irradiance data could be readily monitored.
4- A manually adjusted output AC VARIAC provides a variable AC voltage excitation to the PDLC film attached to the PDLC window.
5- The weather station used in the experimental setup of chapter three was employed for the same purpose.

However, more technical details about the microcontrollers, sensors, and pyranometers that were used in the experiment are illustrated in Table 4. 3; The temperature sensor has the same specifications of that used in the experimental setup of chapter three.

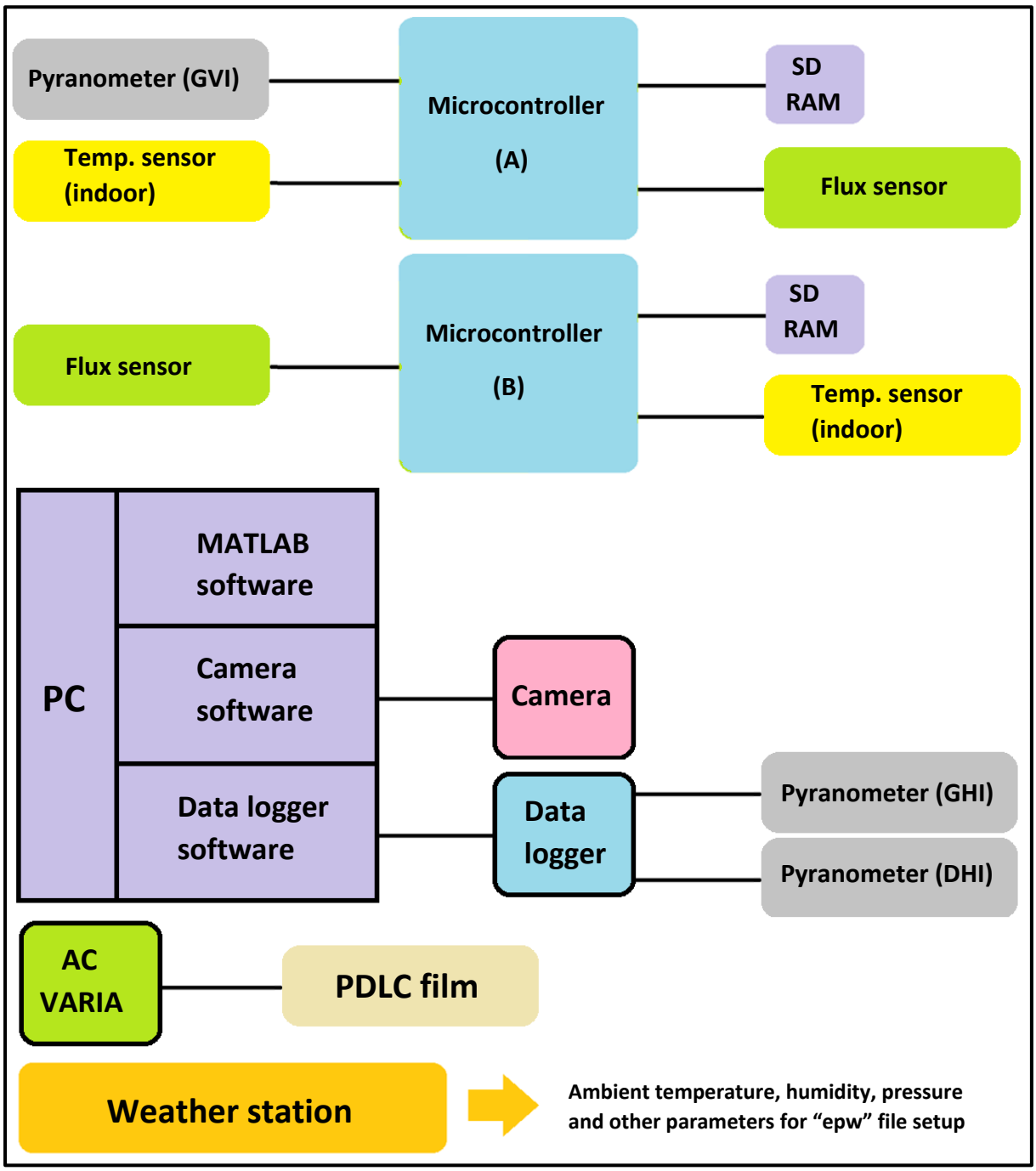

Figure 4. 6. *Data acquisition system of the proposed visual comfort quantification system.*

Table 4. 3. *Technical specifications of the sensors.*

Veinasa-ZFS Solar total radiation pyranometer (for global horizontal irradiance measurement)	Sensitivity	7 ～ 14 μV/W.m^{-2}
	Spectrum band	0.3-3 μm
	Range of measurements	0 ～ 2000 $W.m^{-2}$
	The type of output voltage	DC 12 V
	Type of the output port	RS485
	System latency	≤ 35s (99%)
	Resistance	about 350 Ω
	Stability	≤ ±2 %
	The cosine response	≤ 7 % (when the sun altitude Angle of 10 °)
	Error of azimuth response	≤ 5 % (when the sun altitude Angle of 10 °)
	temperature characteristic	± 2 % (-10 ℃ ～ +40 ℃)
	Working temperature	-40 ℃ ～ 50 C14℃
	Non-linearity	≤ 2%
Veinasa-SFS Scattered radiation pyranometer (for diffused horizontal irradiance measurement)	Power supply	DC 12 V
	measuring range	0 ～ 2000 $W.m^{-2}$
	Sensitivity	7—14 μV/W.m^{-2}
	Spectral region	0.3-3 μm
	Response time	< 35S (99%)
	Cosine response	≤ ± 7% (When the height angle of the sun is 10℃)
	Position	≤ ± 5% (When the height angle of the sun is 10℃)
	Output	0 ～ 2.5 V
	Latitude calibration range	0 ～ 50°
	Ring diameter	400 mm
	Line length Standard	2.5 m
	Shape size	410×500×500
	Working humidity	≤ 100% RH
	Working temperature	-50 ℃ ～ 85 ℃
Davis Instruments 6450 Solar Radiation pyranometer (for global vertical irradiance measurement)	Operating Temperature	-40° to +150° F (-40° to +65° C)
	Transducer	Silicon photodiode
	Spectral Response (10% points)	400 to 1100 nm
	Cosine Response Percent of Full Scale	±2% (0° to ±90°)
	Resolution and Units	1 W/m2
	Range	0 to 1800 W/m2
	Accuracy	±5% of full scale
	Time step	50 seconds to 1 minute
Flux sensor	Power supply	1.6 ~ 3.6 V DC
	Operating temperature	–40 ~ 85 °C
	Peak irradiance spectral responsivity	550 nm
	Resolution	0.01 lux
	Range of illumination	83865.6 lux

4.3.3 Scenarios of vision quantification experiment

The two test rooms have been set up on the rooftop of the Basra Oil Training Institute in Basra, Iraq (latitude: 30.5 and longitude: 47.8). Every room has a window that faces the south. From August 11 to August 14, 2021, the experiment was conducted continuously over four days during the day. Every day, a different PVR was set to carry out the experiment. The four scenarios, numbered 1 through 4, that were put into practice on the first through fourth days of the experiment are shown in Table 4. 4. It is important to note that PVR is only used for the window in the test room of PDLC window to demonstrate how it affects other system factors like interior temperature, interior daylight, and solar heat gain in addition to vision quality.

Table 4. 4. *Scenarios of experimentation.*

Scenario	Day	Test room 1 (reference room)	Test room 2	
		Window type	PVR	Window type
1	1st	Traditional double-glazed window	0	Double-glazed PDLC window
2	2nd		0.3	
3	3rd		0.65	
4	4th		1	

From $5{:}30\ a.m.\ to\ 6{:}30\ p.m.$, the experiment runs. The second room has been subjected to the procedure depicted in Figure 4. 7, $27\ times$ daily ($every\ 30\ minutes$); the procedures were done manually. Each manual execution of the process takes two minutes. The PDLC film voltage is first set by the algorithm to one of 16 possible values between $0\ and\ 200V$: $0, 10, 20, 30, 40, 50, 60, 70, 80, 90, 100, 120, 140, 160, 180, and\ 200$. For every voltage value, an image is captured once. The voltage-to-contrast relation and threshold value of the contrast (C_{th}) are then estimated by MATLAB.

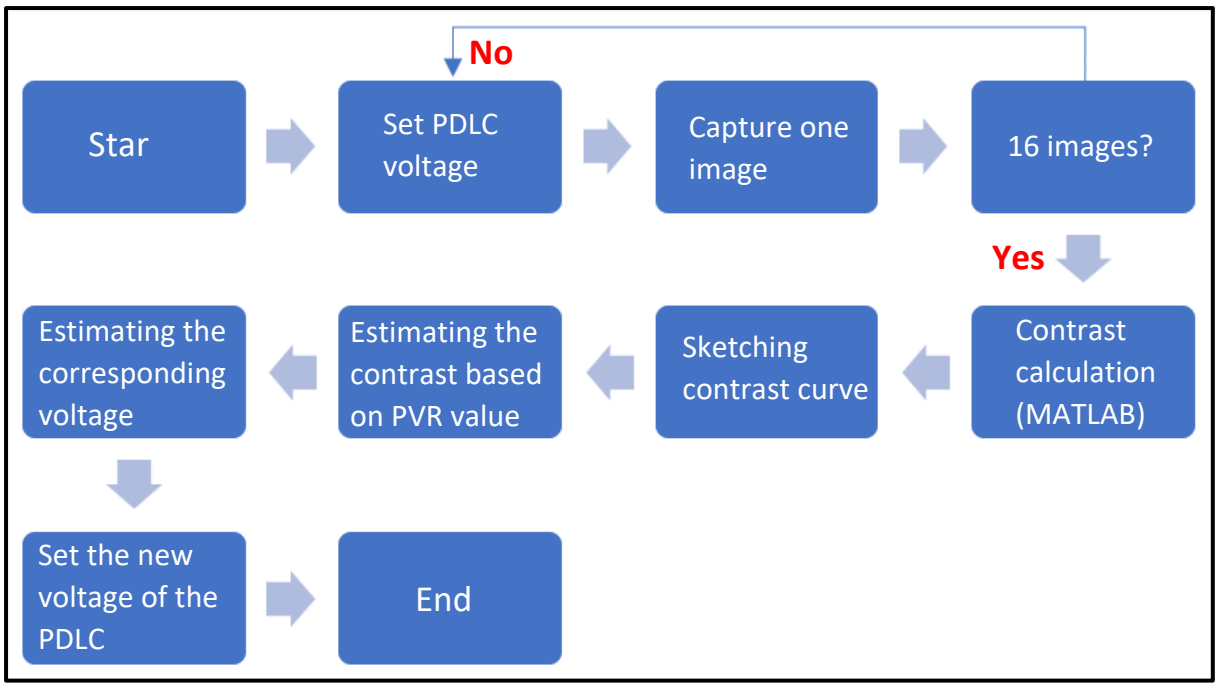

Figure 4. 7. *Quantification algorithm of vision through the PDLC window: experimental procedures.*

Following that, according to the selected value of PVR, the instant contrast values will be determined through equation $(4.\ 12)$. The instant contrast-voltage curve is represented graphically or by equation (4. 13) to yield the corresponding voltage. Lastly, in order to achieve the instant desired transmittance, the VARIAC output is manually adjusted to the new voltage value obtained from equation (4. 13). According to the selected PVR ratio, it should guarantee a certain level of visual comfort for the users.

4.3.4 Simulated test room models

According to the characteristics illustrated in Table 4. 2, both of the experimental test rooms, the primary room with the traditional double-glazed window and the other room with the PDLC double-glazed window, were modelled in the Design Builder software. At the same time, the weather data file necessary for the simulation was created using calculated illuminance data, experimentally measured solar irradiance data, and weather conditions collected by the weather station.

It is essential to impose the actual conditions of the experiment to the simulated models to guarantee a realistic simulation result. Consequently, it was essential to customize the visible transmittance of the PDLC film at different hours during the simulation because the visible transmittance of the film varied during the experiments. This goal was accomplished by making use of the optical transmittance-voltage curve of the PDLC film. The visible transmittance of the employed PDLC film was measured using a spectrometer against various input AC excitations, and the resulting curve is depicted in Figure 4. 8.

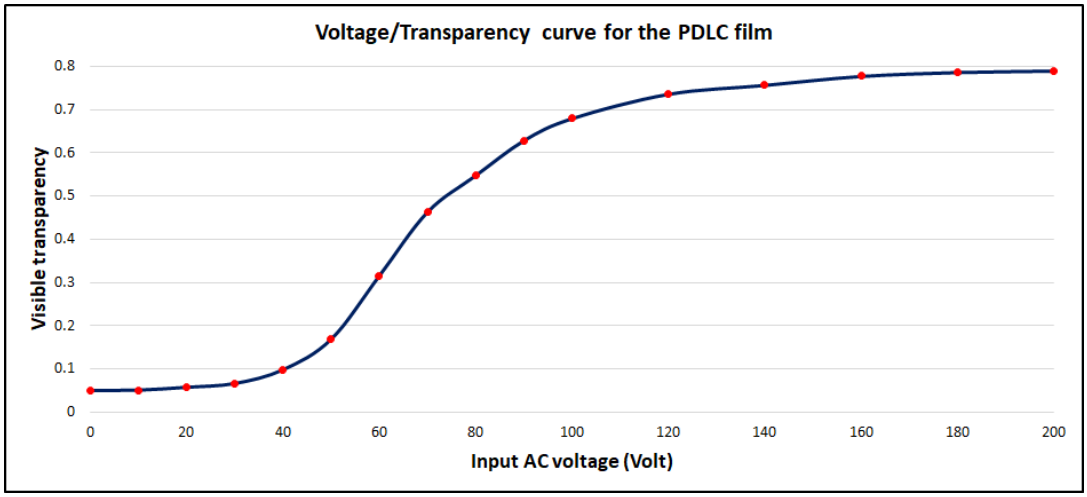

Figure 4. 8. *Relationship of transmittance versus the excitation for the utilised PDLC thin film.*

4. 4 Results of vision quantification experiment, validation, and discussion

The following are the section's goals:

a. displaying the simulation and experimentation findings for the applied scenarios listed in Table 4. 4.

b. To validate the system, results from simulations and experiments are compared.

c. examining the effects of the PVR ratio on various parameters of the system.

The illumination data, which includes direct normal illuminance, diffuse horizontal illuminance, and total illuminance, have been determined for the 11th–14th of August 2021 using the IESNA method provided by equations $(4.\ 2)$ to $(4.\ 7)$. As depicted in Figure 4. 9, the computation result revealed that the accessible calculated illumination throughout the four days is roughly equal; the actual daylight period is From 5 o'clock in the morning until 7 o'clock

in the evening. This is due, in part, to the experiment's successive days, where the sun's inclination angle is nearly identical, and, in part, to the four days' shared sky clearness parameters (sunny days).

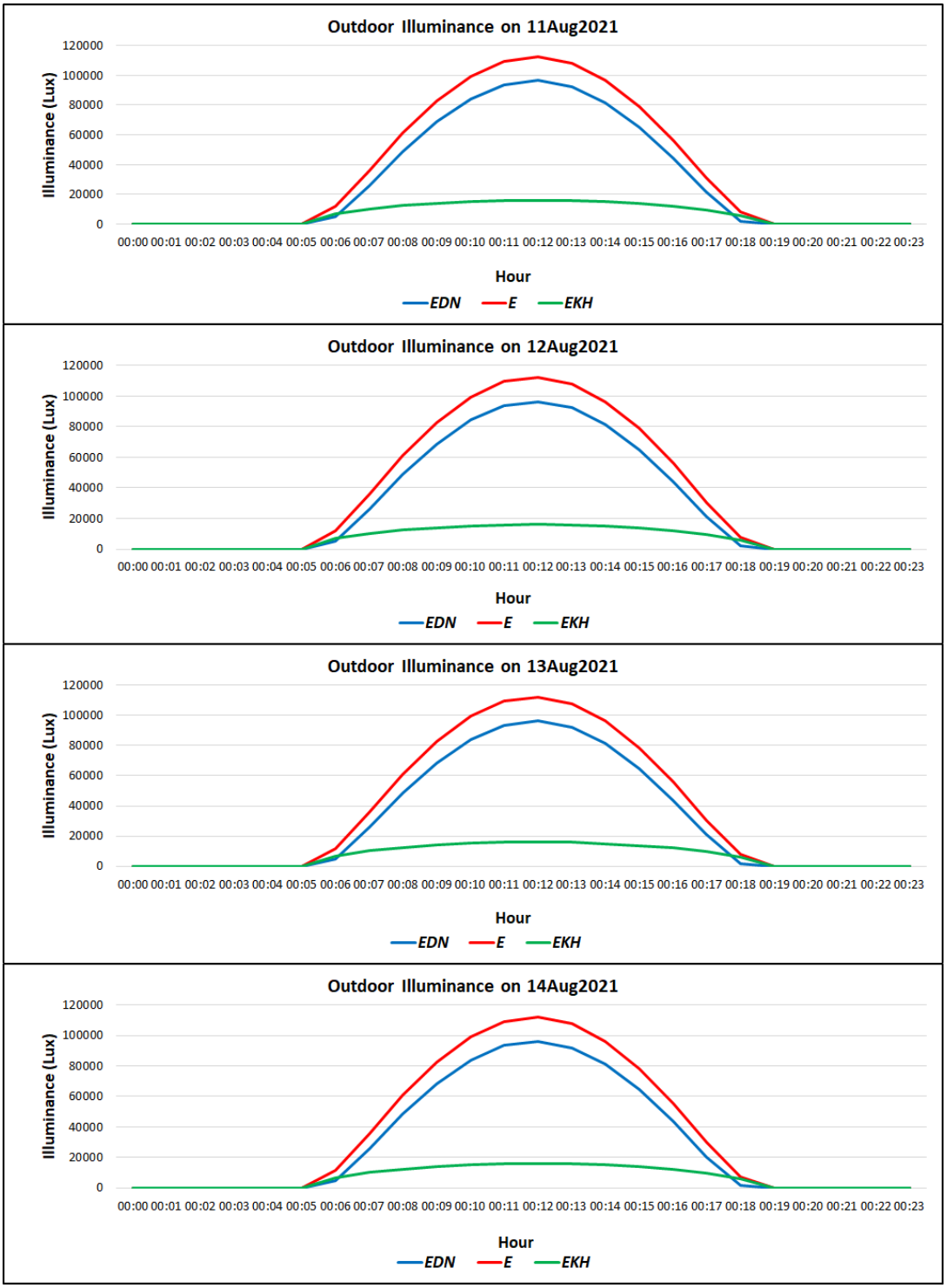

Figure 4. 9. *Estimated illumination data throughout days of the experiment according to the IESNA method.*

Figure 4. 10 displays the solar radiation data for the experiment execution days, involving global horizontal irradiance (GHI) and diffuse horizontal irradiance (DHI); solar irradiation has a slight variation from August 11 to August 14.

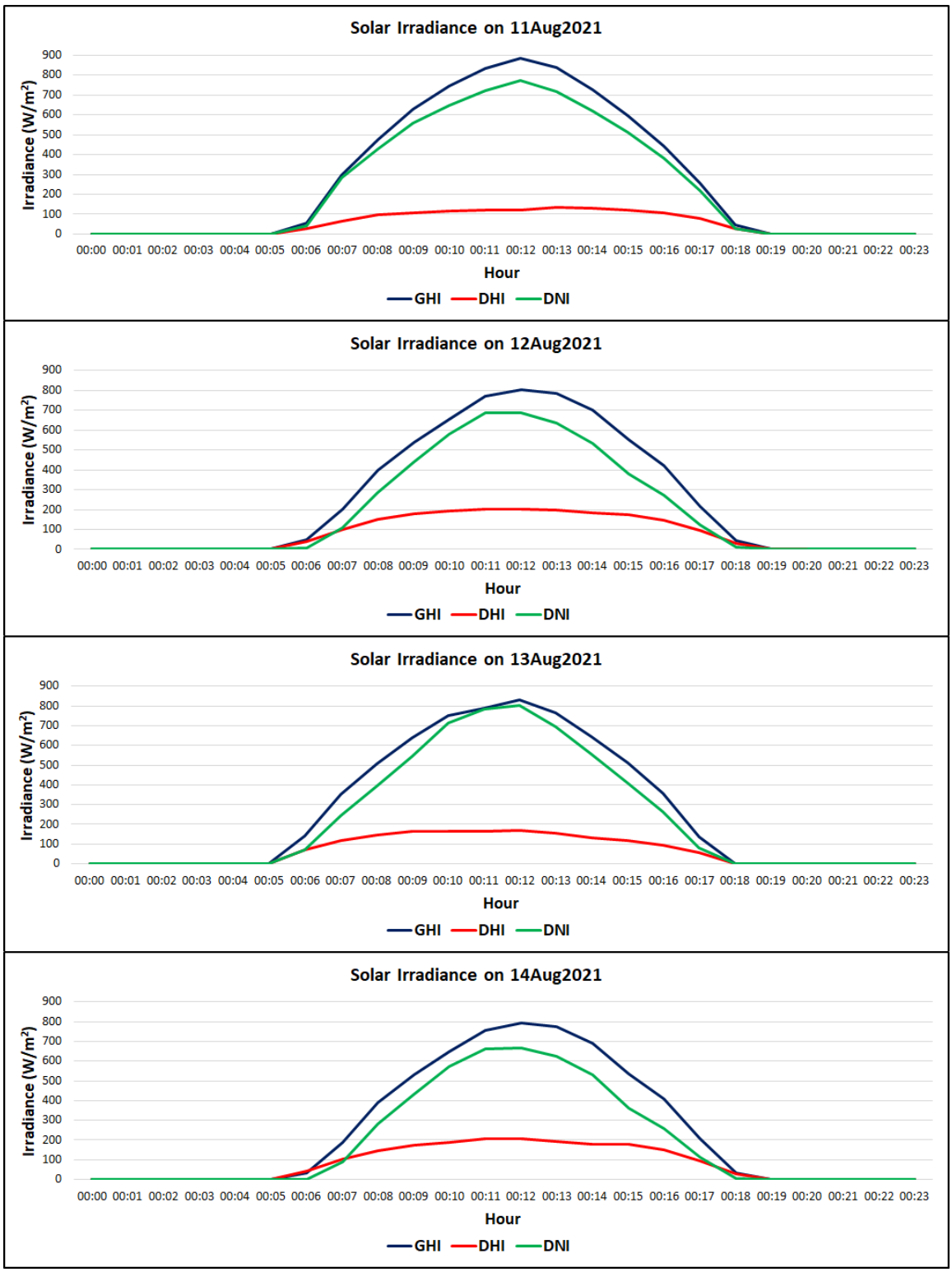

Figure 4. 10. *Measured solar radiation data throughout experiment days.*

Figure 4. 11 shows a plot of the test rooms' indoor and outdoor temperatures over the course of the experiment's days. The experimental and simulated interior temperatures were responding to the fluctuation of the outside temperature with proper mutuality on the first day while the PVR ratio was set to 0, which equates to the lowest attainable contrast within the visual comfort band. The highest and mean temperatures for the reference model at $2{:}00\ p.m.$ were $58.8°C\ and\ 41°C$, respectively, while these values for the PDLC test room model were $56\ °C\ and\ 38\ °C$, respectively. Inside the double-glazed window room and PDLC test room, the mean difference in temperature between the experimental and simulated readings was $0.12°C\ and\ 0.37°C$, respectively.

The experimental and simulated interior temperatures changed in a similar way as the outside temperature on the second day, when the PVR ratio was set to 0.3. The interior temperatures of the two test rooms in the experiment and simulation are roughly equivalent. Additionally, the highest and mean temperatures in the reference test room at $2{:}00\ p.m.$ were $61.7°C\ and\ 41.5°C$, respectively, whereas they were $58.5°C\ and\ 39.4°C$ for the PDLC test room. Inside the reference test room and PDLC test room, the mean deviation between the experimental and simulated temperatures was $0.19°C\ and\ 0.22°C$, respectively.

Similarly, findings were made on day three, when the PVR ratio was 0.65. The highest and mean temperatures recorded inside the reference test room at $2{:}00\ p.m.$ were $62°C\ and\ 42.3°C$, respectively, while these values were $60.7°C\ and\ 40.8°C$ for the PDLC test room. In the room with the reference window and the PDLC room, the mean difference in temperature between the experimental and simulated readings was $0.1°C\ and\ 0.3°C$, respectively.

On day four, when the PVR ratio was equated to 1, the reference test room experienced a high temperature of $58.6°C\ at\ 2{:}00\ PM$ and a mean temperature of $40°C$, while these values were $57.5°C\ and\ 38.8°C$ for the PDLC test model, respectively. Inside the reference test room and PDLC test room, the mean differences in temperature between the experimental and simulated readings were $0.2°C\ and\ 0.24°C$, respectively.

Undoubtedly, as $preferred\ vision\ ratio\ (PVR)$ values increased, the temperature of the PDLC test room also increased. For example, for PVR values of $0, 0.3, 0.65, and\ 1$, the mean

temperature of the reference test room was higher than that of the PDLC test room by $3C°, 2.1C°, 1.5C°, and\ 1.2C°$, respectively. On the other hand, as the PVR ratio rises, the temperature of the PDLC test room grows closer to the temperature in the reference test room. This is due to the fact that as the PVR ratio rises, the optical transmittance of the PDLC test room increases, allowing further solar radiation to penetrate the window towards the internal environment.

Figure 4. 12 displays actual and simulated daylight in lux, which indicate the level of illumination in the test rooms at the location where the flux sensor was installed during the setup of the experiment. The simulation result of the interior illumination have been plotted as ranges at various times of the day. This is due to that the Design Builder software offers a range of illumination levels that the illuminance for a specific point lies within it. Additionally explained in Figure 4. 12 is $vertical\ global\ irradiance\ (VGI)$.

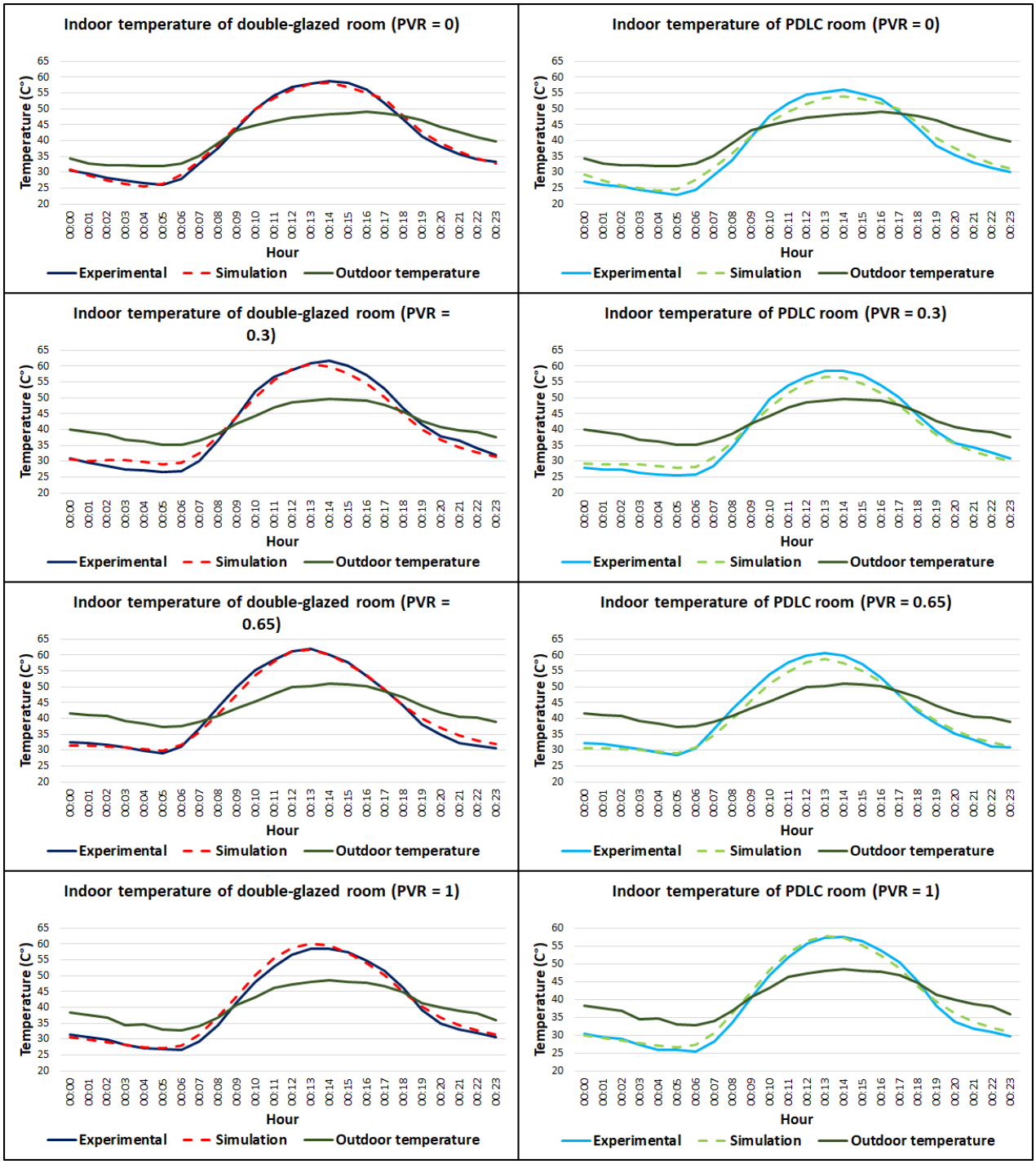

Figure 4. 11. *Measured indoor test rooms temperature vs. PVR ratio throughout experiment days.*

The experimental and simulated inside illumination reacts to changes in the outside $vertical\ global\ irradiance$ (VGI) with a high association starting on the day one of the experiment and a PVR ratio of 0. At $12{:}00\ p.m.$, the reference test room's maximum recorded illuminance (at the greatest radiation of the VGI) was $4.1\ Klux$, while the PDLC test

room's maximum and mean recorded illuminances were $3\ Klux$ and $1.9\ Klux$, respectively. The PVR settings for other days show comparable trends.

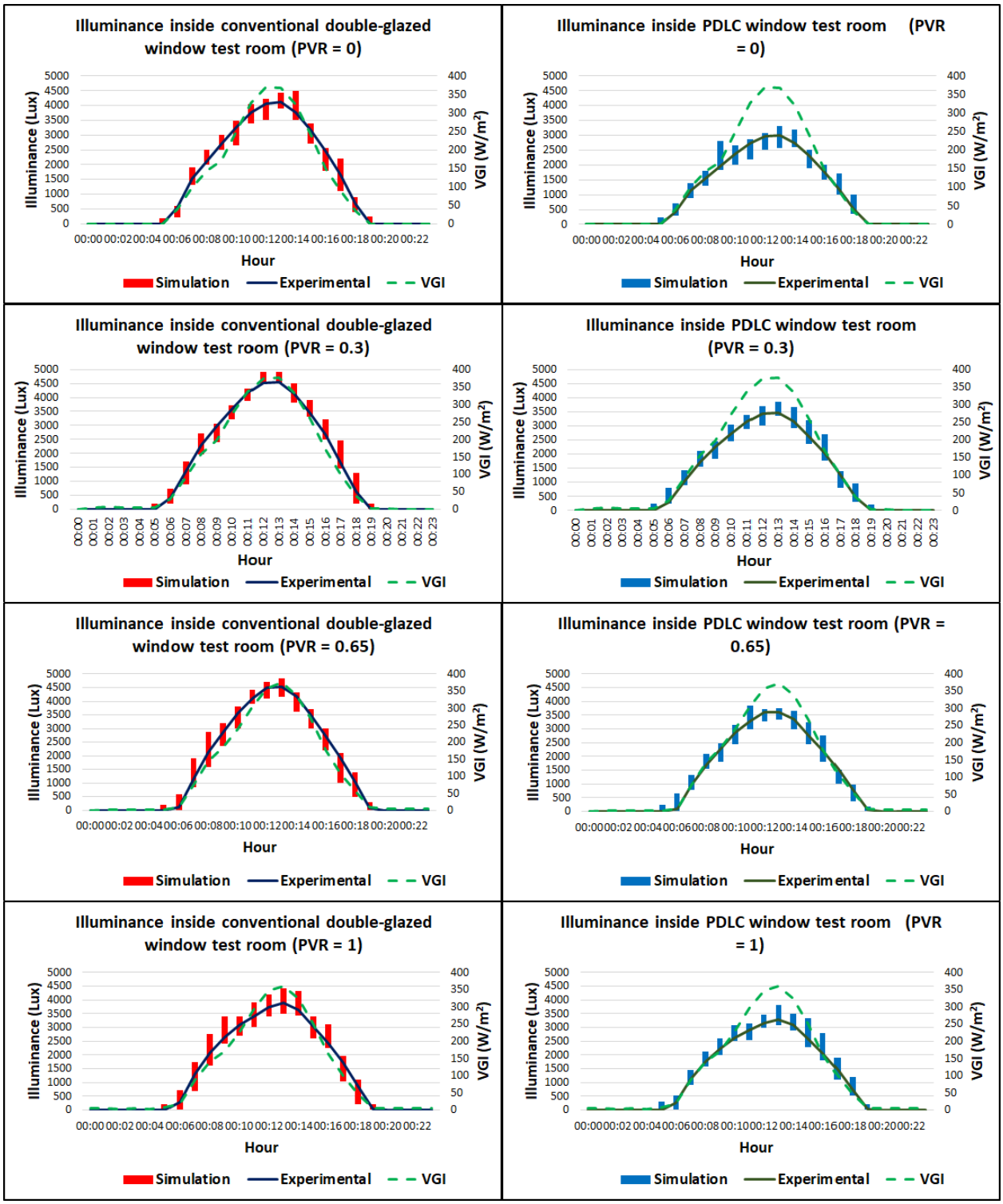

Figure 4. 12. *Measured indoor illumination vs. PVR ratio throughout experiment days.*

Further daylight entered the interior environment as the PVR ratio increased. For instance, on the first day of the experiment, while the PVR was equated to 0, the mean amount of daylight in the PDLC test room was 73% higher than in the reference test room. After that, the percentage of daylight increases to $76\%, 80\%, and\ 85\%$, respectively, for PVR values of $0.3, 0.65, and\ 1$. The PVR can be raised to increase the visible transmission of the glazing and let additional sunlight into the PDLC test room, as was earlier stated. Inside the reference and PDLC test rooms, the mean difference between experimental and simulated daylight was $20\ lux\ and\ 39\ lux$ on the first day, $57\ lux\ and\ 69\ lux$ on the second day, $81\ lux\ and\ 29\ lux$ on the third day, and $39\ lux\ and\ 108\ lux$ on the fourth day, respectively.

Due to the varying optical transmittance of the PDLC window in comparison to a standard double-glazed window, the solar heat gain coefficient $SHGC$ has different levels accordingly. Consequently, the solar heat gain inside both test rooms had different levels. Figure 4. 13 illustrates the experimental falling solar irradiance on the vertical level of the window and simulated solar heat gain for both test rooms throughout the experimentation days.

The PDLC window has a different $solar\ heat\ gain\ coefficient\ (SHGC)$ than a traditional double-glazed window due to its variant optical transmission. As a result, there was a difference in the solar heat gain between the two test rooms. Figure 4. 13 shows the simulated solar heat gain for the two test rooms over the course of the experiment as well as the experimentally measured falling solar radiation on the window. The falling solar radiation on the window was estimated from the measured $vertical\ global\ irradiance\ (VGI)$, taking into account the area of the PDLC window.

The peak solar heat gain occurred at $12{:}00\ p.m.$, with functional hours occurring between $5{:}00\ a.m.\ and\ 6{:}00\ p.m.$ The heat gain values follow the fluctuation of the window's falling solar irradiation. The greatest heat gain in the reference test room on day one of the experiment with a PVR ratio of 0 was $14.6\ W$, with a mean value of $8.32\ W$. As opposed to that, the mean heat gain was $1.38\ W$, with $2.23\ W$ being the greatest value recorded in the PDLC test room. In addition, the reference test room's higher observed heat gain was $17.85\ W$ and a mean value of $8.95\ W$ with a PVR ratio of 0.3, whereas the PDLC test room's greatest captured heat gain was $4.25\ W$ and an average value of $2.24\ W$.

Moreover, while the PVR ratio was equated to 0.65, the reference test room's greatest noted heat gain was $17.8\ W$, with a mean value of $8.81\ W$. In a like manner, the PDLC test room's highest recorded value was $5.88\ W$, with a mean value of $3.05\ W$. The heat gain in the reference room peaked at $18.28\ W$ and averaged $9.09\ W$ on the fourth day of the experiment with a PVR ratio of 1, with a greatest noticed gain in the PDLC test room was $8.33\ W$ and a median value of $4.28\ W$.

The mean heat gain in the PDLC test room was only $16.6\ \%$ compared to that of the reference room with a PVR of 0, 25.1% with a PVR of 0.3, 34.7% with a PVR of 0.65, and 47.1% with a PVR of 1. It is evident that increasing the preferred vision ratio PVR causes the heat gain in the PDLC test room to increase. Additionally, the Design Builder software determined solar heat gain coefficients of 0.42, 0.49, 0.56, and 0.78 compared to PVR ratios of $0, 0.3, 0.65$, and 1 respectively.

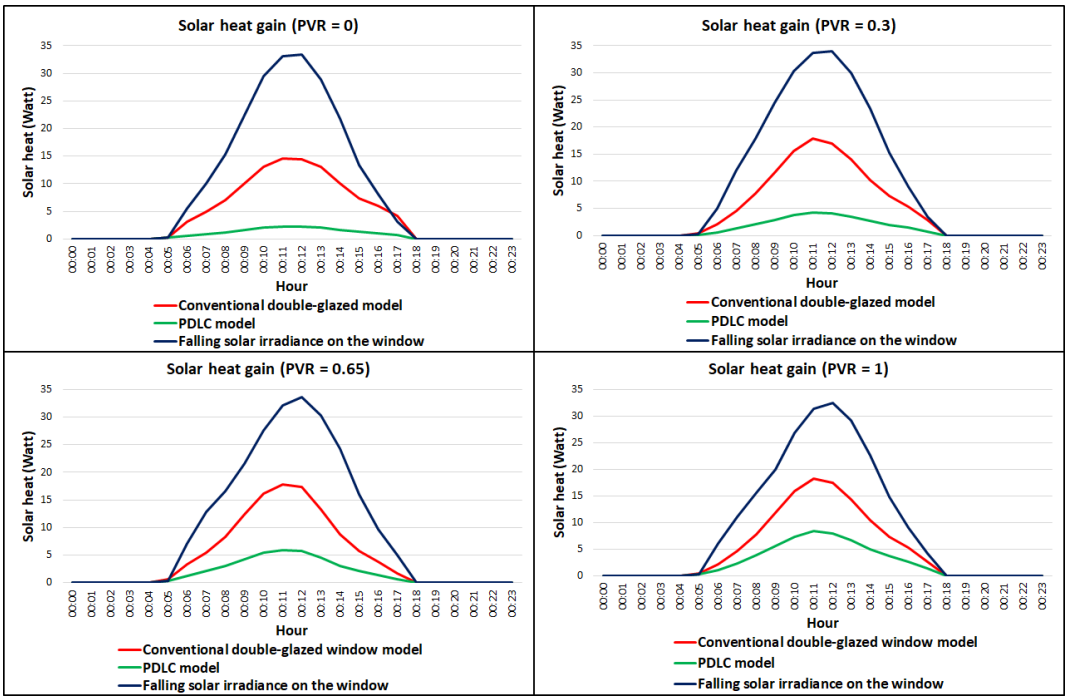

Figure 4. 13. *Measured solar heat gain vs. PVR ratio throughout experiment days.*

As previously explained, changing the PVR ratio directly affects the visual quality observed through the PDLC window. , this is due to the fact that it defines the operating point on the comfort vision band of the contrast-voltage curve, which acts as the contrast value of the instantaneous external scene seen through the window. Consequently, the visible

transparency is estimated accordingly. Figure 4. 14 depicts the contrast values during daytime that determined by the proposed algorithm along the days of the experiment. Obviously, opting higher PVR ratio prompts the system to step up the contrast, thus, the average contrast value was 0.18, 0.25, 0.31, and 0.37 for PVR ratio of 0, 0.3, 0.65, and 1 respectively.

However, Figure 4. 14 shows a fluctuation in the contrast value during the daytime. The suggested system raises the contrast level throughout first and late hours of the daytime (low illuminance hours). On the other hand, when the external environment provides excessive illumination, the system reduces the contrast during midday hours. Thus, the contrast was at its lowest point at the time of highest outdoor illuminance, which was at 12:00 pm.

Throughout the experiment, the contrast-voltage curve were exacerbated while minor luminous duration, or shrunk while major luminous duration, therefore, comfort vision band was widened or limited based on that. This modification in contrast/voltage curve led to a change in the PVR ratio, therefore, the system tried to fix the value of PVR ratio by modifying the contrast value simultaneously.

The system's response to the outdoor illuminance imitates the behaviour of the human eye. The human eye's pupil controls the amount of light entering the eye to ensure a specific level of visual acuity, it has a dilatable diameter to achieve light controlling action the pupil can dilate or constrict in diameter to realise its function [153].

As previously stated, the proposed algorithm was implemented every 30 minutes during daylight hours; Nonetheless, the experiment indicates that the achieved contrast values were close to the desired setpoint. Increasing the processing frequency to every 10 minutes, for instance, can result in more accurate contrast values.

For practical purposes, the current study made the assumption that the scene remains stationary during image capture. However, if the view were to change suddenly, such as by the appearance of dirt, dust, or rain on the window, two outcomes could occur. Firstly, If the sudden change is minor, it is unlikely to have an impact on the contrast calculation. Secondly, However, if the sudden change is significant, it may result in an atypical form for the contrast curve. In such a scenario, the quantification process would need to be adjusted to detect and

accommodate such changes in real-time using image processing techniques to overcome this limitation.

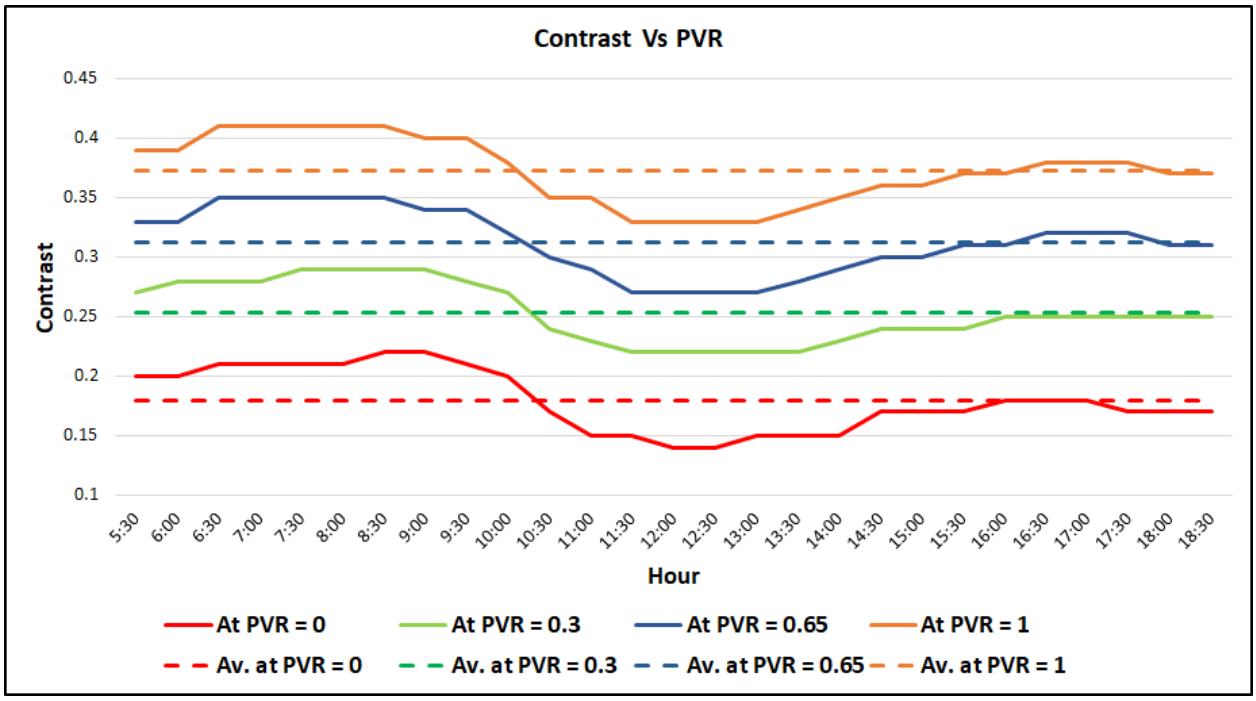

Figure 4. 14. *Estimated contrast values vs. PVR ratio throughout experiment days.*

Figure 4. 15 is retrieved from [154], it shows the impact of the hysteresis phenomenon on the relation between the visual transmission and excitation voltage in PDLC films. As depicted in the figure, the variation of the transparency against the applied voltage has two different paths. The red and pink paths represent the change in transparency while increasing and decreasing the applied voltage, respectively. The reason behind the hysteresis phenomenon is that when the voltage is raised and the PDLC film is saturated (all molecules are aligned in one direction), the electrical charge remains even after disconnecting the PDLC film from the excitation voltage. As a result, for an excitation value, the transparency in the second path (due to the hysteresis phenomenon) could be higher than the value in the first path [155].

In the present experiment, the influence of hysteresis was not considered. However, the deviation between the two curves could be a challenge in practical applications. If a controller is designed to run the proposed quantification algorithm, the hysteresis path of the utilised PDLC film may be trained by the system to guess the correct value of the preferred voltage with high accuracy.

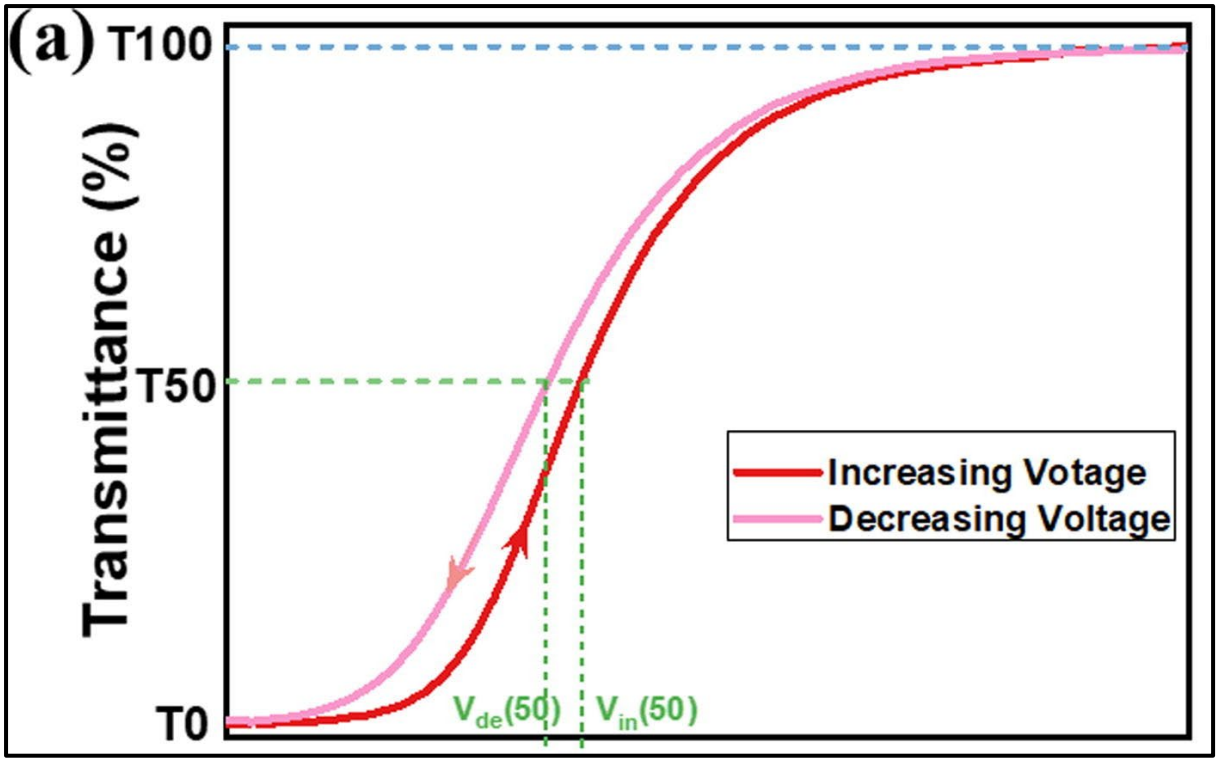

Figure 4. 15. *Hysteresis in PDLC films, retrieved from* [154].

Figure 4. 16 depicts the system's general evaluation in terms of the amount of daylight entering the inside environment, the inside temperature, solar heat gain, and vision contrast via the window, all of which are directly related to the PVR ratio.

It has been determined that increasing the PVR ratio improves visibility via the proposed PDLC window and the effectiveness of daylight in enclosed spaces. However, this situation causes buildings to gain more heat inside, which increases the mean interior temperature and necessitates higher cooling load energy consumption in hotter climates. The provision of good vision quality is unquestionably a challenge, though, and a trade-off can be taken into account. As opposed to that, the difficult trade-off may be simpler for a temperate climate, like the UK, as the lower temperature is anticipated to increase energy consumption. Utilising recently developed thin films shouldn't impair vision through windows, but to achieve the best overall performance, achieving a balance between energy consumption, visual quality, and daylight performance is crucial.

The results of the experiment demonstrated that using typical low dynamic range (LDR) images produces acceptable values for the (contrast vs. voltage curve. The use of high

dynamic range (HDR) images can produce contrast curves with greater accuracy. But HDR images have a larger colour data width (16 bits as opposed to 8 bits in LDR images), which will complicate the image processing controller and effectively drive up the cost. When the processor is being implemented, it will be possible to contrast the processing effectiveness between LDR and HDR images and assess the accuracy of contrast values in each scenario.

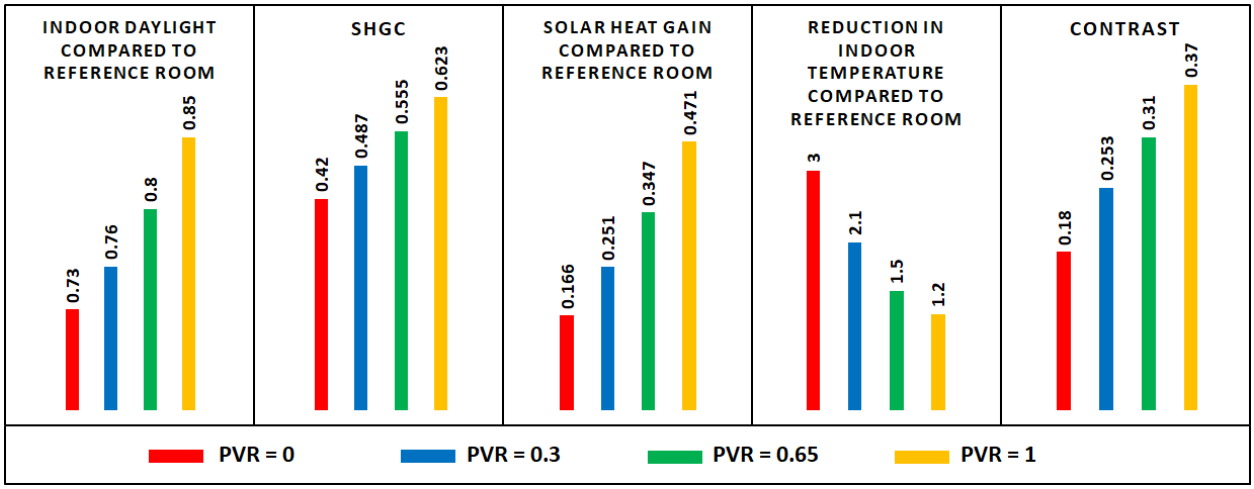

Figure 4. 16. *Results summary of vision quantification experiment.*

According to the quantification algorithm's procedures, if a commercial structure were to be outfitted with the proposed system, the optical transmittance of the windows would, in our case, alter from a translucent to a transparent mode every half an hour. For the experience of the occupants, this is unacceptable. It is suggested that the quantification procedures be carried out on a reference window situated in a less recognized area and that the data and transmittance and PDLC excitation settings be distributed to other glazing in the building each time the quantification process is performed.

It is important to note that the suggested quantification approach can be used to assess the quality of vision via other types of typical and smart windows in addition to PDLC windows, whenever this is necessary. However, typical windows offer high-quality exterior views primarily because of the glass's high visible optical transmittance; as a result, the suggested quantification approach may be more necessary in the applications of smart windows.

4. 5 Summary

In order to provide the occupants with a comfortable visual environment, the goal of this research is to quantify the vision via smart windows by employing an image processing method. A small room with PDLC double-glazed window has been introduced as an illustration of how the suggested system can be implemented. It has been suggested to use online image processing to limit the optical transmittance range of the PDLC film to levels that are comfortable for the occupants while simultaneously determining the attainable visual comfort from the (contrast vs. voltage) relationship of the PDLC film. The two main conclusions are the mathematical definition of the visual comfort band for PDLC double-glazed windows and the introduction of the $Preferred\ Vision\ Ratio\ (PVR)$, which guarantees the occupants' comfortable level of vision. The following can be used to summarize the main findings of this work:

1. The contrast of the views determined via the window in relation to the exterior environment can be used to quantify vision via smart windows.
2. Building occupants may choose their preferred scale of vision via the window using the suggested PVR ratio.
3. The experiment demonstrates that modifying the PVR ratio from 0 to 1 can change the mean contrast value in a clear sky environment from 0.18 to 0.37.
4. To guarantee the minimum acceptable vision quality, the suggested algorithm guarantees that the optical transmittance of the window will not be lower than a threshold value (C_{th}).
5. The experiment demonstrates that increasing the PDLC window's PVR ratio from 0 to 1 causes the $solar\ heat\ gain\ coefficient\ (SHGC)$ to increase from 0.42 to 0.623.
6. The experiment demonstrates that raising the PVR ratio of the PDLC window from 0 to 1 permits further light to penetrate to the interior environment of the test room ($73\%\ to\ 85\%$ more than with traditional double-glazed windows).

The Design Builder commercial software was adopted to simulate the test rooms according to the experimental weather conditions, and the simulation outcomes were contrasted to the experiment's findings to show the validity of the experimental models. Using the suggested system in commercial buildings limits vision via smart windows to the comfortable vision range. Additionally, it allows to replace the traditional methods of assessing people's

preferences, saving time and effort. Upcoming research can also use the suggested PVR ratio to assess the clarity of vision via smart windows. In conclusion, The suggested system enhances observability and controllability for building managers, leading to improved living conditions and greater comfort for occupants.

Furthermore, the suggested quantification method can be implemented using an embedded system, which speeds up the operations and produces more accurate instant optical transmittance levels for glazing; however, this task will be handled in chapter five.

Chapter 5: Prototyping of automated quantification controller for vision through PDLC double-glazed windows

5.1 Introduction

In chapter four, the contrast-based algorithm was introduced to quantify the vision quality through double-glazed PDLC windows. The present chapter demonstrates the implementation of the automated system that realise the vision quantification algorithm. As mentioned in the literature, designers utilised numerous techniques to realise different functions for practical applications; each technique relies on special hardware and software. However, the present chapter employed four methods to implement the vision quantification function: MATLAB software, Raspberry-Pi system on-chip, Cortex-A9 microcontroller, and (FPGA) field programmable gate array techniques. The implemented systems showed a wide range of performance in regard to processing speed, throughput, latency, power consumption, and cost.

5.2 Research method and the proposed quantification system

It is crucial to first follow the procedures that were used in chapter 4 to realise the quantification process manually because the goal of this work is to automate the vision quantification process by implementing an appropriate controller for this purpose:

1- An image processing model: a collection of sixteen manually taken images through the PDLC window were used to determine the contrast of the images. Each image was captured with the PDLC film at a specific level of visible optical transmission.

Contrast calculation was depended on the root mean square (RMS) contrast method [152] as demonstrated in equations (5. 1) and (5. 2):

$$RMS\ Contrast = \sqrt{\frac{1}{M * N} \sum_{i=0}^{M-1} \sum_{j=0}^{N-1} (I_{ij} - \bar{I})^2} \qquad (5.\ 1)$$

Where:

M and N are the number of columns and rows of the image I, respectively

I_{ij} is the pixel's value which is located in the i^{th} column and the j^{th} row, and $\bar{I}$ is the mean value of the brightness of overall pixels in the image I. However, the mean brightness can be determined using equation (5. 2) in the range of [0, 1]:

$$\bar{I} = \frac{1}{M * N} \sum_{i=0}^{(M*N)-1} I_i \qquad (5.\ 2)$$

2- A mathematical model: a computational formula for calculating the necessary voltage to bias the PDLC film. Based on the user's selected preferred vision ratio (PVR), this will keep a specific level of optical visual transmission.

As seen in **Figure 5. 1**, the contrast values that the image processing model produced are plotted versus the associated voltage. Ac voltage levels were used to draw the contrast values of 0, 10, 20, 30, 40, 50, 60, 70, 80, 90, 100, 120, 140, 160, 180, and 200 volts, as shown in the figure. The key points on the defined curve are as follows:

- C_{min} and C_{max} are, respectively, the lowest and highest contrast values.
- (v_{th}, C_{th}) is the contrast threshold point, where C_{th} is the contrast value that must be exceeded before contrast values begin to saturate, and v_{th} is the appropriate voltage at threshold contrast. Equation (5. 3) was used to determine the threshold contrast value:

$$Threshold\ Contrast\ (C_{th}) = 0.707\ (C_{max} - C_{min}) \qquad (5.\ 3)$$

On the contrast curve, the two points (C_a, v_a) and (C_b, v_b), which are situated before and after the desired point (C_{pvr}, v_{pvr}) on the contrast curve, must be identified in order to find the voltage (v_{PVR}) for the PDLC film that offers the desired visible optical transmission. Based on the user-specified preferred vision ratio (PVR), the quantification process should monitor the point (C_{pvr}, v_{pvr}). The minimum value of (PVR) is 0 (which indicates the minimum visibility permitted via the window), and the highest value of (PVR) is 1 (which provides the highest offered visibility via the window). However, equation (5. 4) was used to estimate the instant value of the preferred voltage for the PDLC film (v_{PVR}):

$$v_{PVR} = v_b - \left[(v_b - v_a)\left(\frac{C_b - (PVR(C_{max} - C_{th}) + C_{th})}{C_b - C_a}\right)\right] \ldots\ldots 0 \leq PVR < 1 \qquad (5.\ 4)$$

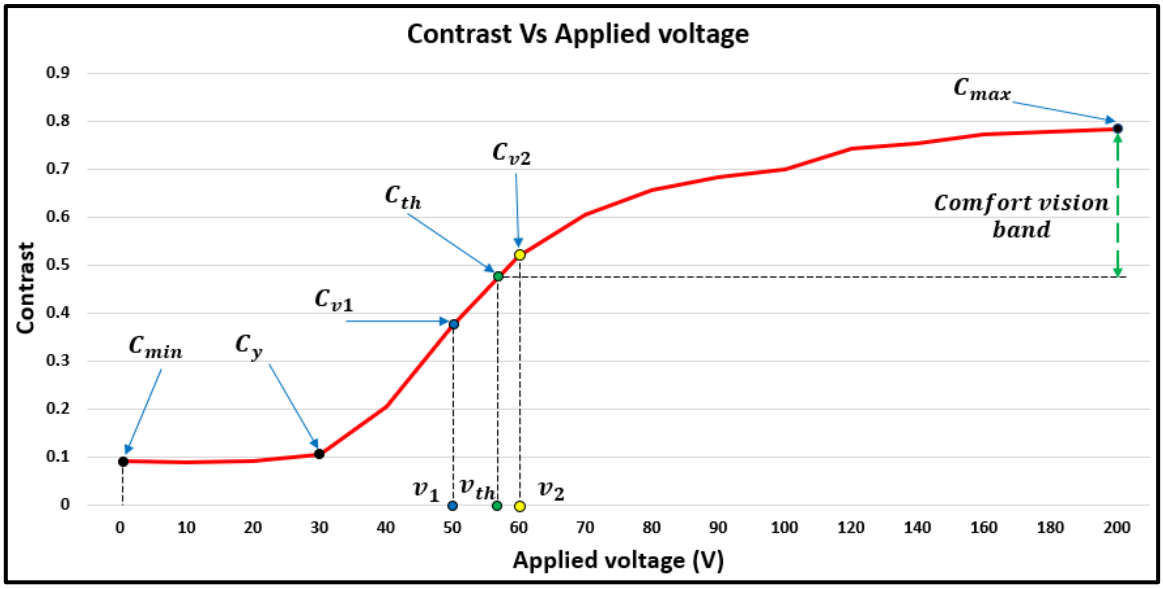

Figure 5. 1. *Contrast of the scene through the window versus the applied voltage.*

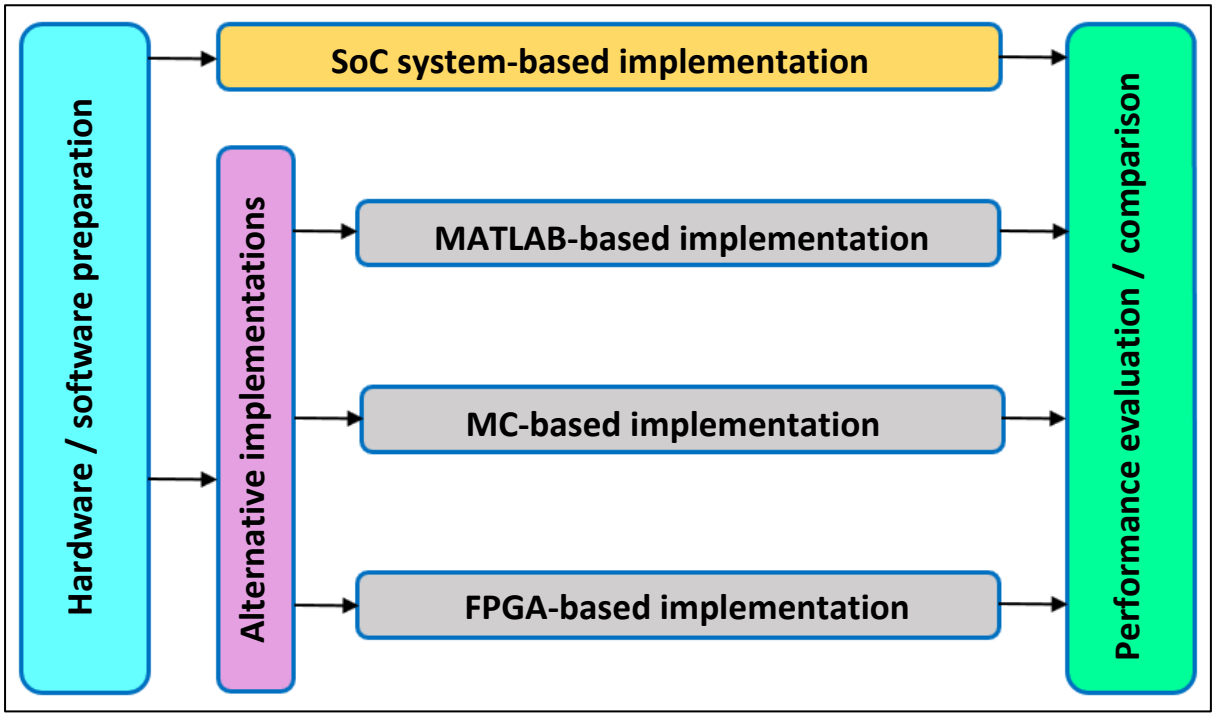

Figure 5. 2. *Workflow of automated vision quantification controller implementation.*

The workflow depicted in **Figure 5. 2** is the foundation for the work in this chapter. To carry out the quantification action, the necessary hardware and software were ready. The quantification algorithm was implemented using a system on-chip (SoC) system; it will be discussed in more detail in the following sections. On the other hand, three alternate approaches based on MATLAB, microcontrollers, and field programmable gate array

techniques were used to implement the quantification process. Finally, a thorough evaluation and comparison of the realized systems' performance was conducted.

Figure 5. 3 depicts the proposed quantification algorithm. According to chapter four, the quantification algorithm has several stages, including image capture, contrast computation, PDLC voltage estimation, and repetition time counting. The experimental work in chapter four, in contrast, carries out various steps manually. The previous chapter, however, did not depict the entire proposed algorithm in a single diagram to demonstrate how the system might operate to accomplish it. Additionally, the repetition time step was not included in the earlier work. As a result, the repetition time stage was added to the previously mentioned quantification process components in the current chapter, as shown in **Figure 5. 3**. The algorithm begins by storing the current time (t_1) because the entire procedure must be carried out within a specific time (T_r) on a regular basis. Thereafter a collection of photos ought to be captured and kept in a storage location. A PDLC power driver is given instructions by the main controller to produce the previously mentioned first voltage level (0 volt). A high-definition HD camera captures a single image via the PDLC window after the ordered voltage has been set, and it is then saved in a memory storage device. The camera will take another picture through the window after the controller commands the power driver to produce the subsequent voltage level. For the remaining images, the process is repeated. The sixteen images, each of which is captured at a specific voltage level, should then be saved in the system's memory.

The calculation of contrast is done in the subsequent step of the process. The individual saved images must be brought to the RAM so that the controller can reach and use them. In accordance with equations (5. 1) and (5. 2), the controller derives the RGB data from the images and calculates the contrast value. The system then finds all sixteen (contrast vs. voltage) points on the contrast curve, as formerly described in **Figure 5. 1**, after image processing carrying out has been completed.

The next pace is to find, based on the selected PVR ratio, the necessary voltage to operate the PDLC film and retain the desired transparency. In order to calculate the equivalent voltage, the controller initially defines the landmark points on the contrast slope using equations (5. 3) and (5. 4) respectively. The controller then calculates the voltage value, which

is then transmitted to the PDLC power driver. The voltage level may be formed as a binary-code that represents the recommended voltage value calculated by equation (5. 4). It will be decoded by the power driver, which will also produce the required voltage for the PDLC film. Eventually, it's critical to note the time that has passed since the first step ($elapsed\ time = t_2 - t_1$). The system then concludes to delay rerunning the quantification algorithm until ($T_r - elapsed\ time$) has finished the entire cycle (T_r).

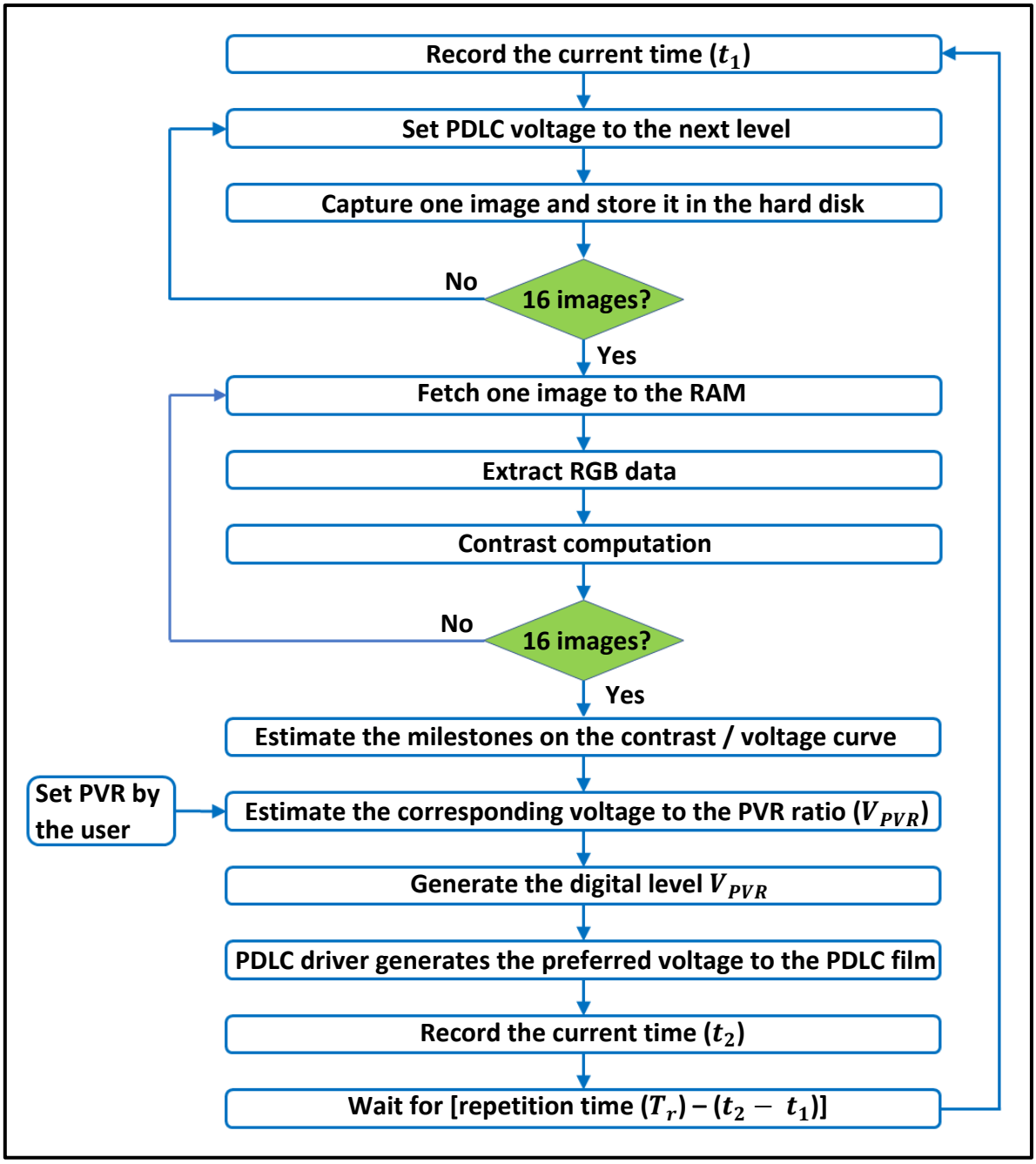

Figure 5. 3. The proposed quantification algorithm.

5.3 Experimental setup

The circuitry for the quantification process controller was realized through an experiment with four scenarios. The experimental scenarios, which include their goal, architecture, hardware configuration, and software organisation, are illustrated in the following.

5.3.1 Scenario one: implementation of vision quantification controller using on-chip SoC system

The quantification procedure shown in **Figure 5. 3** was implemented using a SoC-based system called the Raspberry Pi-3 (RPi-3). As a result, the hardware and software were set up as depicted in **Table 5. 1**. The open source SoC system is provided by the Raspberry Pi-3 board [156], which is run by Linux. The SoC system translated the quantification algorithm shown in **Figure 5. 3** into a Python program. To implement the suggested process, the Python program manages the auxiliary devices. An HD camera that was suited with the SoC system was used to capture the images. The SoC system selects a 10-bit digital code as the voltage value. In other words, there are ($2^{10}\ or\ 1024$) levels in the PDLC AC voltage range. An ATmega328P-based microcontroller acquires the digital code (decided by the SoC) on the Arduino board. Based on the obtained decision, the Arduino microcontroller is in charge of producing a pulse width modulated (PWM) signal. The power driver receives the PWM signal, which is then used to create the desired voltage value for the PDLC film. The SoC system's operating system was observed on a PC. **Figure 5. 4** shows how scenario 1 is set up.

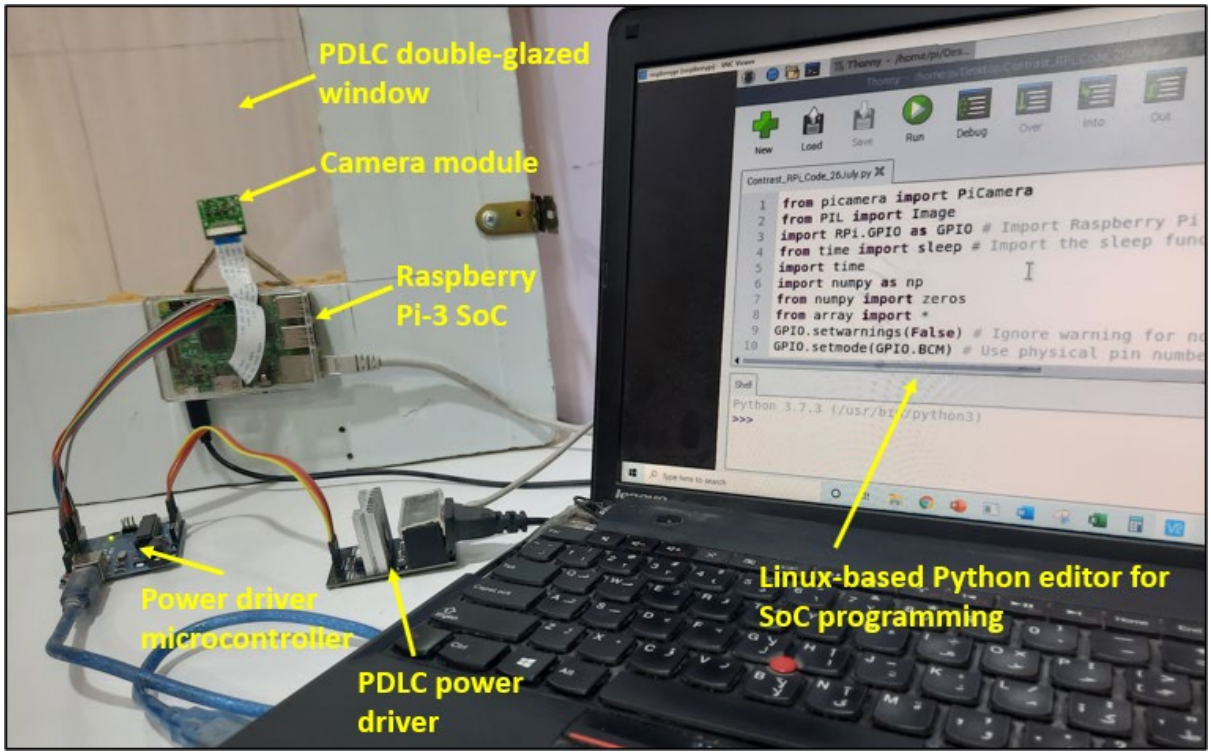

Figure 5. 4. *Scenario one: experimental setup.*

The wiring diagram of Raspberry Pi-3 SoC system is shown in **Figure 5. 5**. A windows-based personal computer (PC) acts as a workstation to monitor, control, and program the Raspberry Pi-3 SoC system. The camera module is interfaced to the SoC system to send the taken images. On the other hand, the SoC system sends the binary code corresponding to the preferred voltage to an Arduino microcontroller. The latter microcontroller is responsible for adjusting the duty cycle of the pulse width modulated signal and sending it to the AC power driver; the power driver generates the desired AC voltage for the PDLC film accordingly.

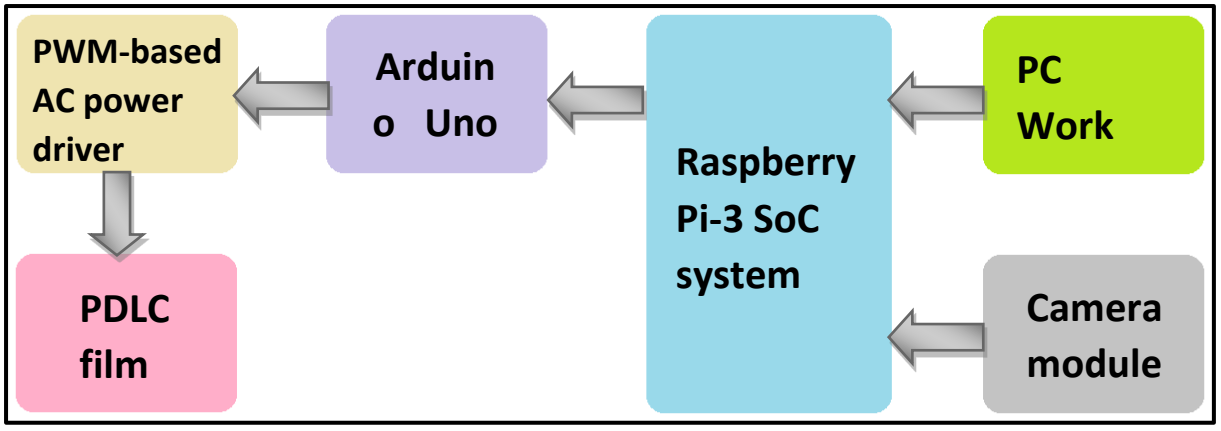

Figure 5. 5. *Wiring diagram of Raspberry_based SoC system.*

5.3.2 Scenario two: implementation of contrast estimator using MATLAB

In this case, only the contrast estimation portion of the suggested quantification process will be implemented using MATLAB code. The image's RGB data is first read by the code, and each image's contrast is then calculated separately. More information about the hardware and software configuration of scenario two is shown in **Table 5. 1**.

5.3.3 Scenario three: implementation of contrast estimator using Microcontroller system

In this case, the contrast estimation component of the identified quantification algorithm has been realized using an ARM Cortex-A9 microcontroller. Integrated into the microcontroller is an Altera Cyclone V FPGA chip. A bare-metal bus [157] connects the microcontroller to a client (a personal computer). On the client side, the ARM Development Studio IDE software acts as a mediator for the programming code and the microcontroller. To carry out the contrast computation action, a piece of code was created using the open-source "C" programming language. More information about the setup of scenario 3 can be found in **Figure 5. 6** as well as in **Table 5. 1**.

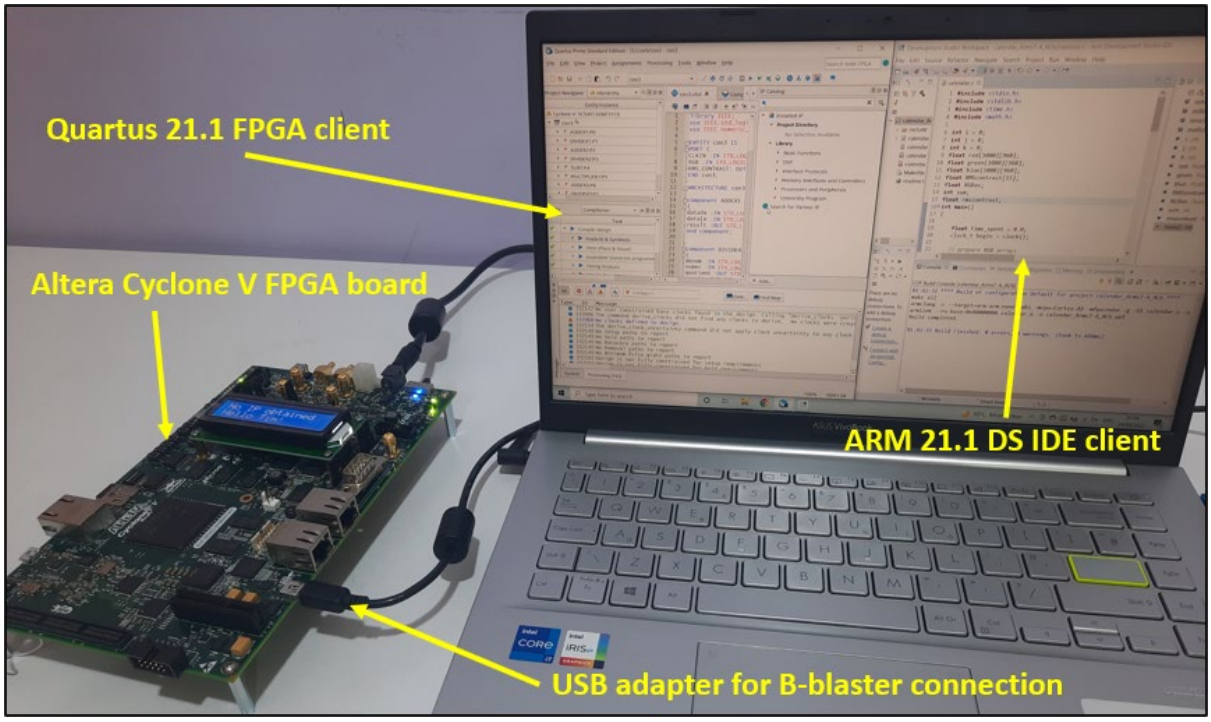

Figure 5. 6. *Experimental setup for scenario 3 and 4.*

5.3.4 Scenario four: implementation of contrast estimator using field programmable gate array chip

In case four, the contrast estimation circuit was constructed using the field programmable gate array chip. The contrast estimator was built using the 41,910 CLBs or configurable logic blocks from Altera Cyclone V. The Quartus software controls the FPGA design [158].

The FPGA chip prototyped the estimation circuit depicted in **Figure 5. 7** to calculate the contrast value for a single image with the timing diagram. The system depends on the contrast calculation formulas (5. 1) and (5. 2). The design made use of the intellectual properties components (IPs) in the Quartus software library to build the circuit. Very high scale integrated circuit Hardware Description Language (VHDL) [159] was used to describe the estimator circuit's top-level design. **Figure 5. 7** shows the thorough timing diagram. Initially, the output of each component in the circuit is reset to zero to begin the contrast estimation process.

The divider (DIV1) component divides the sum value by three times the count of pixels ($3MN$) after the accumulator (ACC1) has calculated the equation (5. 2) ($\bar{I} = \frac{1}{M*N}\sum_{i=0}^{(M*N)-1} I_i$)'s result. At this point, the input image's I average brightness $\bar{I}$ has been calculated. Additionally to one clock cycle for the division action, this step needs ($3MN$) clock cycles to compile the RGB data for entire pixels. The accumulators components ACC2 and ACC3, the divider components DIV2, the subtractor component SUB, and the multiplier component all work together to determine the term ($\sum_{i=0}^{M-1}\sum_{j=0}^{N-1}(I_{ij} - \bar{I})^2$) in equation (5. 1).

The average brightness of a pixel (I_{ij}) is calculated for each pixel by adding the RGB data for that pixel (by the accumulator ACC2), and then dividing the result by three (by the divider DIV2). The subtractor subtracts the current pixel's average brightness I_{ij} from the mean brightness of all the pixels ($\bar{I}$). (SUB). The multiplier squares the calculated difference of pixel's brightness under processing (by the multiplier component MUL). The accumulator builds up the squared difference $(I_{ij} - \bar{I})^2$ for each pixel (by the accumulator ACC3). This process uses up ($8MN$) clock cycles because it needs eight clock cycles to complete one pixel. The divider (DIV3) divides the result of accumulation (the output of the accumulator component ACC3) by the count of pixels ($M * N$).

The output of the divider (DIV3) is fed to the square root circuit (SQRT) to determine the RMS contrast value according to equation (5. 1). It is assumed that each component in the FPGA design is supplied by a unique clock signal. The clock signals are generated by the clock distribution circuit shown in the figure. The clock signals activate the components of the FPGA circuit at specific times to complete the mathematical operations of equations (5. 1) and (5. 2). In the timing graph of **Figure 5. 7**, the number of utilised clocks were displayed for various phases with regard to column M and row N of the image. The clock source on the FPGA chip sends a universal clock signal to the clock distribution circuit.

Clock distribution circuit in **Figure 5. 7** receives the main clock signal and spreads the timing signals to other entities. However, this task requires a special circuit, **Figure 5. 8** and **Figure 5. 9** show the entire design of the clock distribution circuit. In **Figure 5. 7**, contrast calculation for one image passes through six intervals; the number of clock cycles required by each interval is: one cycle, 3MN cycles, one cycle, 8MN cycles, one cycle, and one cycle, respectively. **Table 5. 2** identifies the start and end points for each interval in terms of the number of clock cycles.

Table 5. 1. *Setup of the experimental scenarios.*

Scenario	Item	Specifications	
1	**Raspberry Pi-3 SoC-system**	CPU	ARM Quad-core Cortex A-53 (1.5 GHz)
		RAM	DDR2 SDRAM (1 GB capacity)
		Hard disk	External SD memory (16 GB capacity)
		Operating system	Linux-OS
		Programming language	Python-3
	HD camera	Module	Raspberry Pi-3 (5 Megapixel) camera
		Resolution	Up to 2592 x 1944 pixels
	Power driver	Module	Triac PWM-based AC dimmer
		Rating	16 A, 600 V AC
		Microcontroller	Arduino-UNO (ATmega328P MC)
2	**Software**	MATLAB WINDOWS-based (version 2022)	
	Programming language	MATLAB programming language	
	Operating system	WINDOWS 10 (64-bit)	
	PC	Intel quad-Core i7, 2.2 GHz speed, 8 GB RAM capacity	
3	**Microcontroller**	ARM Cortex-A9 MC, Dual-core, (50 MHz speed)	
	Software	ARM Development Studio IDE 2022.1	
	Programming language	“C”	
4	**FPGA chip**	Altera Cyclone-V	
	Software	Lite Edition of Quartus Prime 21.1	
	Programming language	VHDL	

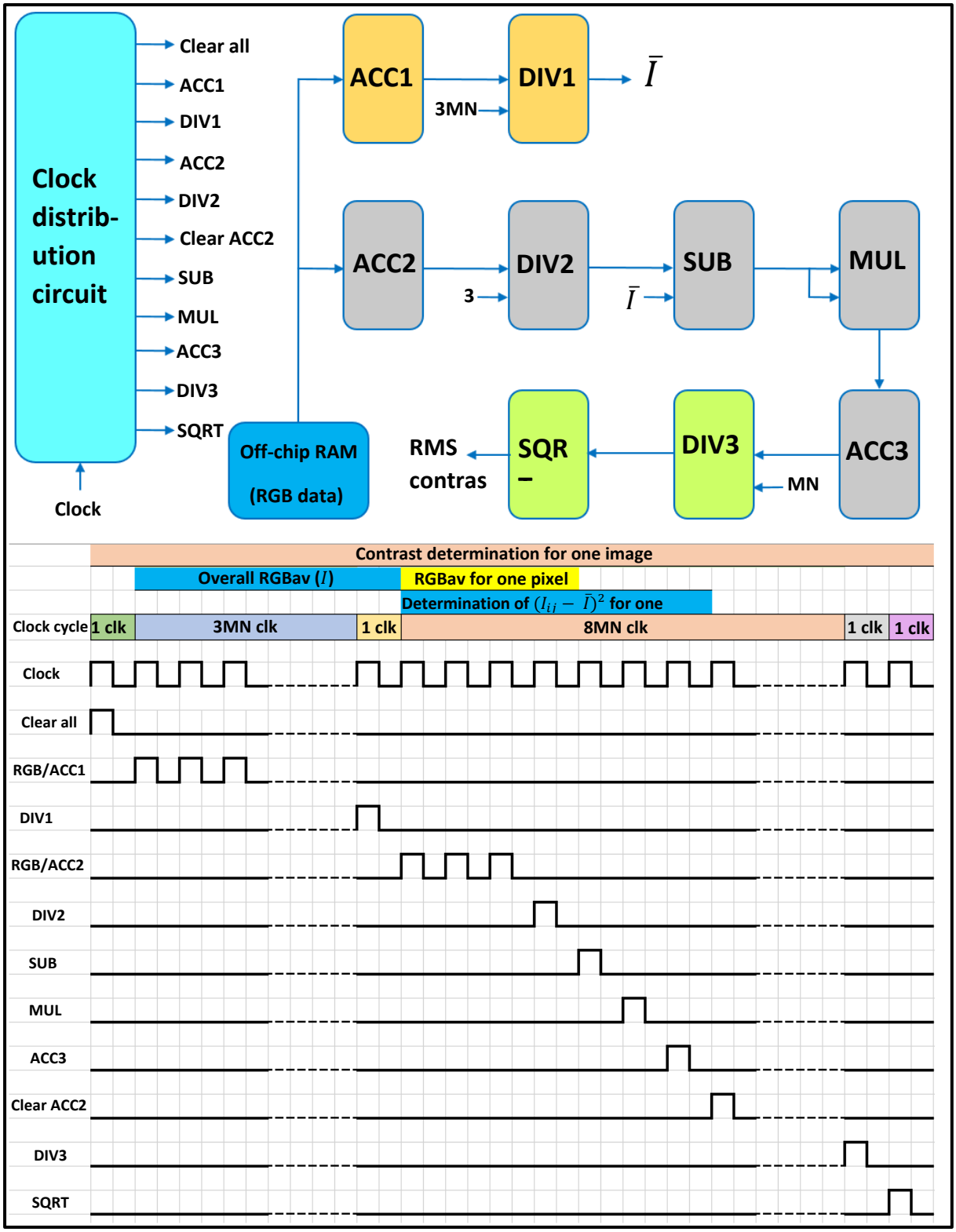

Figure 5. 7. *Estimator circuit design and the timing diagram using Alter Cyclone-V FPGA chip.*

Table 5. 2. *Intervals of contrast calculation.*

Interval	No. of clock cycles	Starts at clock No.			Ends at clock No.		
		Decimal	Binary	Point in the figure	Decimal	Binary	Point in the figure
1st	1	0	000000000000000000000000	A	1	000000000000000000000001	B
2nd	3MN	1	000000000000000000000001	B	3110401	001011110111011000000001	C
3rd	1	3110401	001011110111011000000001	C	3110402	001011110111011000000010	D
4th	8MN	3110402	001011110111011000000010	D	11404802	101011100000011000000010	E
5th	1	11404802	101011100000011000000010	E	11404803	101011100000011000000011	F
6th	1	11404803	101011100000011000000011	F	11404804	000000000000000000000000	G ≡ A

If the images to be used in the experiment are (MN = 1080 x 960 pixels), then the total count of clock cycles needed to complete the contrast calculation for a single image is (11MN + 4 = 11404804 clock cycles, or 1010 1110 0000 0110 0000 0100 in binary). Hence, to determine this interval, a 24-bit digital counter with a clear input is employed. to clear the output at the (11404804th counting stage), a 24-input AND gate is used to generate a reset pulse at the (11404804th input clock cycle) as shown in **Figure 5. 8.** Clock distribution circuit (A). Therefore, inputs of the AND gate with logic "0" are inverted by the NOT gate according to the (1010 1110 0000 0110 0000 0100) binary input (reset cycle); the output of the AND gate is fed to the clear input of the counter (CLR).

The points "A, B, …, G" represent the start and end points of the six intervals as illustrated in **Table 5. 2**. The AND gates (1 to 6) are used to generate positive pulses (high edges) at the points (A to F) respectively. It is worth mentioning here that the point (G) represents the end point of the sixth interval and occurs at the same timing of point (A); i.e., (G ≡ A). For instance, all inputs of AND gate number (1) are complemented; hence, a positive pulse is generated at the beginning of the first interval (first counting stage (0000 0000 0000 0000 0000 0000) or point A). Further, all inputs of AND gate number (2) are complemented except the first least significant bit (O0); therefore, a positive pulse is generated at the end of the first interval (second counting stage (0000 0000 0000 0000 0000 0001) or point B).

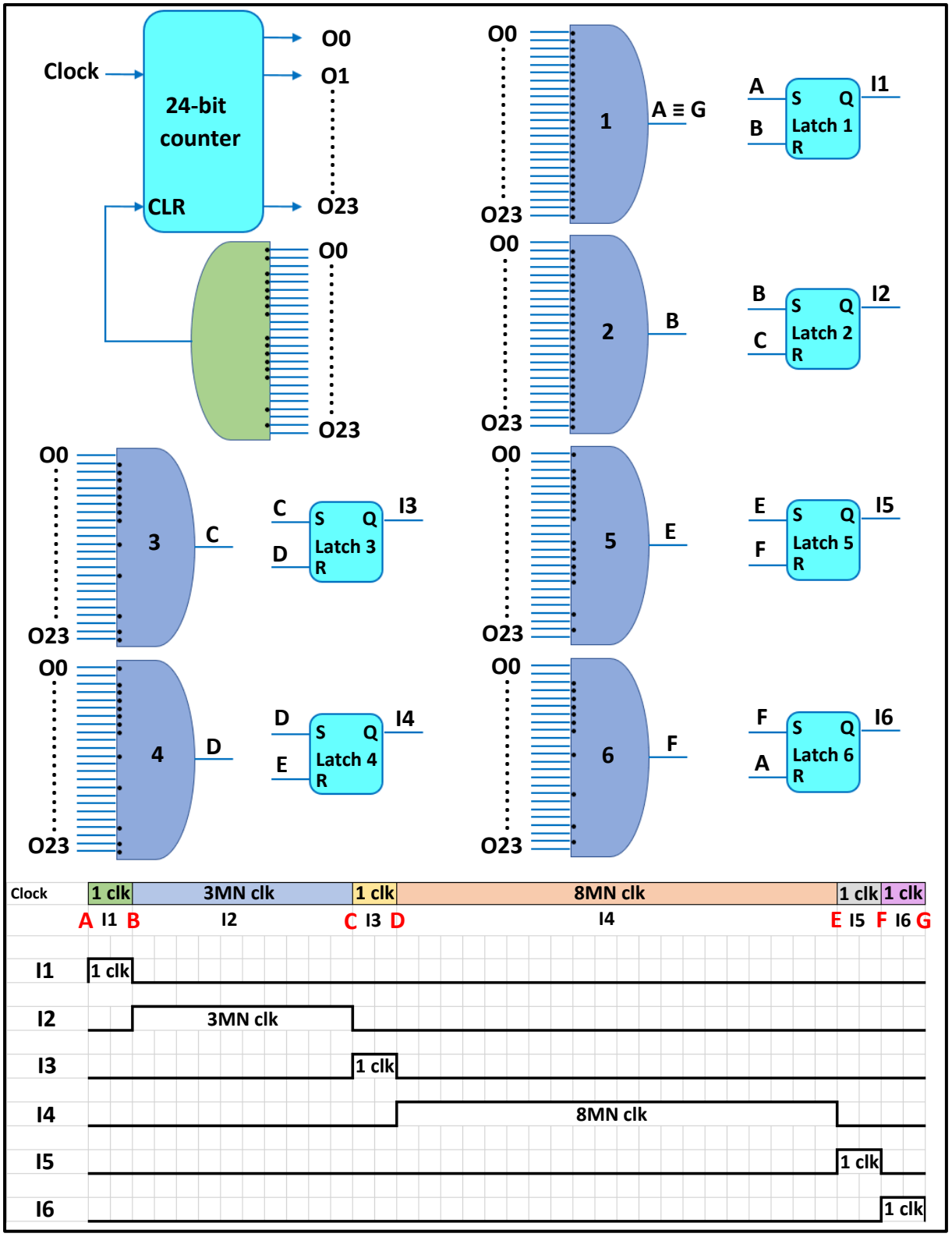

Figure 5. 8. *Clock distribution circuit (A).*

The start pulse (A) and the end pulse (B) of the first interval are wired to the set and reset inputs of (latch 1) respectively. Consequently, the output signal (I1) of (latch 1) will be logic high only during the first interval, as depicted in **Figure 5. 8**. In the same manner, using the

ANG gates (2 to 6) and the latches (2 to 6), signals (I2 to I6) can be generated to be logic high during the intervals (2nd to the 6th) respectively.

Figure 5. 9 shows the second part of the clock distribution circuit; it receives the signals (I1 to I6) to generate the timing signals for the entities of the contrast estimation circuit. However, before going through the details of the design, the following explanation demonstrates the sequence of the timing signal in the contrast estimation circuit.

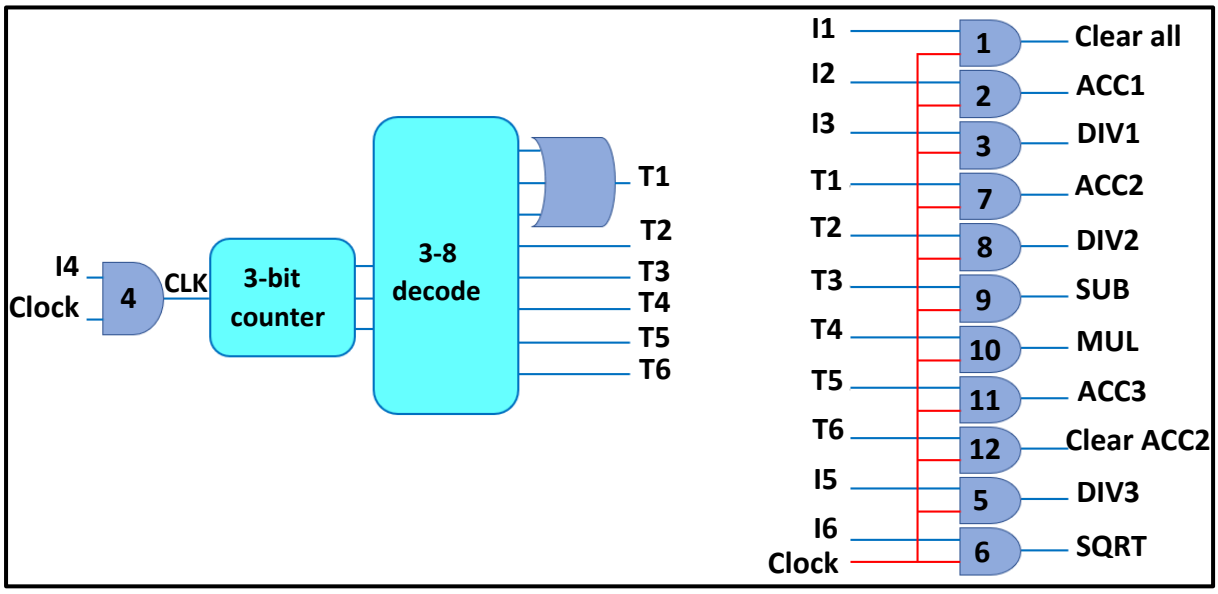

Figure 5. 9. *Clock distribution circuit (B).*

The required sequence of timing signals is shown in **Figure 5. 10** as follow:

1- During the first interval, the sequence starts with (Clear all) signal for only one clock cycle.
2- In the second interval, (ACC1) signal is repeated MN times.
3- The third interval has (DIV1) signal with only one clock cycle.
4- In the fourth interval, the following sequence is occurred MN times:
    a. signal (ACC2) has three clock cycles.
    b. The signals (DIV2), (SUB), (MUL), (ACC3), and (Clear ACC2) has only one clock cycle respectively.
5- During the fifth and sixth intervals, (DIV3) and (SQRT) signals have only one clock cycle, respectively.

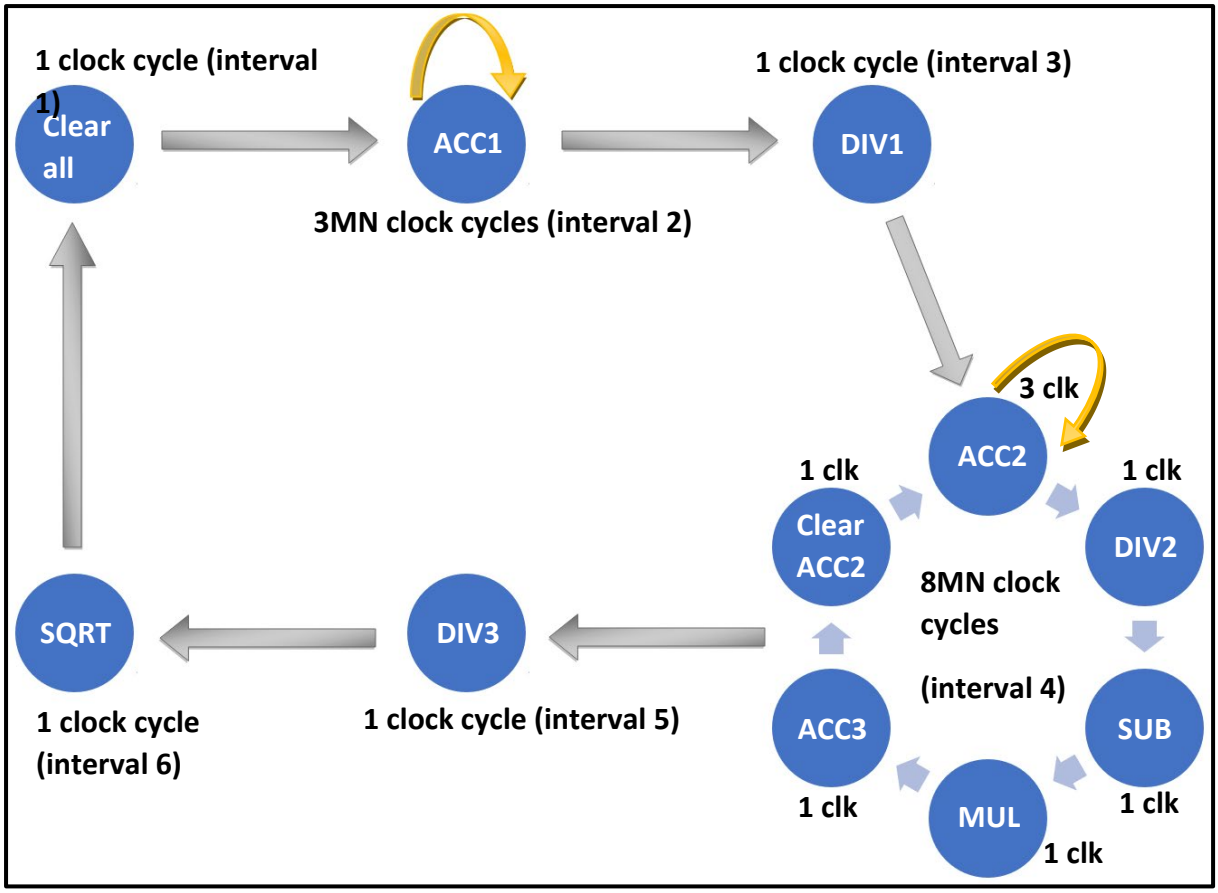

Figure 5. 10. *Sequence of timing signals.*

Referring to **Figure 5. 9**, the signals (I1 to I6 and T1 to T6) are wired to the first input of 2-input AND gates (1 to 12) respectively, while the second input of the AND gates (1 to 12) is fed by the main clock signal. Therefore, AND gates allow the clock signal to appear at their outputs while the first input (one of the signals: I1 to I6 and T1 to T6)) is active or logic high. In this way, the timing signals of the contrast estimation circuit are obtained as follows:

1- (Clear all, ACC1, DIV1, DIV3, and SQRT) signals can be generated by ANDing (I1, I2, I3, I5, and I6) with the main clock signal respectively.
2- (I4) signal is used to activate a 3-bit digital counter during the fourth interval. The 3-bit output of the counter is interfaced with the 3-8 decoder. Six signals will be generated as below:
    a. (T1) is logic high during the first three counting stage of the counter.
    b. (T2 to T6) is logic high during the (fourth to eighth) counting stage of the counter.

3- (ACC2, DIV2, SUB, MUL, DIV3, and Clear ACC2) signals can be generated by ANDing (T1 to T6) with the main clock signal, respectively.

5.4 Results of implementing the vision quantification controller and discussion

The following are the section's goals:

1. showcasing and contrasting the experimental outcomes of the scenarios that were put into practice and listed in Table 5.
2. looking into the cost, power consumption, throughput, latency, and processing speed of the realized systems.

The SoC system was connected to the Raspberry camera, which was then firmly fastened in front of the window. The PDLC film was connected to the power driver's output, which was interfaced with the SoC system. **Figure 5. 11** illustrates the investigation done prior to running the Python code to determine how long it took the SoC system to take one image. It is important to be aware of this time because it should be included in the system's overall latency calculation as a delay. The steps that were taken to determine the duration of each step were as follows:

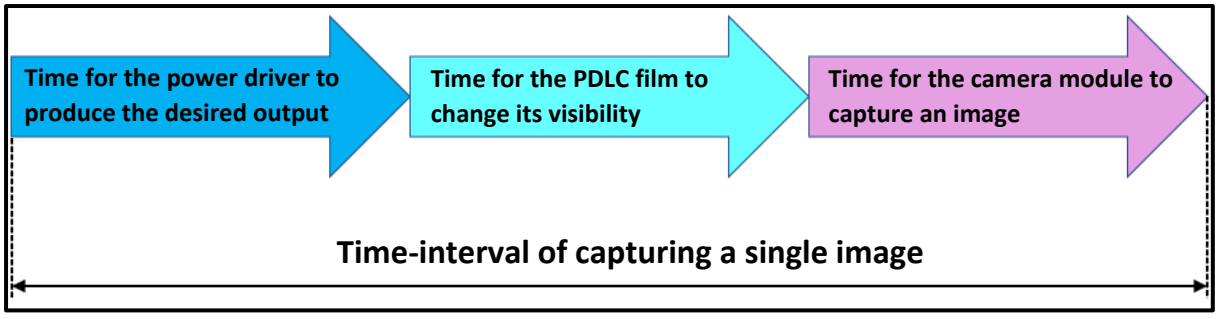

Figure 5. 11. *Time-interval of capturing a single image.*

1- The SoC system creates the binary-code that represents the necessary voltage level and transmits it to the power driver in order to capture one image. The power driver requires some time to sets its output to the desired level. To test the power driver's time response, a different experiment was run. A suitably calibrated ac voltage sensor was set up to monitor the power driver's output. The power driver was demanded to produce a 50 volt

output while the output was at 20 volts (20 V and 50 V were assigned at random); the power driver response is depicted in Figure 5. 8. The output was jump-started to 50 V in 20 milliseconds, according to the time response.

2- On previous research examination on this subject, it can be relied upon to determine the time needed by the PDLC film to change its optical state versus the variation of input voltage. According to Pozhidaev et al. [160], a PDLC film transitions from an opaque state to a translucent state in about 10 msec.

3- In a separate experiment, a Python code was created to examine how long the camera module needed to shoot a single image. The same SoC system and camera module that used in the main experimental scenarios were applied. The examination revealed that the camera takes one image in 531 milliseconds. This time, an image is captured and stored in a specific directory in the SoC system's memory.

As a result, it can be claimed that the SoC system needed 561 ms (20 ms + 10 ms + 531 ms) to take a single picture, or about 8.98 sec for 16 images. In addition to the latency caused by the other actions of the suggested quantification algorithm, this time will also be regarded as a latency.

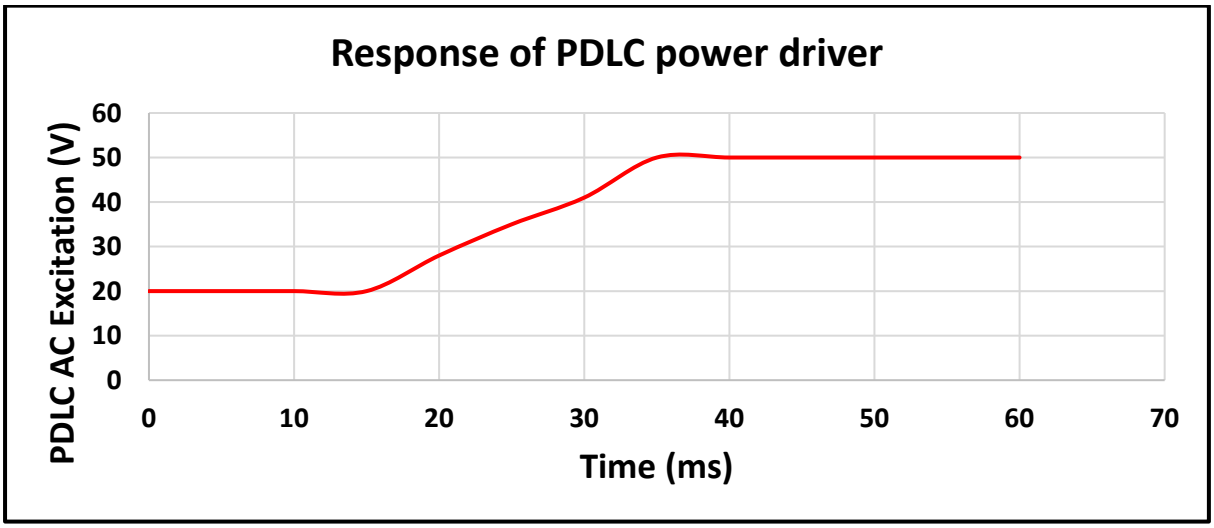

Figure 5. 12. *Time response of PDLC power driver.*

The SoC system carried out the quantification process after executing the Python code for scenario one, taking and storing sixteen (1080 x 960) images. Both in this scenario and the other scenarios, the estimation of contrast estimation was done for the image group. The

desired voltage level was produced by applying the calculated contrast values to the mathematical model of the proposed quantification algorithm. A random number was chosen for the PVR ratio. Finally, the power driver applied the desired voltage to the PDLC film in accordance with the SoC choice. According to the capacity of the input data and the latency, the throughput of the experimental systems can be estimated.

$$Throughput\ of\ vision\ quantification\ SoC\ system = \frac{Data\ size}{Latency}\ (bit\ per\ sec) \qquad (5.\ 5)$$

The 16 images serve as the input data for all scenarios of the experiment. The implemented systems in the experimental scenarios work with the images' RGB data. Therefore:

$$Input\ data\ size = 3KMN\ (bit) \qquad (5.\ 6)$$

Where K is the number of bits per single colour data, in this case $K = 8$ as the input images are 8-bit coloured images, and M and N are the column and row numbers of image pixels, respectively.

The Python code was properly established to track how much time was spent on each step as the program ran, and the results were as follows:

- Time spent for capturing and saving 16 images in SoC memory = 8.98 seconds.
- Time to fetch images from the hard-disk of SoC system to the RAM = 0.12 seconds.
- Time spent for contrast estimation time = 451.69 seconds.
- Time spent to estimate voltage values for the power driver = 0.02 seconds.
- Throughput of the SoC systems is approximately 0.86 Mb/second.

In accordance with the second scenario, a Windows-based PC's hard drive contained the sixteen photos that the camera module in scenario one had captured. The MATLAB code correctly sets the image group's location so that the program can reach them while it is running. During execution, the MATLAB software made use of two CPU cores from the PC's processing power. To gauge the running time for the contrast computation part, the "TIC-TOC" instruction was used in the code for this purpose. The results showed that the time

spent to calculate the images' contrast values is 2.98 seconds. The system's throughput was measured at 133.6 Mb/s.

According to scenario three, the ARM A9 microcontroller system was used to compute contrast using the images captured in the first scenario. The "C" code for the program included a reference to the storage directory where the stored images were kept. Instructions to determine the amount of time needed to calculate contrast were also included in the code. The ARM development studio IDE software (at the PC side) in addition to the on-chip CPUs started a blaster link over a USB port (on the Cyclone V FPGA board). A "C" compiler was used to compile the code and create the source code that the microcontroller would use to run it. When the code was run, it was discovered that the contrast estimation task took 8.36 seconds. 47.62 Mb/sec of throughput was actually measured.

In accordance with the fourth scenario, Quartus prime software generated an empty FPGA Cyclone-V chip-based project. VHDL language was used to define the hardware configuration of the logical circuit in **Figure 5. 7**. To realize the circuit, intellectual properties (Ips) were restored from the Quartus software library. As a top-level design, a VHDL code was created that contains a thorough description of the wiring layout among the various components in the circuit. Since it is situated outside the FPGA chip, the off-chip memory in **Figure 5. 7** was not included in the FPGA design. The 16 images gathered in scenario 1 are stored in the RAM as RGB data. A "Cyclone V FPGA board" contains the FPGA chip and the off-chip memory represented by an (SD RAM). After compiling the project, the following information regarding the use of hardware resources was taken from the Quartus software:

- Number of the utilised Configurable Logic Blocks (CLB): 2493 out of 41910 (≈ 6%).
- Number of the utilised Digital Signal Processing Blocks (DSPB): 3 out of 112 (≈ 3%).
- The Frequency of the universal clock source: on-chip clock source (50 MHz).

Using **Figure 5. 7**'s timing diagram for the FPGA design, the count of clock cycles required to compute a single image's contrast is:

$$Clock\ cycles\ for\ Contrast\ computation = (11MN + 4)\ clock\ cycle \qquad (5.\ 7)$$

Where M and N are column number and row number of image pixels respectively. Thus, the latency of the FPGA contrast estimator is:

$$Latency\ of\ FPGA\ contrst\ estimator = \frac{11MN + 4}{F_{CLK}} \quad (5.\ 8)$$

The circuit used 50 MHz (or 0.02 sec cycle time) and the captured images in all scenarios have a resolution of (1080 x 960) pixels, so the FPGA contrast estimator's latency is (0.228 sec). The throughput is therefore (109.14 Mb/sec). **Table 5. 3** lists the outcomes of the scenarios that were put into practice, though.

Table 5. 3. *Results summary.*

Method of implementation	**For sixteen images**			**For one image**
	R-Pi 3 SoC system	**MATLAB**	**Cortex-A9 MC**	**FPGA**
Contrast computation (s)	451.69	2.98	8.36	0.228
Throughput (Mb/s)	0.86	133.6	47.62	109.14
Additional result	Time for remaining steps of the process = 9.12 s	. . . . .	. . . . .	Configurable logic block utilisation (6 %) DSP block utilisation (3 %)

The realized systems of the experimental scenarios will be evaluated and compared in the next sections based on the outcomes. The advantages and disadvantages of each system will be outlined from a variety of points of view.

5.4.1 Latency

According to the experimental data from the Raspberry Pi-3 SoC system, the time it took to determine the contrast was 451.69 seconds. In other words, it was responsible for 98% of the program's overall latency. The monitored running time for the entire process is 7.68 minutes; but, when the preferred repetition time (T_r) of the quantification process is less than it (7.68 minutes), this latency will not satisfy the real-life application need. Therefore, a different approach should be taken into account to shorten the running time of the vision quantification process. The realized "contrast estimator systems" in the other scenarios will

be checked to address this problem because the phase of contrast estimation caused the effective delay.

2.98 seconds of latency were effectively reduced by the MATLAB implementation method. As a result, the quantification process will be completed faster than the Raspberry Pi-3 SoC system ($T_r = 12.1$ seconds vs. $T_r = 460.81$ seconds). On the other hand, the bare-metal ARM Cortex-A9 realization performs efficiently. In comparison to the Raspberry Pi-3 SoC system, the latency was reduced to 3.8%. As a result, the quantification process takes less time, or ($T_r = 17.48$ seconds). In FPGA implementation, the contrast estimation was reduced to 0.228 seconds in the fourth scenario; in other words, it is 1981 times higher processing speed than the SoC system in the first scenario. As seen in the FPGA contrast estimator, the lower latency system has a faster processing speed. In conclusion, The best performance was revealed by FPGA implementation among other methods in terms of latency.

5.4.2 Throughput

A system's latency is inversely correlated with its throughput. Therefore, throughput increases as latency decreases. For instance, the SoC system that was used had the highest latency and the lowest throughput of all the implemented systems, at 0.86 Mb/sec. By contrast, the FPGA implementation technique at low latency achieved a maximum throughput of 109.14 Mb/sec. However, the contrast computation is only accomplished for one image by the presented FPGA design. The potential use of the chip's residual resource to compute contrast for the sixteen images will be covered in the sections that follow. Therefore, the throughput and other FPGA circuit design parameters will be declared again later.

5.4.3 Power consumption

The experimental systems that are being presented can be divided into two categories in order to assess their power consumption. Computers in the two scenarios are the PC-based MATLAB system in scenario two and the Raspberry Pi-3 SoC system in scenario one. While the FPGA system and the ARM Cortex-A9 microcontroller are regarded as non-computers. Previous research revealed that Raspberry SoC systems consume less power than standard PCs. For example, Bekaroo and Santokhee [161]looked into the power usage of various computer types while they were carrying out a variety of tasks. They came to the conclusion

that the laptop uses 17.68 W, which is equivalent to four times the amount of power that a Raspberry SoC system uses. On the other hand, earlier research found that FPGA-based DSP implementations use less power than DSP micro-processors. For instance, using two different hardware platforms, a Texas Instruments DSP processor [162] and an Altera FPGA chip, Bai et al. [163] realised a DSP task and compared their power consumption. They came to the conclusion that the commercial DSP processor used 2.4 times more power than the FPGA-based system.

5.4.4 Cost

The expense of the proposed systems has a wide range of costs. The Raspberry Pi SoC systems, for example, are the most affordable at $35 [164]. Research findings have categorized FPGA techniques as low-cost DSP application implementation methods [165], [166]. However, the Altera cyclone V SoC development kit was used to implement the contrast estimator systems in scenarios three and four. The latter development kit is available from authorized organizations for $1795 [167]. The cost of MATLAB-based implementation will increase because it is necessary to use the hardware (the PC) and the licensed software permanently.

The permanent license for MATLAB, however, costs $2350, according to the official website [168]. Additionally, the price of a typical PC will be included with the implementation cost of MATLAB software. To conclude, the following order classifies the implementation methods from lower to higher in terms of cost: Raspberry Pi-3 system, Cyclone-V in scenarios three and four, and MATLAB implementation.

The SoC system of scenario 1 uses the ARM Cortex-A53 microcontroller, which has more advanced characteristics than the Cortex-A9 microcontroller that was utilised in scenario three. For example, the architecture of the A53 microcontroller has a quad-core CPU and a 64-bit data-bus, contrasts with the architecture of the A9 microcontroller, which has a dual-core CPU and a 32-bit data-bus [169], [170]. The results, however, demonstrated that the ARM A9 microcontroller outperformed the A53 MC in terms of contrast estimation process throughput and latency. CPU utilisation was tracked throughout the program's run in order to better understand how the A53 microcontroller behaved within the SoC system. It was

discovered that the Linux operating system used a single CPU to run the Python program, with the other cores being used to carry out other SoC system tasks. On the other hand, the ARM A9-microcontroller's entire resource pool was devoted to handling contrast estimation. Earlier research, however, highlighted that the Raspberry Pi-3 SoC system is not the best option for performing mathematical tasks [102].

According to earlier studies [171], [172], latency and power consumption in digital circuits are directly correlated to the count of clock cycles applied to the CMOS transistors gates. In order to estimate the count of clock cycles used in the proposed experimental systems, the latency and the frequency of the universal clock source (F_{CLK}) must be known . Subsequently:

$$Clock\ consumption\ in\ terms\ of\ clock\ cycles = Latency * F_{CLK} \quad (5.\ 9)$$

According to equation (5. 9) and the experimental findings, the contrast estimation in scenarios 1 through 4 took $691.2 * 10^9$, $6.56 * 10^9$, $418 * 10^6$, and $11.4 * 10^6$ clock cycles, respectively. In other words, latency and power consumption increase as clock consumption for a given digital function increases. Consequently, there is a greater decline in system performance when MATLAB, SoC, and ARM A9 MC implementations are used. Clock consumption strategy is a key distinction between FPGA implementation and other approaches. For the contrast computation action in experimental scenarios 1 to 3, a microcontroller or microprocessor was used. The mathematical method was translated into commands.

For the CPU to complete a single instruction, it needs one or more clock cycles. The number of clock cycles for the whole program will increase as a result. In contrast, the contrast estimator circuit was created using the configurable logic blocks (CLBs) that were present in the FPGA chip architecture. The summation loops in equations (5. 1) and (5. 2) needed $11.4 * 10^6$ clock cycles, which the FPGA circuit consumed. This resulted in the least amount of clock cycles being used, as well as the least amount of power consumption and latency [173].

The architecture of an FPGA chip admits it to configure itself according to the requested designs [174]. Additionally, after configuration, an FPGA chip gains hardware implementation features, i.e., the signals have fixed paths from the inputs to the outputs. In other words, the delay between input and output paths in FPGA chips [175], which is typically measured in

nanoseconds or even less, determines the delay of a system that has been implemented. The count of clocks needed to run an implemented process, as in PCs, microcontrollers, and SoC systems, determines the latency of software realisation techniques, which is typically higher than that of hardware implementation [102]. Therefore, as highlighted in the literature, FPGA is superior to other techniques for the realisation of image processing applications.

A human-like odour recognition algorithm was put into place by Mo, Z. et al. [176]. They made use of the FPGA technique, PCs with various processor types, and the Raspberry Pi-3 SoC system. The algorithm was run by the SoC system in 4.6 ms. The best case for PC-based realisation was 2.1 ms using an i7-10875H micro-processor. FPGA system, but, displayed an outstanding calculation efficiency with 57.3 µs. When applied to sophisticated computation algorithms, FPGA realisation is the most effective technique, according to the literature. The experimental results in this chapter are comparable to the efficiency variance between the FPGA and other realisation techniques in the literature. In comparison to the Raspberry Pi 3 SoC system, the suggested system's latency was reduced from 451.69 s to just 0.228 s in FPGA implementation.

In order to reduce latency even further, FPGA chips can implement a hardware acceleration technique. The hardware resources on the chip (configurable logic blocks and DSP blocks) are used by designers to construct a circuit using parallel paths. DSP applications use parallel designs to improve the efficiency of the mathematical operations [177]. This method can be used with the scenario 4 (the proposed FPGA circuit). According to the experimental outcomes, only 6% of the chip's area was used to construct the contrast estimator circuit for a single image. In order to build a contrast estimator circuit for sixteen images, the circuit may copied sixteen times to be working in parallel, making use of the residual unemployed resources on the FPGA chip. All circuits will receive the RGB colour data and triggering signals at once. As a result, the total latency will remain the same (0.228 sec), however, the throughput will increase by sixteen times (109.14 Gb/sec x 16 = 1.75 Gb/sec).

The presented FPGA circuit can be further parallelized. The circuit's effective percentage of latency was due to the two summations in equations (5. 1) and (5. 2). N accumulator and N divider are required if the summation ($\sum_{i=0}^{(M*N)-1} I_i$) is carried out in N parallel branches. As a result, the summation's latency will decrease by N times. In the same manner, the other

summation's latency can be decreased to lessen the overall time consumption. However, the used Altera Cyclone V FPGA chip's hardware resources (41,910 logic blocks) might not be sufficient to carry out this task. To occupy the extra components, an FPGA chip with more hardware resources should be used instead.

Figure 5. 13, which illustrates the behaviour of the proposed systems in the present chapter, provides a conclusion. High latency and power dissipation, along with humble computation efficiency, were displayed by the Raspberry Pi-3 SoC system. However, it can be selected due to its low cost if it can complete the quantification process equals to or less the repetition time (T_r). Implementation techniques using MATLAB and the Cortex-A9 MC demonstrated closed efficiency with minimal latency. Lowest latency and highest throughput are outstanding characteristics of the Cyclone V FPGA chip implementation. Additionally, the FPGA design enables the suggested vision quantification process to be implemented with a minimum repetition time ($T_r = 9.14\ sec$).

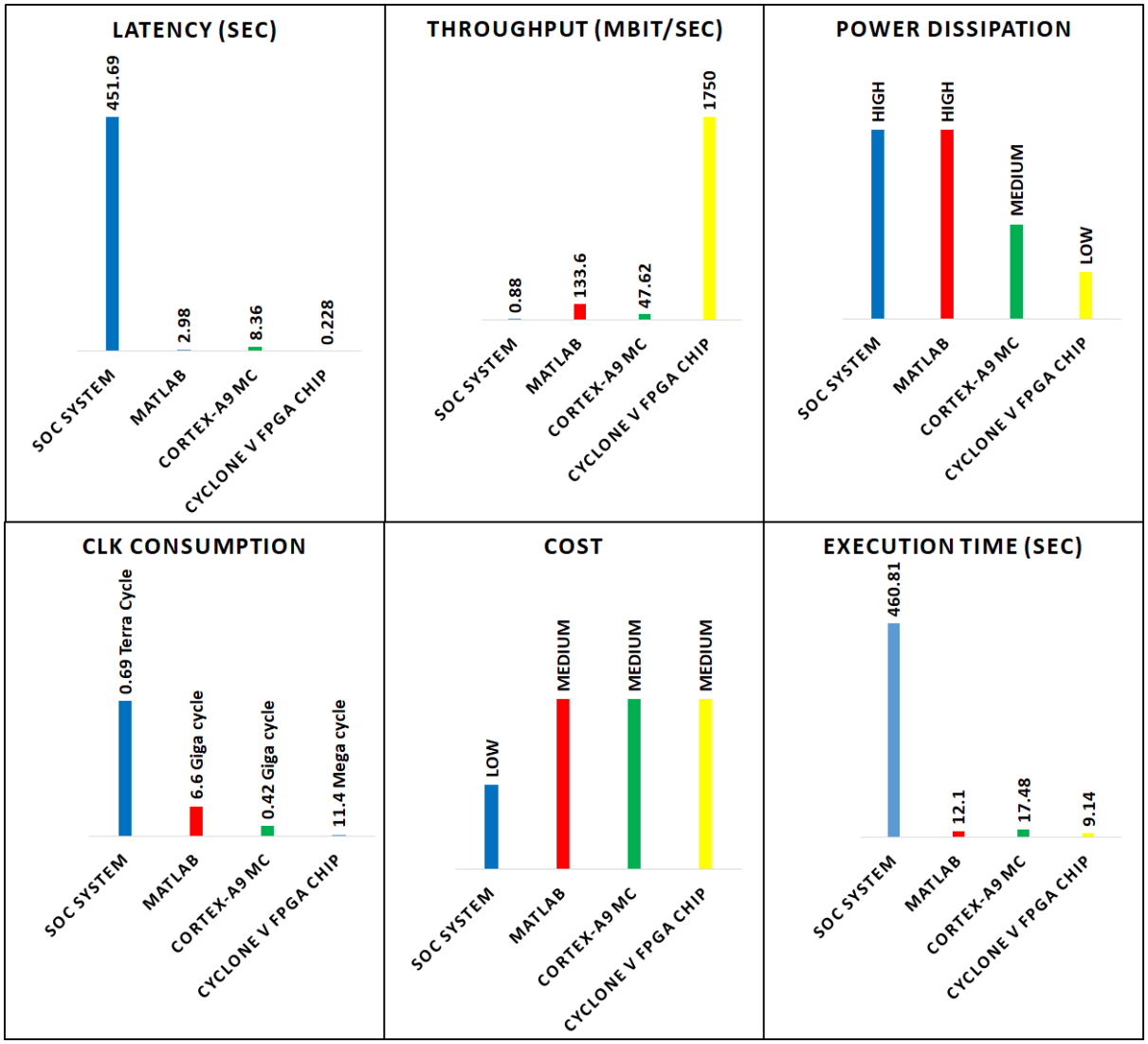

Figure 5. 13. *Result summary.*

The FPGA system in the present chapter performed the best in terms of throughput, latency, and power dissipation. The necessity for quantification of vision via PDLC windows is also satisfied. The overall efficiency of the suggested systems will, however, suffer if the size of the input data is increased. In the meantime, the handled data consists of (1080 x 960 pixels) 8-bit colour images. Further computational sophistication is necessary if image size is raised for better contrast precision (for instance, 1920 x 1080 pixels with 16-bit colour images). In a similar manner, the proposed system uses 16 images to define the contrast/voltage curve. For greater accuracy, the number of images taken may increase. However, the system should have more processing capacity to be able to handle additional mathematical operations.

A passing cloud can quickly cast shade over a structure. If the proposed system doesn't react in real-time, the PDLC optical transmission level will be inappropriate for the new condition in this situation. The system adjusts the PDLC biasing using the vision quantification process in response to changes in the exterior environment. Therefore, in order to instantly cover the outdoor lighting condition, the repetition time T_r should be as short as possible. The proposed process will be repeated in $T_r = 9.14\ sec$ if the suggested FPGA vision quantification system is used.

During the image-capturing phase of the proposed quantification process, if an unforeseen object passes in front of the window, a nonstandard shape of contrast curve will result. The resultant contrast value of the quantification operation will be significantly altered as a result. By including an inspection phase in the quantification process, this flaw can be avoided. It will be necessary to use an inspector circuit to examine contrast values by contrasting them with the typical pattern of contrast curve. Quantification processes should be restarted if the difference exceeds a threshold value. However, the inspection phase may increase system latency and decrease overall computational effectiveness.

In chapter four, the influence of the hysteresis phenomenon on the relation between the transparency and the applied voltage was briefly discussed. The change of the transparency against the excitation has two different paths depending on whether the input voltage is increasing or decreasing. It is concluded that for an excitation value, the transparency in the second path (while the applied voltage is decreasing) could be higher than the value in the first path (while the applied voltage is growing), and this can lead to a deviation between the determined transparency and the preferred value instantaneously. However, to overcome this hurdle, the proposed algorithm may be trained to choose only the first path. Every time the proposed algorithm estimates the contrast curve, the system starts in ascending order (from 0 to 200 volt). Further, during setting the new preferred voltage, the controller instructs the power driver to reset its output and then starts increasing the applied voltage in ascending order (from 0 to the preferred voltage).

When the quantification algorithm is run, or every time one of the suggested systems is used in a commercial structure, the optical transmission of the PDLC glazing will change from a an opaque to transparent state within a period of (T_r). The occupants will, however, have an

unpleasant sight experience as a result, particularly if the repetition time is only a few seconds. The quantification algorithm can be applied to a test window placed in an unoccupied or vacant area of the building to conquer this problem. The building's glazing will be informed of the controller's decision after the vision quantification process is completed on the test window.

It is feasible to quantify the vision via other kinds of glazing using the suggested quantification process, as the suggested systems express the vision in terms of optical transmission through PDLC glazing. The suggested systems can therefore be used with smart windows that have adjustable optical characteristics [68], [178]. This gives occupants and outside viewers a better visual connection by providing an instant evaluation of vision quality.

5.5 Summary

In summary, this chapter presented various approaches for implementing a controller to quantify the optical transmission for PDLC-windows in commercial structures. Real-time execution of a previously proposed vision quantification algorithm is performed by the automated controller. A total of sixteen images were shot for an external scene via a PDLC window by the implemented controller. The principal purpose of the implemented system is to compute and examine the vision contrast values of the photos and determine the appropriate excitation for the PDLC film instantaneously. Relying on the occupants desires, the biasing voltage level estimates the visible transparency via the PDLC window. Additionally, the automated system defines the threshold value of glazing optical transmission that maintains an acceptable level of vision in the direction of the exterior views. The following provides an illustration of the main result of this work:

1- The research highlighted that the Raspberry Pi-3 SoC system has a significant processing cost and power consumption and may not be able to address the suggested quantification process.
2- The latency of contrast estimation was 8.36 and 2.98 seconds for the ARM Cortex-A9 microcontroller and MATLAB realisations, respectively, which reflects a close

performance of both systems. However, there is a noticeable increase in the power dissipation and clock cycle consumption.

3- The most effective system, with a latency of only 0.228 sec and low power dissipation, uses an ARM Cyclone-V FPGA chip.
4- The ARM Cyclone V FPGA system was able to accomplish the proposed quantification process's minimal repetition time of $T_r = 9.14\ sec$.

The relaxed vision range through smart windows in commercial buildings can be identified by the automated systems that have been implemented. When it's necessary to evaluate the vision quality through the glazing of a window, the proposed system can be used with other types of smart glazing in addition to PDLC windows. The instant observation and control capabilities of the suggested system improve visual comfort in the interior spaces of commercial structures, in addition to previous studies on smart windows.

Chapter 6: Conclusion and Future Work

6.1 Conclusion

This research project focuses on the development of two types of intelligent windows based on specific climate conditions. For colder regions, an optimization method has been devised to enhance the utilisation of waste air in ventilating double-glazed windows. This approach aims to maximize the efficiency of these windows in cold environments. Conversely, for hotter regions, the study quantifies the visual quality provided by polymer dispersed liquid crystal (PDLC) double-glazed windows. Furthermore, an automated system has been implemented to autonomously carry out the quantification process, making it suitable for practical applications.

The primary objective of this study is to enhance the thermal and daylight performance of smart windows in order to create more comfortable environments for occupants in commercial buildings. By introducing these innovative solutions tailored to specific climate conditions, the research aims to contribute to the overall improvement of smart window technology and its practical implementation in real-world settings.

To accomplish the aim of the study, several objectives were successfully achieved. These objectives include:

- For double-glazed ventilated windows:
    - General optimisation procedures for using of waste air in windows ventilation have been experimentally investigated and evaluated.
- For PDLC double-glazed windows:
    - The contrast-based quantification algorithm for the vision through windows has been experimentally investigated and evaluated.
    - The mathematical representation for the lowest allowed vision quality through windows have been determined.
    - Implementation of automated system-based controller to realise the vision quantification process.

6.2 Contributions to knowledge

The contributions to knowledge are:

1- In the practical application of double-glazed windows in cold regions, there is a potential to enhance the thermal efficiency of commercial buildings by employing optimization techniques that effectively utilise waste air. However, a critical observation from the literature review indicates that previous studies focusing on the performance of ventilated windows have neglected to consider the limitations posed by the quantity of waste air supplied by buildings. This oversight is noteworthy because it has implications for the feasibility and effectiveness of implementing such ventilation systems.

   To illustrate this point, an example of a ventilated window was specifically discussed in the literature review of the present thesis (section 2.3.2). This example shed light on a practical scenario where a room is capable of providing a waste air flow rate of 10.5 m^3/h. However, the ventilated window, which aims to optimize air circulation, necessitates a flow rate that is four times higher than what the room can provide. This discrepancy underscores the importance of considering the constraints associated with the available waste air volume in order to accurately evaluate the viability and performance of ventilated windows.

   Therefore, in order to maximize the thermal efficiency of commercial buildings in cold regions using double-glazed windows, it is crucial to develop optimization procedures that account for the limitations imposed by the quantity of waste air supplied by buildings. By addressing this aspect, future research and practical implementations can effectively enhance the performance and sustainability of ventilated window systems in real-world applications.

2- Based on prior research in the field of smart windows, it has been established that smart films possess adjustable visible transmittance characteristics, making them suitable for introducing shading effects to conventional glazing. Particularly in hot regions, the integration of smart films with regular glass has the potential to reduce the amount of daylight entering indoor spaces and thus mitigate cooling energy consumption. However, an examination of existing literature revealed that previous studies have not adequately

considered the impact of decreased visible transmittance on the quality of vision when using smart films.

To address this research gap, the present study introduces a quantification process specifically designed to assess the visual experience through polymer dispersed liquid crystal (PDLC) double-glazed windows. The proposed method establishes a mathematical formula that establishes a relationship between the quality of vision achieved through PDLC double-glazed windows and the contrast of the displayed images. Additionally, a minimum level of acceptable vision quality through the window is defined, primarily in terms of image contrast.

Within the vision quantification algorithm, a new metric called the preferred vision ratio (PVR) is introduced. The PVR serves to describe the desired level of visual experience as perceived by users. By quantifying the preferred vision level using the PVR, this approach provides a means to objectively evaluate and optimize the visual performance of smart windows, ensuring that the resulting image contrast meets or exceeds the defined minimum threshold.

In summary, the study addresses the oversight in previous research regarding the impact of reduced visible transmittance on the quality of vision through smart films. By introducing a quantification process and utilising the preferred vision ratio (PVR), the study offers a comprehensive framework to assess and enhance the visual experience provided by PDLC double-glazed windows, ultimately contributing to the development of improved smart window technologies.

3- The practical implementation of an automated quantification controller for vision through PDLC double-glazed windows offers several advantages that contribute to the effective operation of the system. Firstly, it enables significant controllability and observability for PDLC windows, ensuring precise and reliable control over their visual properties. By incorporating artificial intelligence techniques, this controller serves as a mediator between the window itself and advanced computing technologies, thereby opening up new possibilities and opportunities in the field of smart windows.

In the context of this particular study, a noteworthy accomplishment is the achievement of the vision quantification process within a remarkably short time frame of 9.14 seconds, with the implementation of Field Programmable Gate Array (FPGA) technology. This fast

processing time is essential as it guarantees a seamless and comfortable visual experience through the window, while also ensuring the delivery of high-quality views to the users. The utilisation of FPGA implementation not only allows for efficient and swift execution of the vision quantification process but also enhances the overall feasibility of the system. By reducing the processing time to such a short duration, the controller ensures that users can enjoy a comfortable and visually pleasing environment without any noticeable delays or disruptions. Moreover, the high-quality views obtained through this efficient implementation demonstrate the potential for utilising FPGA technology to optimize the performance of smart windows and create a positive user experience.

In summary, the automated quantification controller for vision through PDLC double-glazed windows presents practical advantages by offering extensive controllability and observability. Its integration with artificial intelligence techniques introduces new possibilities for the field of smart windows. The study's achievement of completing the vision quantification process within 9.14 seconds through FPGA implementation signifies a feasible running time that guarantees both comfortable vision through the window and high-quality views, thereby contributing to the advancement of smart window technologies.

6.3 Findings

The findings and recommendations of this study are demonstrated in the following:

1- In the first topic addressed in this study, which focuses on utilising waste air in ventilating double-glazed windows, practical scenarios where the available quantity of waste air is insufficient for a number of windows in a building are considered. The proposed method offers the advantage of maintaining a certain level of thermal efficiency for these windows over extended periods. To achieve the optimal utilisation of waste air, the proposed method employs two strategies.

   The first strategy involves distributing the available flowrate of waste air to the windows one at a time. This approach allows for the systematic allocation of the limited waste air to each window, ensuring that every window receives its fair share of ventilation. The second strategy entails dividing the available flowrate of waste air among the ventilated windows. By implementing these approaches, different conditions of heat conduction and convection are created within the cavity of the ventilated windows. However, it is expected that one of these scenarios will lead to the highest energy savings.

   Importantly, the suggested method is applicable to already constructed buildings. This option presents an easier and cost-effective alternative to mitigate heat loss through windows compared to replacing the existing windows with more complex and specialized types. By implementing the proposed method, building owners and operators can optimize the thermal efficiency of their windows without requiring extensive renovations or costly replacements. This approach demonstrates the practicality and feasibility of utilising waste air in ventilating double-glazed windows to enhance energy efficiency and reduce heat loss in existing buildings.

   In Chapter 3 of the thesis, the proposed waste air optimization process was applied to an experimental test room model. The investigation revealed that the optimal case occurred when the waste air flowrate was distributed among three double-glazed windows simultaneously. By comparing these optimized windows to conventional double-glazed windows, a significant improvement was observed in terms of the overall heat transfer coefficient. The coefficient decreased from 3.82 W/(m^2.K) to 2.36 W/(m^2.K), representing a substantial reduction. Additionally, this optimization process resulted in an impressive energy savings of 83.1%.

Based on these findings, for practical applications, the study strongly recommends implementing the proposed waste air optimization process on existing double-glazed windows in commercial buildings. To facilitate this, simulation software can be utilised to aid in determining the most effective distribution of waste air among the available windows, leading to maximum potential energy savings. By following this approach, building owners and operators can make informed decisions and achieve significant improvements in energy efficiency without the need for costly window replacements.

By employing the proposed waste air optimization process and leveraging the power of simulation software, it becomes possible to identify the most efficient distribution strategy for waste air among the existing double-glazed windows. The expected outcome is a comprehensive understanding of how to maximize energy savings while maintaining the desired thermal performance. This practical recommendation allows for the implementation of cost-effective measures in commercial buildings to enhance overall energy efficiency and contribute to sustainability goals.

2- In practical applications, the proposed vision quantification process offers a significant advantage by enabling real-time tracking of the band of visible transmittance that corresponds to a comfortable vision through the window. By continuously monitoring and adjusting the visible transmittance, the system ensures that the visibility level does not fall below a specified threshold, thereby guaranteeing a minimum level of vision quality for the users. This capability addresses a crucial aspect that previous research has overlooked, namely the consideration of a threshold level of vision quality when reducing the visible transmittance of the window.

Without the inclusion of this threshold level, occupants may experience a disconnection from the outdoor environment, which is one of the essential functions provided by a window. By neglecting the minimum level of vision quality, previous approaches may inadvertently result in compromised visibility and hinder the desired interaction with the external surroundings. In contrast, the proposed vision quantification process takes into account the threshold level and employs a systematic approach to constrain the visible transmittance within a determined comfortable vision band.

Through experimental testing, the proposed system demonstrates its ability to maintain the visible transmittance of the window within the defined comfortable vision band,

thereby ensuring a preferred level of vision quality as determined by the preferred vision ratio (PVR). This dynamic control mechanism allows users to enjoy a comfortable and visually pleasing experience, with the system continuously adapting to optimize the vision quality based on real-time conditions.

In summary, the proposed vision quantification process offers a distinct advantage in practical applications by actively tracking and controlling the visible transmittance within a comfortable vision band. By considering the minimum threshold level of vision quality, the system ensures that occupants maintain a connection with the outdoor environment while enjoying a preferred level of visual experience. The experimental results validate the effectiveness of this system in maintaining a desired level of vision quality and highlight the importance of considering such factors in the design and implementation of smart window technologies.

During the deployment of the vision quantification process in the test room, it was observed that the solar heat gain coefficient ($SHGC$) exhibited a range of values, varying from 0.42 to 0.623, corresponding to the preferred vision ratio (PVR) range of 0 to 1. This variability in the $SHGC$ allows the system to effectively adjust the amount of daylight entering the interior spaces, thereby mitigating the greenhouse effect and regulating the overall thermal conditions within the room.

Furthermore, it was discovered that the set of PVR values ranging from 0 to 1 can directly influence the contrast of the vision experienced through the window, with values ranging from 0.18 to 0.37, respectively. The contrast value of 0.18, corresponding to a PVR of 0, ensures the minimum level of vision quality, guaranteeing that the visibility through the window does not fall below this threshold. Conversely, a contrast value of 0.37, corresponding to a PVR of 1, provides the maximum available vision quality, allowing users to experience enhanced clarity and visibility.

This novel approach of incorporating a range of PVR values and the corresponding contrast levels in the vision quantification process sets it apart from previous research efforts. By defining a minimum threshold of vision quality (0.18 contrast) and offering a spectrum of vision possibilities up to the maximum available quality (0.37 contrast), the system establishes strict rules that ensure a satisfactory and consistent level of visual experience through the window.

The absence of such a comprehensive system, which operates based on these rules, in previous research indicates the uniqueness and novelty of the proposed approach. By integrating the control of $SHGC$ and the quantification of vision quality through contrast, the system effectively optimizes the visual experience while maintaining the desired level of thermal comfort and energy efficiency. This significant contribution showcases the advancements made in the field and highlights the importance of considering both vision quality and thermal performance in the design and implementation of smart window technologies.

The proposed vision quantification process holds significant potential in the field of research concerning windows integrated with smart films. This study emphasizes the importance of considering the available visual band that ensures a comfortable and satisfying vision through windows. It is crucial to acknowledge that when reducing visible transparency, it is essential to maintain a connection between occupants and the outdoor scenes. Therefore, in future studies focusing on windows with smart films, it becomes imperative to incorporate the vision quantification algorithm as a means to evaluate the quality of vision through these windows.

By employing the vision quantification algorithm, researchers can effectively assess and quantify the visual experience offered by windows with smart films. This process becomes a vital tool in proving that lowering the visible transparency of such windows does not compromise occupants' connection with the outdoor environment. Instead, it aims to demonstrate that the reduced transparency still allows for a comfortable and engaging visual link with the surrounding scenes.

Future studies in this field can benefit from incorporating the proposed vision quantification process to validate and measure the quality of vision provided by windows integrated with smart films. This approach ensures that the visual experience is adequately evaluated, taking into account the impact of reduced transparency on occupants' connection with the outside world. By conducting such studies, researchers can further enhance the understanding and development of smart windows, ultimately leading to improved designs that strike a balance between privacy, energy efficiency, and maintaining a desirable visual experience for building occupants.

3- When implementing the proposed vision quantification process in real-world window applications, it is crucial to ensure its seamless and automatic operation. Recognizing this need, the study presented various scenarios demonstrating how the vision quantification process can be effectively implemented. In order to showcase a diverse range of hardware and software characteristics, as well as processing capabilities, the study proposed four distinct implementation methods. By exploring these different techniques, the study aimed to provide a comprehensive understanding of their respective advantages and disadvantages.

   By presenting multiple implementation methods, the study offers valuable insights into the practical aspects of deploying the vision quantification process in real windows applications. Each method represents a unique approach, utilising different hardware configurations and software components. Through this diversity, the study aims to highlight the versatility of the vision quantification process and its compatibility with various technological environments.

   Moreover, by evaluating the pros and cons of each implementation method, the study provides valuable information for researchers, developers, and practitioners in the field. This analysis enables a deeper understanding of the trade-offs involved in selecting a specific implementation technique, considering factors such as cost, complexity, computational requirements, and integration feasibility.

   Ultimately, the study's objective is to offer a comprehensive overview of the various ways in which the vision quantification process can be incorporated into real-world window applications. By presenting multiple implementation scenarios and analysing their respective advantages and disadvantages, the study aims to provide a solid foundation for researchers and practitioners to make informed decisions and select the most suitable technique based on their specific requirements and constraints. This comprehensive exploration of implementation methods contributes to advancing the field of smart windows and facilitates the practical adoption of the vision quantification process in real-world settings.

   The proposed scenarios encompass a range of commonly used implementation techniques. The first scenario involves a PC-based MATLAB implementation, which demonstrates powerful performance in computing image contrast. However, in practical applications, there is a need for standalone systems that do not rely on a PC, as they offer

enhanced reliability and independence. In this regard, the Raspberry-Pi3 system on chip (SoC) integrated with Python programming language emerges as a flexible option commonly employed in various applications. Nevertheless, it exhibits inferior performance compared to the MATLAB method in terms of latency, throughput, and power consumption.

On the other hand, the Cortex-A9 microcontroller system integrated with C programming language proves to be a viable alternative, demonstrating comparable efficiency to the MATLAB implementation. This approach offers a balance between computational power and practicality for real-world applications.

Another technique explored in the study is the field programmable gate array (FPGA), which offers unique capabilities. The FPGA chip has the distinctive property of converting any design into a fixed circuit on the chip after prototyping, resulting in very low latency. This feature makes the FPGA method highly efficient and well-suited for handling the vision quantification process in practical applications. Its impressive efficiency sets it apart from other techniques, qualifying it as a suitable choice for implementing the vision quantification process.

By presenting and comparing these scenarios, the study provides valuable insights into the strengths and limitations of different implementation techniques for the vision quantification process. This analysis aids researchers and practitioners in understanding the trade-offs involved in selecting the most appropriate approach for their specific application requirements. Furthermore, the study highlights the potential of the FPGA method, with its low latency and impressive efficiency, as a promising solution for handling vision quantification in real-world scenarios.

6.4 Limitation of the study

Possible limitations of this study include the small size of test rooms and windows that used in the experiments due to manual setup utilised for assessing the proposed systems.

6.5 Future work

In the proposed process for optimizing the utilisation of waste air in double-glazed ventilation, it is important to acknowledge that the experimental outcomes obtained with the small window size used in the experiment may not precisely reflect the practical situation. Consequently, as a future study, it is recommended to apply the waste air optimization experiment in a room and window with real dimensions. By conducting such an experiment, the objective would be to emphasize the outcomes of this study and demonstrate their applicability to industrial applications.

The current study assumed that the source of air used for ventilating the window is the waste air generated within the room itself. However, in future studies, it is suggested to consider a larger amount of waste air from other areas of the building, such as kitchens. The inclusion of additional waste air can enhance the efficiency of the ventilation process. It is important to note, though, that such air may be humid and impure, making it unsuitable for direct use in the ventilation process as it could soil the glazing. To address this, the waste air should be properly cleaned and dried before being utilised. This can be achieved through the implementation of suitable techniques, such as filters and heat exchangers, to remove impurities and reduce moisture content.

By considering these aspects in future studies, a more comprehensive understanding of waste air optimization in double-glazed ventilation can be attained. Incorporating real-scale dimensions and exploring additional sources of waste air, along with implementing appropriate cleaning and drying techniques, will provide valuable insights into the practical application of this optimization process. Ultimately, such research endeavours contribute to the development of more efficient and effective ventilation strategies for various industrial settings.

As a potential avenue for future research, the proposed vision quantification method for PDLC windows could benefit from the incorporation of high dynamic range (HDR) images to achieve a more precise contrast curve. The experiment conducted in this study was primarily carried out during sunny days, which provided valuable insights into vision quantification under specific weather conditions. However, to enhance the applicability of the system in practical scenarios, it is recommended to replicate the experiment across a range of weather conditions that can significantly impact vision through the window.

By conducting experiments during various weather conditions, such as rainy, foggy, and cloudy skies, the proposed system can capture a more comprehensive understanding of the impact of different atmospheric phenomena on vision quality. These weather conditions can significantly alter the lighting conditions and visibility through the PDLC windows, thereby affecting the contrast curve and overall visual experience. By considering a broader spectrum of weather conditions, the system can account for the real-world variability in environmental factors and provide more accurate quantification of vision quality.

Incorporating different weather conditions into the experimental setup will enable researchers to evaluate the robustness and adaptability of the vision quantification method. It will also help validate the system's performance across a wider range of scenarios, allowing for a more reliable assessment of its effectiveness in practical applications. By expanding the experimental scope to include different weather conditions, researchers can enhance the practicality and relevance of the proposed vision quantification method for PDLC windows, providing valuable insights for architectural design, building energy management, and occupant comfort optimization.

In terms of future developments for the automated vision quantification system, the superior processing efficiency demonstrated by the FPGA implementation suggests that a full FPGA implementation should be considered. This would involve integrating the FPGA circuitry with both the power driver of the PDLC film and the digital camera module. By incorporating these components, the system can achieve enhanced functionality and performance.

Furthermore, it is worth noting that the camera and PDLC driver exhibit a longer delay (8.9 s) compared to the FPGA chip's computing time for contrast calculation. To minimize overall system latency, it would be beneficial to explore the utilisation of alternate high-performance

modules for these components. By employing modules with faster response times, the system can reduce delays and improve real-time performance.

Another aspect to consider is the handling of moving images through the PDLC window during the subsequent step of the vision quantification process. Incorporating image-processing methods into the system's framework would equip it with the capability to effectively manage any sudden changes that may occur in real-time scenes while capturing images. Developing a supplementary system that can swiftly detect scene changes would facilitate the maintenance of a consistent and uniform contrast curve.

To ensure the desired uniformity in the contrast curve, this supplementary system would analyse the correlative data between successive images. By examining the relationships and patterns within the recurring images, the system can ensure a cohesive and smooth transition in the contrast curve, thereby enhancing the accuracy and reliability of the vision quantification process.

Considering these future improvements, such as full FPGA implementation, integration with high-performance modules, and the creation of a supplementary system for scene change detection and correlation analysis, the automated vision quantification system can be further refined to deliver enhanced functionality, real-time performance, and accurate quantification of vision quality through PDLC windows.

References

[1] "IEA, Global status report for buildings and construction 2019, Tech. rep., IEA, Paris, 2019".

[2] "Global Status Report for Buildings and Construction, 2022".

[3] "EIA, Electric power annual 2020, Tech. rep, US Energy Information Administration (2021)".

[4] "N. Zhou, N. Khanna, W. Feng, J. Ke, M. Levine, Scenarios of energy efficiency and CO2 emissions reduction potential in the buildings sector in China to year 2050, Nat Energy, 3 (2018), pp. 1-7".

[5] "McNeil MA, Feng W, du Can SdlR, Khanna NZ, Ke J, Zhou N. Energy efficiency outlook in China's urban buildings sector through 2030. Energy Pol. 2016;97:532–9".

[6] R. K. Jaysawal, S. Chakraborty, D. Elangovan, and S. Padmanaban, "Concept of net zero energy buildings (NZEB) - A literature review," *Clean Eng Technol*, vol. 11, p. 100582, Dec. 2022, doi: 10.1016/j.clet.2022.100582.

[7] M. Pompilio, I. Ierides, and F. Cacialli, "Biomimetic Approaches to 'Transparent' Photovoltaics: Current and Future Applications," *Molecules*, vol. 28, no. 1. MDPI, Jan. 01, 2023. doi: 10.3390/molecules28010180.

[8] G. R. Setyantho, H. Park, and S. Chang, "Multi-criteria performance assessment for semi-transparent photovoltaic windows in different climate contexts," *Sustainability (Switzerland)*, vol. 13, no. 4, pp. 1–22, Feb. 2021, doi: 10.3390/su13042198.

[9] M. Oh, C. Lee, J. Park, K. Lee, and S. Tae, "Evaluation of energy and daylight performance of old office buildings in South Korea with curtain walls remodeled using polymer dispersed liquid crystal (PDLC) films," *Energies (Basel)*, vol. 12, no. 19, Sep. 2019, doi: 10.3390/en12193679.

[10] C. Y. Li *et al.*, "Electro-optical properties of a polymer dispersed and stabilized cholesteric liquid crystals system constructed by a stepwise UV-initiated radical/cationic polymerization," *Crystals (Basel)*, vol. 9, no. 6, Jun. 2019, doi: 10.3390/cryst9060282.

[11] H. W. S.G. Li, "Summarization of present building energy consumption and corresponding strategies in China," *Environmental Science and Management 33(2)*, pp. 6–9, 2008.

[12] International Energy Agency, "Statistics and Data." [Online]. Available: https://www.iea.org/

[13] J. Zemitis and A. Borodinecs, "Energy saving potential of ventilation systems with exhaust air heat recovery," *IOP Conf Ser Mater Sci Eng*, vol. 660, no. 1, 2019, doi: 10.1088/1757-899X/660/1/012019.

[14] N. Lu, T. Taylor, W. Jiang, J. Correia, L. R. Leung, and P. C. Wong, “The temperature sensitivity of the residential load and commercial building load,” *2009 IEEE Power and Energy Society General Meeting, PES ’09*, 2009, doi: 10.1109/PES.2009.5275654.

[15] Z. Jiang and H. Rahimi-Eichi, “Design, modeling and simulation of a green building energy system,” *2009 IEEE Power and Energy Society General Meeting, PES ’09*, pp. 1–7, 2009, doi: 10.1109/PES.2009.5275755.

[16] I. Ahmed *et al.*, “A Critical Analysis of the Energy Requirements of a Commercial Building Based on Various Types of Glass Insulations,” *Sustainability (Switzerland)*, vol. 15, no. 4, Feb. 2023, doi: 10.3390/su15042998.

[17] A. M. Pavlenko and K. Sadko, “Evaluation of Numerical Methods for Predicting the Energy Performance of Windows,” *Energies*, vol. 16, no. 3. MDPI, Feb. 01, 2023. doi: 10.3390/en16031425.

[18] Z. Respondek, “Heat transfer through insulating glass units subjected to climatic loads,” *Materials*, vol. 13, no. 2, Jan. 2020, doi: 10.3390/ma13020286.

[19] A. Bahadori-Jahromi, A. Rotimi, A. Mylona, P. Godfrey, and D. Cook, “Impact of window films on the overall energy consumption of existing UK hotel buildings,” *Sustainability (Switzerland)*, vol. 9, no. 5, 2017, doi: 10.3390/su9050731.

[20] A. P. Brdnik, “Thermal performance optimization of double and triple glazing systems for Slovenian climate conditions,” *Sustainability (Switzerland)*, vol. 13, no. 21, Nov. 2021, doi: 10.3390/su132111857.

[21] A. Eljojo, “Effect of Windows Size, Position and Orientation on the Amount of Energy Needed for Winter Heating and Summer Cooling,” *Journal of Engineering Research and Technology*, vol. 1, no. 1, pp. 0–8, 2017, doi: 10.13140/RG.2.2.32424.47361.

[22] A. S. Muhaisen and H. R. Dabboor, “Studying the Impact of Orientation, Size, and Glass Material of Windows on Heating and Cooling Energy Demand of the Gaza Strip Buildings,” *Journal of Architecture and Planning*, vol. 27, no. 1, pp. 1–15, 2015.

[23] A. M. A. Youssef, Z. J. Zhai, and R. M. Reffat, “Design of optimal building envelopes with integrated photovoltaics,” *Build Simul*, vol. 8, no. 3, pp. 353–366, 2015, doi: 10.1007/s12273-015-0214-y.

[24] A. Cannavale, U. Ayr, and F. Martellotta, “Energetic and visual comfort implications of using perovskite-based building-integrated photovoltaic glazings,” *Energy Procedia*, vol. 126, pp. 636–643, 2017, doi: 10.1016/j.egypro.2017.08.256.

[25] S. Saridar and H. Elkadi, “The impact of applying recent façade technology on daylighting performance in buildings in eastern Mediterranean,” *Build Environ*, vol. 37, no. 11, pp. 1205–1212, 2002, doi: 10.1016/S0360-1323(01)00095-6.

[26] E. Rivas, J. L. Santiago, and B. Sánchez, “Advances on the Influence of Vegetation and Forest on Urban Air Quality and Thermal Comfort—Series II,” *Forests*, vol. 14, no. 2. MDPI, Feb. 01, 2023. doi: 10.3390/f14020284.

[27] Y. Mao, H. Xie, X. Zhang, F. Hou, and M. Wang, “Study on the Applicable Room Size Dimension of Stratum Ventilation for Heating Based on Multi-Criteria Analytic Hierarchy Process-Entropy Weight Model,” *Buildings*, vol. 13, no. 2, Feb. 2023, doi: 10.3390/buildings13020381.

[28] A. Laouadi, L. Ji, C. Shu, L. Wang, and M. A. Lacasse, “Overheating Risk Analysis in Long-Term Care Homes—Development of Overheating Limit Criteria,” *Buildings*, vol. 13, no. 2, Feb. 2023, doi: 10.3390/buildings13020390.

[29] C. Chen *et al.*, “Deep Reinforcement Learning-Based Joint Optimization Control of Indoor Temperature and Relative Humidity in Office Buildings,” *Buildings*, vol. 13, no. 2, Feb. 2023, doi: 10.3390/buildings13020438.

[30] D. Sekartaji, Y. Ryu, D. Novianto, K. Eto, and W. Gao, “Energy-Use and Indoor Thermal Performance in Junior High School Building after Air-Conditioning Installation with the Private Finance Initiative,” *Buildings*, vol. 13, no. 2, Feb. 2023, doi: 10.3390/buildings13020455.

[31] P. Lamsal, S. B. Bajracharya, and H. B. Rijal, “A Review on Adaptive Thermal Comfort of Office Building for Energy-Saving Building Design,” *Energies*, vol. 16, no. 3. MDPI, Feb. 01, 2023. doi: 10.3390/en16031524.

[32] A. Yaacoub, M. Esseghir, and L. Merghem-Boulahia, “A Review of Different Methodologies to Study Occupant Comfort and Energy Consumption,” *Energies*, vol. 16, no. 4. MDPI, Feb. 01, 2023. doi: 10.3390/en16041634.

[33] C. C. Cheng, H. H. Tsai, D. Y. Chin, and D. Lee, “Establishment of a Thermal Comfort Model for Young Adults with Physiological Parameters in Cold and Hot Stimulation,” *Sustainability (Switzerland)*, vol. 15, no. 3, Feb. 2023, doi: 10.3390/su15032667.

[34] M. Sedighi, P. Pourmoghaddam Qhazvini, and M. Amidpour, “Algae-Powered Buildings: A Review of an Innovative, Sustainable Approach in the Built Environment,” *Sustainability (Switzerland)*, vol. 15, no. 4. MDPI, Feb. 01, 2023. doi: 10.3390/su15043729.

[35] I. Lahmar, A. Cannavale, F. Martellotta, and N. Zemmouri, “The Impact of Building Orientation and Window-to-Wall Ratio on the Performance of Electrochromic Glazing in Hot Arid Climates: A Parametric Assessment,” *Buildings*, vol. 12, no. 6, Jun. 2022, doi: 10.3390/buildings12060724.

[36] N. H. Matin, A. Eydgahi, and P. Matin, “The Effect of Smart Colored Windows on Visual Performance of Buildings,” *Buildings*, vol. 12, no. 6, Jun. 2022, doi: 10.3390/buildings12060861.

[37] N. H. Matin, A. Eydgahi, A. Gharipour, and P. Matin, “A Novel Framework for Optimizing Indoor Illuminance and Discovering Association of Involved Variables,” *Buildings*, vol. 12, no. 7, Jul. 2022, doi: 10.3390/buildings12070878.

[38] Y. Wang and D. Durmus, “Image Quality Metrics, Personality Traits, and Subjective Evaluation of Indoor Environment Images,” *Buildings*, vol. 12, no. 12, Dec. 2022, doi: 10.3390/buildings12122086.

[39] J. K. Day, B. Futrell, R. Cox, and S. N. Ruiz, “Blinded by the light: Occupant perceptions and visual comfort assessments of three dynamic daylight control systems and shading strategies,” *Build Environ*, vol. 154, pp. 107–121, May 2019, doi: 10.1016/j.buildenv.2019.02.037.

[40] G. H. Lim, N. Keumala, and N. A. Ghafar, “Energy saving potential and visual comfort of task light usage for offices in Malaysia,” *Energy Build*, vol. 147, pp. 166–175, Jul. 2017, doi: 10.1016/j.enbuild.2017.05.004.

[41] E. Sorooshnia, M. Rashidi, P. Rahnamayiezekavat, and B. Samali, “Optimizing Window Configuration Counterbalancing Energy Saving and Indoor Visual Comfort for Sydney Dwellings,” *Buildings*, vol. 12, no. 11, Nov. 2022, doi: 10.3390/buildings12111823.

[42] M. Fakhari, R. Fayaz, and R. Lollini, “The Impact of Evaluated Daylight to the Total Light Ratio on the Comfort Level in Office Buildings,” *Buildings*, vol. 12, no. 12, Dec. 2022, doi: 10.3390/buildings12122161.

[43] A. Ghosh, A. Mesloub, M. Touahmia, and M. Ajmi, “Visual comfort analysis of semi-transparent perovskite based building integrated photovoltaicwindow for hot desert climate (riyadh, saudi arabia),” *Energies (Basel)*, vol. 14, no. 4, Feb. 2021, doi: 10.3390/en14041043.

[44] M. Rabani, H. Bayera Madessa, and N. Nord, “Achieving zero-energy building performance with thermal and visual comfort enhancement through optimization of fenestration, envelope, shading device, and energy supply system,” *Sustainable Energy Technologies and Assessments*, vol. 44, Apr. 2021, doi: 10.1016/j.seta.2021.101020.

[45] M. Basinska, D. Kaczorek, and H. Koczyk, “Building thermo-modernisation solution based on the multi-objective optimisation method,” *Energies (Basel)*, vol. 13, no. 6, 2020, doi: 10.3390/en13061433.

[46] S. Cesari, P. Valdiserri, M. Coccagna, and S. Mazzacane, “The energy saving potential of wide windows in hospital patient rooms, optimizing the type of glazing and lighting control strategy under different climatic conditions,” *Energies (Basel)*, vol. 13, no. 8, Apr. 2020, doi: 10.3390/en13082116.

[47] C. H. Wang, N. W. Kuo, and K. Anthony, “Impact of window views on recovery—an example of post-cesarean section women,” *International Journal for Quality in Health Care*, vol. 31, no. 10. Oxford University Press, pp. 798–803, Dec. 01, 2019. doi: 10.1093/intqhc/mzz046.

[48] A. Fikfak, M. Zbašnik-Senegačnik, and S. Drobne, “Greenery as an Element of Imageability in Window Views,” *Land (Basel)*, vol. 11, no. 12, Dec. 2022, doi: 10.3390/land11122157.

[49] P. Pilechiha, M. Mahdavinejad, F. Pour Rahimian, P. Carnemolla, and S. Seyedzadeh, “Multi-objective optimisation framework for designing office windows: quality of view, daylight and energy efficiency,” *Appl Energy*, vol. 261, Mar. 2020, doi: 10.1016/j.apenergy.2019.114356.

[50] D. Katunský, E. Dolníková, and S. Doroudiani, “Integrated lighting efficiency analysis in large industrial buildings to enhance indoor environmental quality,” *Buildings*, vol. 7, no. 2, Jun. 2017, doi: 10.3390/buildings7020047.

[51] A. Batool, P. Rutherford, P. McGraw, T. Ledgeway, and S. Altomonte, “Window Views: Difference of Perception during the COVID-19 Lockdown,” *LEUKOS - Journal of Illuminating Engineering Society of North America*, vol. 17, no. 4, pp. 380–390, 2021, doi: 10.1080/15502724.2020.1854780.

[52] Y. A. Dodo, M. Z. Kandar, D. R. Ossen, J. D. azimi Jibril, A. H. Bornoma, and A. I. Abubakar, “Importance of a view window in rating green office buildings,” in *Advanced Materials Research*, 2013, pp. 180–183. doi: 10.4028/www.scientific.net/AMR.689.180.

[53] A. Roetzel, A. Tsangrassoulis, U. Dietrich, and S. Busching, “On the influence of building design, occupants and heat waves on comfort and greenhouse gas emissions in naturally ventilated offices. A study based on the EN 15251 adaptive thermal comfort model in Athens, Greece,” *Build Simul*, vol. 3, no. 2, pp. 87–103, Jun. 2010, doi: 10.1007/s12273-010-0002-7.

[54] G. Ma and X. Pan, “Research on a visual comfort model based on individual preference in china through machine learning algorithm,” *Sustainability (Switzerland)*, vol. 13, no. 14, Jul. 2021, doi: 10.3390/su13147602.

[55] A. Meresi, “Evaluating daylight performance of light shelves combined with external blinds in south-facing classrooms in Athens, Greece,” *Energy Build*, vol. 116, pp. 190–205, Mar. 2016, doi: 10.1016/j.enbuild.2016.01.009.

[56] M. B. C. Aries, J. A. Veitch, and G. R. Newsham, “Windows, view, and office characteristics predict physical and psychological discomfort,” *J Environ Psychol*, vol. 30, no. 4, pp. 533–541, Dec. 2010, doi: 10.1016/j.jenvp.2009.12.004.

[57] J. A. Jakubiec, “Bachelor of Science in Architecture Georgia Institute of Technology,” 2008.

[58] M. Detsi, A. Manolitsis, I. Atsonios, I. Mandilaras, and M. Founti, “Energy savings in an office building with high WWR using glazing systems combining thermochromic and electrochromic layers,” *Energies (Basel)*, vol. 13, no. 11, Jun. 2020, doi: 10.3390/en13113020.

[59] Y. Ko, H. Oh, H. Hong, and J. Min, “Energy consumption verification of spd smart window, controllable according to solar radiation in south korea,” *Energies (Basel)*, vol. 13, no. 21, Nov. 2020, doi: 10.3390/en13215643.

[60] A. Hemaida, A. Ghosh, S. Sundaram, and T. K. Mallick, “Simulation study for a switchable adaptive polymer dispersed liquid crystal smart window for two climate zones (Riyadh and London),” *Energy Build*, vol. 251, Nov. 2021, doi: 10.1016/j.enbuild.2021.111381.

[61] Z. Fan, M. Liu, and S. Tang, “A multi-objective optimization design method for gymnasium facade shading ratio integrating energy load and daylight comfort,” *Build Environ*, p. 108527, Oct. 2021, doi: 10.1016/j.buildenv.2021.108527.

[62] M. Hegazy, K. Yasufuku, and H. Abe, “Evaluating and visualizing perceptual impressions of daylighting in immersive virtual environments,” *Journal of Asian Architecture and Building Engineering*, vol. 20, no. 6, pp. 768–784, 2021, doi: 10.1080/13467581.2020.1800477.

[63] T. Futagami, T. Yano, C. Huang, and T. Enohara, “Experimental evaluation for daylight-linked gradation lighting control using image-based motion sensors,” *IEEJ Transactions on Electrical and Electronic Engineering*, vol. 15, no. 5, pp. 723–732, May 2020, doi: 10.1002/tee.23108.

[64] J. Suk and M. Schiler, “Investigation of Evalglare software, daylight glare probability and high dynamic range imaging for daylight glare analysis,” *Lighting Research and Technology*, vol. 45, no. 4, pp. 450–463, 2013, doi: 10.1177/1477153512458671.

[65] M. K. Basher, M. N. E. Alam, and K. Alameh, “Design, development, and characterization of low distortion advanced semitransparent photovoltaic glass for buildings applications,” *Energies (Basel)*, vol. 14, no. 13, Jul. 2021, doi: 10.3390/en14133929.

[66] A. P. Gardymova, M. N. Krakhalev, V. Y. Zyryanov, A. A. Gruzdenko, A. A. Alekseev, and V. Y. Rudyak, “Polymer dispersed cholesteric liquid crystals with a toroidal director configuration under an electric field,” *Polymers (Basel)*, vol. 13, no. 5, pp. 1–11, Mar. 2021, doi: 10.3390/polym13050732.

[67] G. Chen *et al.*, “The electro-optical properties and adhesion strength of epoxy-polymercaptan-based polymer dispersed liquid crystal films,” *Crystals (Basel)*, vol. 11, no. 6, Jun. 2021, doi: 10.3390/cryst11060576.

[68] A. V. Shchegolkov, S. H. Jang, A. V. Shchegolkov, Y. V. Rodionov, A. O. Sukhova, and M. S. Lipkin, “A brief overview of electrochromic materials and related devices: A nanostructured materials perspective,” *Nanomaterials*, vol. 11, no. 9. MDPI, Sep. 01, 2021. doi: 10.3390/nano11092376.

[69] M. Brzezicki, “A systematic review of the most recent concepts in smart windows technologies with a focus on electrochromics,” *Sustainability (Switzerland)*, vol. 13, no. 17. MDPI, Sep. 01, 2021. doi: 10.3390/su13179604.

[70] B. W. C. Au and K. Y. Chan, “Towards an All-Solid-State Electrochromic Device: A Review of Solid-State Electrolytes and the Way Forward,” *Polymers*, vol. 14, no. 12. MDPI, Jun. 01, 2022. doi: 10.3390/polym14122458.

[71] J. Wu, L. Zhang, Z. Liu, and Z. Wu, “Coupled optical-electrical-thermal analysis of a semi-transparent photovoltaic glazing façade under building shadow,” *Appl Energy*, vol. 292, Jun. 2021, doi: 10.1016/j.apenergy.2021.116884.

[72] C. Wang, J. Ji, M. M. Uddin, B. Yu, and Z. Song, “The study of a double-skin ventilated window integrated with CdTe cells in a rural building,” *Energy*, vol. 215, Jan. 2021, doi: 10.1016/j.energy.2020.119043.

[73] J. H. Kim and S. H. Han, “Indoor Daylight Performances of Optimized Transmittances with Electrochromic-Applied Kinetic Louvers,” *Buildings*, vol. 12, no. 3, Mar. 2022, doi: 10.3390/buildings12030263.

[74] J. Guo and C. Zhang, “Utilisation of Window System as Exhaust Air Heat Recovery Device and Its Energy Performance Evaluation: A Comparative Study,” *Energies (Basel)*, vol. 15, no. 9, May 2022, doi: 10.3390/en15093116.

[75] J. H. Kim, J. Hong, and S. H. Han, “Optimized physical properties of electrochromic smart windows to reduce cooling and heating loads of office buildings,” *Sustainability (Switzerland)*, vol. 13, no. 4, pp. 1–30, Feb. 2021, doi: 10.3390/su13041815.

[76] L. Olivieri, E. Caamaño-Martin, F. Olivieri, and J. Neila, “Integral energy performance characterization of semi-transparent photovoltaic elements for building integration under real operation conditions,” *Energy Build*, vol. 68, no. PARTA, pp. 280–291, 2014, doi: 10.1016/j.enbuild.2013.09.035.

[77] D. W. Dockery, “Health Effects of Particulate Air Pollution,” *Ann Epidemiol*, vol. 19, no. 4, pp. 257–263, Apr. 2009, doi: 10.1016/j.annepidem.2009.01.018.

[78] N. Yamaguchi, T. Ichijo, A. Sakotani, T. Baba, and M. Nasu, “Global dispersion of bacterial cells on Asian dust,” *Sci Rep*, vol. 2, 2012, doi: 10.1038/srep00525.

[79] A. A. Wieser, M. Scherz, A. Passer, and H. Kreiner, “Challenges of a healthy built environment: Air pollution in construction industry,” *Sustainability (Switzerland)*, vol. 13, no. 18. MDPI, Sep. 01, 2021. doi: 10.3390/su131810469.

[80] E. Cuce, D. Harjunowibowo, and P. M. Cuce, “Renewable and sustainable energy saving strategies for greenhouse systems: A comprehensive review,” *Renewable and Sustainable Energy Reviews*, vol. 64. Elsevier Ltd, pp. 34–59, Oct. 01, 2016. doi: 10.1016/j.rser.2016.05.077.

[81] M. I. Elhadary, A. M. Y. Alzahrani, R. M. H. Aly, and B. Elboshy, “A comparative study for forced ventilation systems in industrial buildings to improve the workers’ thermal comfort,” *Sustainability (Switzerland)*, vol. 13, no. 18, Sep. 2021, doi: 10.3390/su131810267.

[82] R. E. C. Amaral *et al.*, “Waste management and operational energy for sustainable buildings: A review,” *Sustainability (Switzerland)*, vol. 12, no. 13. MDPI, Jul. 01, 2020. doi: 10.3390/su12135337.

[83] S. Park, H. Park, and J. Seo, “Analysis on the exhaust air recirculation of the ventilation system in multi-story building,” *Applied Sciences (Switzerland)*, vol. 11, no. 10, May 2021, doi: 10.3390/app11104441.

[84] Y. Hu, P. K. Heiselberg, and R. Guo, “Ventilation cooling/heating performance of a PCM enhanced ventilated window - an experimental study,” *Energy Build*, vol. 214, p. 109903, 2020, doi: 10.1016/j.enbuild.2020.109903.

[85] T. G. S. Lago, K. A. R. Ismail, and F. A. M. Lino, “Ventilated double glass window with reflective film: Modeling and assessment of performance,” *Solar Energy*, vol. 185, no. April, pp. 72–88, 2019, doi: 10.1016/j.solener.2019.04.047.

[86] S. Zeyninejad Movassag and K. Zamzamian, “Numerical investigation on the thermal performance of double glazing air flow window with integrated blinds,” *Renew Energy*, vol. 148, pp. 852–863, 2020, doi: 10.1016/j.renene.2019.10.170.

[87] G. Michaux, R. Greffet, P. Salagnac, and J. B. Ridoret, “Modelling of an airflow window and numerical investigation of its thermal performances by comparison to conventional double and triple-glazed windows,” *Appl Energy*, vol. 242, no. March, pp. 27–45, 2019, doi: 10.1016/j.apenergy.2019.03.029.

[88] M. Liu, P. K. Heiselberg, O. K. Larsen, L. Mortensen, and J. Rose, “Investigation of Different Configurations of a Ventilated Window to Optimize Both Energy Efficiency and Thermal Comfort,” *Energy Procedia*, vol. 132, pp. 478–483, 2017, doi: 10.1016/j.egypro.2017.09.660.

[89] R. Lollini, L. Danza, and I. Meroni, “Energy efficiency of a dynamic glazing system,” *Solar Energy*, vol. 84, no. 4, pp. 526–537, 2010, doi: 10.1016/j.solener.2009.12.006.

[90] B. Nourozi, A. Ploskić, Y. Chen, J. Ning-Wei Chiu, and Q. Wang, “Heat transfer model for energy-active windows – An evaluation of efficient reuse of waste heat in buildings,” *Renew Energy*, vol. 162, pp. 2318–2329, 2020, doi: 10.1016/j.renene.2020.10.043.

[91] C. Zhang, W. Gang, J. Wang, X. Xu, and Q. Du, “Numerical and experimental study on the thermal performance improvement of a triple glazed window by utilising low-grade exhaust air,” *Energy*, vol. 167, pp. 1132–1143, 2019, doi: 10.1016/j.energy.2018.11.076.

[92] T. G. S. Lago, K. A. R. Ismail, and F. A. M. Lino, “Ventilated double glass window with reflective film: Modeling and assessment of performance,” *Solar Energy*, vol. 185, pp. 72–88, Jun. 2019, doi: 10.1016/j.solener.2019.04.047.

[93] G. Michaux, R. Greffet, P. Salagnac, and J. B. Ridoret, “Modelling of an airflow window and numerical investigation of its thermal performances by comparison to conventional double and triple-glazed windows,” *Appl Energy*, vol. 242, pp. 27–45, May 2019, doi: 10.1016/j.apenergy.2019.03.029.

[94] S. Zeyninejad Movassag and K. Zamzamian, “Numerical investigation on the thermal performance of double glazing air flow window with integrated blinds,” *Renew Energy*, vol. 148, pp. 852–863, Apr. 2020, doi: 10.1016/j.renene.2019.10.170.

[95] C. Zhang, W. Gang, J. Wang, X. Xu, and Q. Du, “Numerical and experimental study on the thermal performance improvement of a triple glazed window by utilising low-grade exhaust air,” *Energy*, vol. 167, pp. 1132–1143, Jan. 2019, doi: 10.1016/j.energy.2018.11.076.

[96] ASHRAE, *Standard 62.1, Ventilation for Acceptable Indoor Air Quality; American Society of Heating, Refrigerating and Air conditioning Engineers*. Atlanta, GA, USA, 2004.

[97] S. Sayadi, A. Hayati, and M. Salmanzadeh, “Optimization of window-to-wall ratio for buildings located in different climates: An IDA-indoor climate and energy simulation study,” *Energies (Basel)*, vol. 14, no. 7, Apr. 2021, doi: 10.3390/en14071974.

[98] J. Shaeri, A. Habibi, M. Yaghoubi, and A. Chokhachian, “The optimum window-to-wall ratio in office buildings for hot-humid, hot-dry, and cold climates in Iran,” *Environments - MDPI*, vol. 6, no. 4, Apr. 2019, doi: 10.3390/environments6040045.

[99] F. Goia, “Search for the optimal window-to-wall ratio in office buildings in different European climates and the implications on total energy saving potential,” *Solar Energy*, vol. 132, pp. 467–492, Jul. 2016, doi: 10.1016/j.solener.2016.03.031.

[100] X. Wang, “Image recognition of english vocabulary translation based on FPGA high-performance algorithm,” *Microprocess Microsyst*, vol. 80, Feb. 2021, doi: 10.1016/j.micpro.2020.103542.

[101] C. Godoy-Rangel, C. I. Rivera-Solorio, and M. Gijón-Rivera, “TecSB: An Open Web Tool of Energy Efficiency and Solar Energy Integration in Mexican Buildings,” *Sustainability (Switzerland)*, vol. 15, no. 4, Feb. 2023, doi: 10.3390/su15043630.

[102] Y. K. Paunski and G. T. Angelov, “Performance and power consumption analysis of low-cost single board computers in educational robotics,” in *IFAC-PapersOnLine*, Elsevier B.V., Nov. 2019, pp. 424–428. doi: 10.1016/j.ifacol.2019.12.575.

[103] V. Sharma and P. Kumar, “Electro-optically oriented Kerr and orientational phase study of normal mode polymer dispersed liquid crystals – Effect of dispersion of nanoparticles,” *J Mol Liq*, vol. 348, Feb. 2022, doi: 10.1016/j.molliq.2021.118030.

[104] S. Shaik, K. Gorantla, M. Venkata Ramana, S. Mishra, and K. S. Kulkarni, “Thermal and cost assessment of various polymer-dispersed liquid crystal film smart windows for energy efficient buildings,” *Constr Build Mater*, vol. 263, Dec. 2020, doi: 10.1016/j.conbuildmat.2020.120155.

[105] A. Ghosh and T. K. Mallick, “Evaluation of colour properties due to switching behaviour of a PDLC glazing for adaptive building integration,” *Renew Energy*, vol. 120, pp. 126–133, May 2018, doi: 10.1016/j.renene.2017.12.094.

[106] K. Wu *et al.*, “Highly flexible and electrically controlled grating enabled by polymer dispersed liquid crystal,” *J Mol Liq*, vol. 353, May 2022, doi: 10.1016/j.molliq.2022.118664.

[107] M. Lami, F. Al-Naemi, H. Alrashidi, and W. Issa, “Quantifying of Vision through Polymer Dispersed Liquid Crystal Double-Glazed Window,” *Energies (Basel)*, vol. 15, no. 9, May 2022, doi: 10.3390/en15093196.

[108] H. Chen *et al.*, “A Stable PDLC Film with High Ageing Resistance from an Optimized System Containing Rigid Monomer,” *Molecules*, vol. 28, no. 4, Feb. 2023, doi: 10.3390/molecules28041887.

[109] J. H. Kim and S. H. Han, “Indoor Daylight Performances of Optimized Transmittances with Electrochromic-Applied Kinetic Louvers,” *Buildings*, vol. 12, no. 3, Mar. 2022, doi: 10.3390/buildings12030263.

[110] H. Musameh, H. Alrashidi, F. Al-Neami, and W. Issa, “Energy performance analytical review of semi-transparent photovoltaics glazing in the United Kingdom,” *Journal of Building Engineering*, vol. 54. Elsevier Ltd, Aug. 15, 2022. doi: 10.1016/j.jobe.2022.104686.

[111] A. Ghosh, “Investigation of vacuum-integrated switchable polymer dispersed liquid crystal glazing for smart window application for less energy-hungry building,” *Energy*, vol. 265, Feb. 2023, doi: 10.1016/j.energy.2022.126396.

[112] S. Shaik, S. Nundy, V. R. Maduru, A. Ghosh, and A. Afzal, “Polymer dispersed liquid crystal retrofitted smart switchable glazing: Energy saving, diurnal illumination, and CO2 mitigation prospective,” *J Clean Prod*, vol. 350, May 2022, doi: 10.1016/j.jclepro.2022.131444.

[113] A. Mesloub, A. Ghosh, L. Kolsi, and M. Alshenaifi, “Polymer-Dispersed Liquid Crystal (PDLC) smart switchable windows for less-energy hungry buildings and visual comfort in hot desert climate,” *Journal of Building Engineering*, vol. 59, Nov. 2022, doi: 10.1016/j.jobe.2022.105101.

[114] D. Chidubem Iluyemi, S. Nundy, S. Shaik, A. Tahir, and A. Ghosh, “Building energy analysis using EC and PDLC based smart switchable window in Oman,” *Solar Energy*, vol. 237, pp. 301–312, May 2022, doi: 10.1016/j.solener.2022.04.009.

[115] K. A. R. Ismail, T. G. S. Lago, F. A. M. Lino, M. V. Mondlane, and M. P. R. Teles, “Experimental investigation on ventilated window with reflective film and development of correlations,” *Solar Energy*, vol. 230, pp. 421–434, Dec. 2021, doi: 10.1016/j.solener.2021.10.061.

[116] R. Pereira *et al.*, “Ranking programming languages by energy efficiency,” *Sci Comput Program*, vol. 205, May 2021, doi: 10.1016/j.scico.2021.102609.

[117] “MATLAB. 9.7.0.1190202 (R2020a); The MathWorks Inc.: Natick, MA, USA, 2020.”

[118] M. Dabbagh and M. Krarti, “Optimal control strategies for switchable transparent insulation systems applied to smart windows for us residential buildings,” *Energies (Basel)*, vol. 14, no. 10, May 2021, doi: 10.3390/en14102917.

[119] W. Ke *et al.*, “Comparative analysis on the electrical and thermal performance of two CdTe multi-layer ventilated windows with and without a middle PCM layer: A preliminary numerical study,” *Renew Energy*, vol. 189, pp. 1306–1323, Apr. 2022, doi: 10.1016/j.renene.2022.03.090.

[120] C. Wang, N. Li, T. Gu, J. Ji, and B. Yu, “Design and performance investigation of a novel double-skin ventilated window integrated with air-purifying blind,” *Energy*, vol. 254, Sep. 2022, doi: 10.1016/j.energy.2022.124476.

[121] R. Krishnamoorthy, K. Krishnan, and C. Bharatiraja, “Deployment of IoT for smart home application and embedded real-time control system,” in *Materials Today: Proceedings*, Elsevier Ltd, 2021, pp. 2777–2783. doi: 10.1016/j.matpr.2020.11.741.

[122] M. Dobrojevic and N. Bacanin, “IoT as a Backbone of Intelligent Homestead Automation,” *Electronics (Switzerland)*, vol. 11, no. 7. MDPI, Apr. 01, 2022. doi: 10.3390/electronics11071004.

[123] A. H. S. Ahmad, A. Riazuddin, and S. A. Khan, “An FPGA cost estimation technique for design space exploration (DSE),” in *17th IEEE International Multi Topic Conference: Collaborative and Sustainable Development of Technologies, IEEE INMIC 2014 - Proceedings*, Institute of Electrical and Electronics Engineers Inc., Apr. 2015, pp. 378–382. doi: 10.1109/INMIC.2014.7097369.

[124] “Python Software Foundation, 2018. Python. Retrieved from. https://www.python.org/.”

[125] M. H. Elkholy, H. Metwally, M. A. Farahat, T. Senjyu, and M. Elsayed Lotfy, “Smart centralized energy management system for autonomous microgrid using FPGA,” *Appl Energy*, vol. 317, Jul. 2022, doi: 10.1016/j.apenergy.2022.119164.

[126] A. Kumar, N. Patel, N. Gupta, and V. Gupta, “Design, analysis and implementation of electronically interfaced photovoltaic system using ARM Cortex-M4 microcontroller,” *Computers and Electrical Engineering*, vol. 98, Mar. 2022, doi: 10.1016/j.compeleceng.2022.107701.

[127] N. Wang *et al.*, “Self-adaptive PDLC Control Strategy with Smart Light Intensity Adjustment Using Photovoltaic-Thermoelectric Hybrid Energy Supply Technology,” *IEEE Transactions on Industrial Electronics*, Oct. 2022, doi: 10.1109/TIE.2022.3224166.

[128] K. Grygierek and J. Ferdyn-Grygierek, “Design of Ventilation Systems in a Single-Family House in Terms of Heating Demand and Indoor Environment Quality,” *Energies (Basel)*, vol. 15, no. 22, Nov. 2022, doi: 10.3390/en15228456.

[129] F. Chekired, O. Taabli, Z. M. Khellili, A. Tilmatine, A. T. de Almeida, and L. Canale, “Near-Zero-Energy Building Management Based on Arduino Microcontroller—On-Site

Lighting Management Application," *Energies (Basel)*, vol. 15, no. 23, Dec. 2022, doi: 10.3390/en15239064.

[130] B. Mobaraki, S. Komarizadehasl, F. J. Castilla Pascual, and J. A. Lozano-Galant, "Application of Low-Cost Sensors for Accurate Ambient Temperature Monitoring," *Buildings*, vol. 12, no. 9, Sep. 2022, doi: 10.3390/buildings12091411.

[131] J. Liu and J. Feng, "Design of embedded digital image processing system based on ZYNQ," *Microprocess Microsyst*, vol. 83, Jun. 2021, doi: 10.1016/j.micpro.2021.104005.

[132] K. Jaskolka, J. Seiler, F. Beyer, and A. Kaup, "A Python-based laboratory course for image and video signal processing on embedded systems," *Heliyon*, vol. 5, no. 10, Oct. 2019, doi: 10.1016/j.heliyon.2019.e02560.

[133] F. C. Pereira and C. E. Pereira, "Embedded image processing systems for automatic recognition of cracks using UAVs," in *IFAC-PapersOnLine*, Jul. 2015, pp. 16–21. doi: 10.1016/j.ifacol.2015.08.101.

[134] C. Ware, "Lightness, Brightness, Contrast, and Constancy," in *Information Visualization*, Elsevier, 2021, pp. 69–94. doi: 10.1016/b978-0-12-812875-6.00003-7.

[135] L. Maurya, V. Lohchab, P. Kumar Mahapatra, and J. Abonyi, "Contrast and brightness balance in image enhancement using Cuckoo Search-optimized image fusion," *Journal of King Saud University - Computer and Information Sciences*, vol. 34, no. 9, pp. 7247–7258, Oct. 2022, doi: 10.1016/j.jksuci.2021.07.008.

[136] D. Kim and J. Lee, "Predictive evaluation of spectrogram-based vehicle sound quality via data augmentation and explainable artificial Intelligence: Image color adjustment with brightness and contrast," *Mech Syst Signal Process*, vol. 179, Nov. 2022, doi: 10.1016/j.ymssp.2022.109363.

[137] M. Wang, S. D. Zhou, Z. Yang, and Z. H. Liu, "Error analysis of atmospheric visibility measurements based on an image brightness contrast method," *IEEE Access*, vol. 8, pp. 48408–48415, 2020, doi: 10.1109/ACCESS.2020.2978941.

[138] Z. Zhou, Z. Shi, and W. Ren, "Linear Contrast Enhancement Network for Low-Illumination Image Enhancement," *IEEE Trans Instrum Meas*, vol. 72, 2023, doi: 10.1109/TIM.2022.3232641.

[139] H. T. Wu, X. Cao, R. Jia, and Y. M. Cheung, "Reversible Data Hiding With Brightness Preserving Contrast Enhancement by Two-Dimensional Histogram Modification," *IEEE Transactions on Circuits and Systems for Video Technology*, vol. 32, no. 11, pp. 7605–7617, Nov. 2022, doi: 10.1109/TCSVT.2022.3180007.

[140] M. Kim and A. Tzempelikos, "Performance evaluation of non-intrusive luminance mapping towards human-centered daylighting control," *Build Environ*, vol. 213, Apr. 2022, doi: 10.1016/j.buildenv.2022.108857.

[141] M. Kim, I. Konstantzos, and A. Tzempelikos, “Real-time daylight glare control using a low-cost, window-mounted HDRI sensor,” *Build Environ*, vol. 177, Jun. 2020, doi: 10.1016/j.buildenv.2020.106912.

[142] Y. Bian, Y. Chen, J. Luo, and Y. Sun, “Contrast-based evaluation of the reflected daylight glare on the blackboard in a classroom with complex fenestration systems,” *Journal of Building Engineering*, vol. 64, Apr. 2023, doi: 10.1016/j.jobe.2022.105622.

[143] T. Y. Y. Fung and H. Yang, “Study on thermal performance of semi-transparent building-integrated photovoltaic glazings,” *Energy Build*, vol. 40, no. 3, pp. 341–350, 2008, doi: 10.1016/j.enbuild.2007.03.002.

[144] A. Ghosh, B. Norton, and A. Duffy, “Measured overall heat transfer coefficient of a suspended particle device switchable glazing,” *Appl Energy*, vol. 159, pp. 362–369, 2015, doi: 10.1016/j.apenergy.2015.09.019.

[145] D. C. Agrawal, “Heating-times of tungsten filament incandescent lamps,” vol. 15, no. November 2017, pp. 86–97, 2018.

[146] H. A. JONES, *the Characteristics of Tungsten Filaments As Functions of Temperature*, vol. 138, no. i. Pergamon Press Ltd, 1960. doi: 10.1016/b978-1-4831-9910-8.50023-9.

[147] A. Shrestha and T. Shimizu, “Evaluation of the suppressive effects on solar radiation for a building façade covered with green layers in the Kathmandu valley,” *Environmental Challenges*, vol. 5, p. 100246, Dec. 2021, doi: 10.1016/j.envc.2021.100246.

[148] D. Mas Ł Y, M. Sitek, and K. Fross, “The impact of solar radiation on the quality of buildings: Research methods,” in *Lecture Notes in Computer Science (including subseries Lecture Notes in Artificial Intelligence and Lecture Notes in Bioinformatics)*, Springer Verlag, 2015, pp. 322–331. doi: 10.1007/978-3-319-20687-5_31.

[149] A. A. A. Shohan, H. Al-Khatri, A. A. Bindajam, and M. B. Gadi, “Solar gain influence on the thermal and energy performance of existing mosque buildings in the hot-arid climate of Riyadh city,” *Sustainability (Switzerland)*, vol. 13, no. 6, Mar. 2021, doi: 10.3390/su13063332.

[150] M. S. G. Casagrande *et al.*, “Numerical Assessment of Downward Incoming Solar Irradiance in Smoke Influenced Regions—A Case Study in Brazilian Amazon and Cerrado,” *Remote Sens (Basel)*, vol. 13, no. 22, p. 4527, Nov. 2021, doi: 10.3390/rs13224527.

[151] C. Kandilli and K. Ulgen, “Solar illumination and estimating daylight availability of global solar irradiance,” *Energy Sources, Part A: Recovery, Utilisation and Environmental Effects*, vol. 30, no. 12, pp. 1127–1140, Jan. 2008, doi: 10.1080/15567030601100688.

[152] C. Ionescu, C. Fosalau, and D. Petrisor, “A study of changes in image contrast with various algorithms,” in *EPE 2014 - Proceedings of the 2014 International Conference*

and Exposition on Electrical and Power Engineering, Institute of Electrical and Electronics Engineers Inc., Dec. 2014, pp. 100–104. doi: 10.1109/ICEPE.2014.6969876.

[153] H. J. Wyatt, "The Form of the Human Pupil," 1995.

[154] M. Yu *et al.*, "Steric group-based polymer dispersed liquid crystal composite films with high contrast ratio, low driving voltage and small hysteresis," *J Mol Liq*, vol. 365, Nov. 2022, doi: 10.1016/j.molliq.2022.120152.

[155] A. Katariya-Jain and R. R. Deshmukh, "Effects of dye doping on electro-optical, thermo-electro-optical and dielectric properties of polymer dispersed liquid crystal films," *Journal of Physics and Chemistry of Solids*, vol. 160, Jan. 2022, doi: 10.1016/j.jpcs.2021.110363.

[156] "Raspberry Pi Foundation, 2018. Raspberry Pi - Teach, Learn, and Make with Raspberry Pi. Retrieved from. https://www.raspberrypi.org/."

[157] "B. Strohmer, A. BØgild, A. S. SØrensen and L. B. Larsen, 'ROS-Enabled Hardware Framework for Experimental Robotics,' 2019 International Conference on ReConFigurable Computing and FPGAs (ReConFig), 2019, pp. 1-2, doi: 10.1109/ReConFig48160.2019.8994770."

[158] "https://www.intel.com/content/www/us/en/products/details/fpga/development-tools/quartus-prime/resource.html."

[159] S. L. Harris and D. Harris, "4 - Hardware Description Languages," in *Digital Design and Computer Architecture*, S. L. Harris and D. Harris, Eds., Morgan Kaufmann, 2022, pp. 170–235. doi: https://doi.org/10.1016/B978-0-12-820064-3.00004-0.

[160] E. P. Pozhidaev, A. V. Kaznacheev, S. I. Torgova, V. V. Kesaev, and V. A. Barbashov, "Polymer dispersed liquid crystals with electrically controlled light scattering in the visible and near-infrared ranges," *Opt Mater Express*, vol. 10, no. 12, p. 3030, Dec. 2020, doi: 10.1364/ome.410163.

[161] G. Bekaroo and A. Santokhee, "Power consumption of the Raspberry Pi: A comparative analysis," in *2016 IEEE International Conference on Emerging Technologies and Innovative Business Practices for the Transformation of Societies, EmergiTech 2016*, Institute of Electrical and Electronics Engineers Inc., Nov. 2016, pp. 361–366. doi: 10.1109/EmergiTech.2016.7737367.

[162] "Texas Instruments Inc. TMS320C6A816x C6-Integra DSP+ARM Processors. Literature number: SPRS680B, 2011."

[163] Y. Bai *et al.*, "FPGA vs DSP: A throughput and power efficiency comparison for Hierarchical Enumerative Coding," in *IEEE/IFIP International Conference on VLSI and System-on-Chip, VLSI-SoC*, IEEE Computer Society, 2013, pp. 318–321. doi: 10.1109/VLSI-SoC.2013.6673300.

[164] F. Bolaños, J. M. LeDue, and T. H. Murphy, "Cost effective raspberry pi-based radio frequency identification tagging of mice suitable for automated in vivo imaging," *J*

Neurosci Methods, vol. 276, pp. 79–83, Jan. 2017, doi: 10.1016/j.jneumeth.2016.11.011.

[165] E. Mostafa Saad, A. Hamdy, M. M. Abutaleb, E. M. Saad, A. Hamdy, and M. M. Abutaleb, "FPGA-based implementation of a low cost and area real-time motion detection Redundant Independent Files (RIF): A Technique for Reducing storage and Resources in Big Data Replication View project computer aided diagnosis View project FPGA-BASED IMPLEMENTATION OF A LOW COST AND AREA REAL-TIME MOTION DETECTION," 2008. [Online]. Available: https://www.researchgate.net/publication/224326286

[166] S. F. Wirtz, A. P. A. Cunha, M. Labusch, G. Marzun, S. Barcikowski, and D. Söffker, "Development of a low-cost FPGA-based measurement system for real-time processing of acoustic emission data: Proof of concept using control of pulsed laser ablation in liquids," *Sensors (Switzerland)*, vol. 18, no. 6, Jun. 2018, doi: 10.3390/s18061775.

[167] "https://www.terasic.com.tw/cgi-bin/page/archive.pl?Language=English&CategoryNo=167&No=819."

[168] "https://www.mathworks.com/pricing-licensing.html."

[169] J. Wanza Weloli, S. Bilavarn, M. de Vries, S. Derradji, and C. Belleudy, "Efficiency modeling and exploration of 64-bit ARM compute nodes for exascale," *Microprocess Microsyst*, vol. 53, pp. 68–80, Aug. 2017, doi: 10.1016/j.micpro.2017.06.019.

[170] P. M. Aviles, A. Lindoso, J. A. Belloch, and L. Entrena, "Evaluating reliability through soft error triggered exceptions at ARM Cortex-A9 microprocessor," *Microelectronics Reliability*, vol. 126, Nov. 2021, doi: 10.1016/j.microrel.2021.114323.

[171] C. Y. Lee, T. Y. Lin, and R. G. Chang, "Power-aware code scheduling assisted with power gating and DVS," *Future Generation Computer Systems*, vol. 34, pp. 66–75, May 2014, doi: 10.1016/j.future.2013.12.011.

[172] S. Nouri, D. Rossi, and J. Nurmi, "Power mitigation of a heterogeneous multicore architecture on FPGA/ASIC by DFS/DVFS techniques," *Microprocess Microsyst*, vol. 63, pp. 259–268, Nov. 2018, doi: 10.1016/j.micpro.2018.09.010.

[173] A. HajiRassouliha, A. J. Taberner, M. P. Nash, and P. M. F. Nielsen, "Suitability of recent hardware accelerators (DSPs, FPGAs, and GPUs) for computer vision and image processing algorithms," *Signal Process Image Commun*, vol. 68, pp. 101–119, Oct. 2018, doi: 10.1016/j.image.2018.07.007.

[174] L. Pyrgas, P. Kitsos, and A. Skodras, "Compact FPGA architectures for the two-band fast discrete Hartley transform," *Microprocess Microsyst*, vol. 61, pp. 117–125, Sep. 2018, doi: 10.1016/j.micpro.2018.06.002.

[175] A. Prakash, S. K. Lam, C. T. Clarke, and T. Srikanthan, “FPGA-aware techniques for rapid generation of profitable custom instructions,” *Microprocess Microsyst*, vol. 37, no. 3, pp. 259–269, 2013, doi: 10.1016/j.micpro.2013.02.002.

[176] Z. Mo, D. Luo, T. Wen, Y. Cheng, and X. Li, “FPGA implementation for odor identification with depthwise separable convolutional neural network,” *Sensors (Switzerland)*, vol. 21, no. 3, pp. 1–19, Feb. 2021, doi: 10.3390/s21030832.

[177] K. S. Unnikrishnan and S. Madhavan, “Parallel Computation Using DSP Slices in FPGA,” *Procedia Technology*, vol. 24, pp. 1127–1134, 2016, doi: 10.1016/j.protcy.2016.05.064.

[178] “Oh, M.; Tae, S.; Hwang, S. Analysis of Heating and Cooling Loads of Electrochromic Glazing in High-Rise Residential Buildings in South Korea. Sustainability 2018, 10, 1121. https://doi.org/10.3390/su10041121.”